Julien DECHELETTE

Master MNIS
2026

Institut Jean Lamour, Université de Lorraine,
2 allée André Guinier, BP 50840, 54011 Nancy CEDEX

Current-induced and light-induced magnetization dynamics in magneto-optic nanostructures

from 16/02/2026 to 15/08/2026

Under the supervision of :

- **Company supervisor : Stéphane, MANGIN, stephane.mangin@univ-lorraine.fr**
- **Phelma Tutor : Liliana, BUDA-PREJBEANU, liliana.prejbeanu@grenoble-inp.fr**

Confidentiality : ⇨ no

Ecole nationale
supérieure de physique,
électronique, matériaux

Phelma
Bât. Grenoble INP - Minatec
3 Parvis Louis Néel - CS 50257
F-38016 Grenoble Cedex 01

Tél +33 (0)4 56 52 91 00
Fax +33 (0)4 56 52 91 03

http://phelma.grenoble-inp.fr

Contents

1 Presentation of the Laboratories: 11
1.1 Institut Jean Lamour: . . . 11
1.2 Fukami - Kanai Laboratory: . . . 11

2 Context of the Internship: 12

3 Introduction to Magnetism and Spintronics: 14
3.1 Magnetic Interactions: . . . 14
3.1.1 Exchange Interaction: . . . 14
3.1.2 Zeeman Interaction: . . . 14
3.1.3 Magnetocrystalline Anisotropy: . . . 14
3.1.4 Surface Interfacial Anisotropy: . . . 15
3.1.5 Shape Anisotropy (or Demagnetizing field): . . . 15
3.2 Ferromagnetic Materials: . . . 15
3.3 Antiferromagnetic Materials: . . . 16
3.4 Synthetic Antiferromagnetic Materials (SAF): . . . 17
3.5 Magneto-optical effects: . . . 17
3.6 Evolution of Magnetoresistance from AMR to TMR: . . . 18
3.7 Spin-Transfer Torque (STT): . . . 21
3.7.1 Reading STT: . . . 21
3.7.2 Writing STT: . . . 22
3.7.3 Stability STT: . . . 22
3.8 All Optical Switching (AOS) and ultrafast spin dynamics: . . . 23

4 Fabrication of STT devices: 25
4.1 Optimization of Thin Films for STT and AOS . . . 25
4.1.1 Investigation of Ir thickness to obtain an antiferromagnetically coupled layer 26
4.1.2 Investigation of the bottom layer for perpendicular magnetization of Co/Ni layer . . . 28
4.1.3 Investigation of Co Thickness to Obtain Different Curie Temperature, and Influence on AOS . . . 28
4.2 Process flow for the Fabrication of 4 Terminal STT Device . . . 34
4.2.1 Electron-Beam Lithography . . . 36
4.2.2 Ion Beam Etching . . . 38
4.2.3 Lift Off . . . 39

5 Characterization of STT devices: 41
5.1 Presentation of the characterization setup . . . 41
5.2 Characterization of MgO based MTJ (**H2** and **H3**) . . . 41
5.2.1 Thermal stability of STT device . . . 42
5.2.2 State Diagram . . . 43
5.3 Mapping of the wafers **H2** and **H3** . . . 45

5.4 Characterization of **1532** and **1534** 47
5.4.1 Field switching 47
5.4.2 State Diagram 48

6 Further Development of the AOS–STT Combination: 51
6.1 Modification of the top electrode 51
6.2 Modify the Copper interlayer 52

7 Conclusion: 53

8 Bibliography: 54

A Gantt Diagram: 58

B Summary sheet: 59

C Skill Report: 62
C.1 C1: Designing or Implementing engineering solutions to meet a specification 62
C.2 C2: Implementing a fundamental research approach or an applied research approach for innovation purposes 65
C.3 C3: Collaborate within a team and in project mode 68
C.4 C4: Work and communicate in an international and intercultural environment . . . 71
C.5 C5: Integrate technological, environmental and societal transitions into the work . . 73
C.6 Traces of Project: 76

List of Figures

1 (a) Memory hierarchy from standalone memory in grey, to embedded memory in blue. On the right of the picture are represented some novel non-volatile memory devices, image taken from [8], (b) Evolution of memory storage according to time, image taken from [3] 12

2 (a) Microscopic ordering in a ferromagnet, image taken from [10], (b) Influence of temperature on the magnetization, image adapted from [11], (c) Hysteresis curve of a ferromagnet [2], the magnetization M changes according to the applied field H . M_S: saturation magnetization, M_R: remanence magnetization, H_C: coercivity field . 16

3 (a) Microscopic view of the 2 sublattices of the antiferromagnet, image taken from [10], (b) Magnetic susceptibility dependence over temperature, image taken from [14] 17

4 (a) Oscillation of the exchange constant as a function of the non-magnetic layer thickness, image taken from [25], (b) Schematic structure of a single synthetic antiferromagnetic layer, image taken from [15] 18

5 Rotation of the light polarization in a material subjected to an applied magnetic field, image taken from [16]. 18

6 Architecture of a spin valve structure, black arrows indicate the magnetization direction of the thin films, gray squares are the electrical contacts, green squares are the free magnetic layers (FL), blue squares are the pinned magnetic layers (RF), violet squares are non-magnetic spacers (NM), image adapted from [19] 19

7 (a) Parallel configuration (P) of the GMR on the left and two-channel model of the resistance, (b) Antiparallel configuration (AP) of the GMR on the right and two-channel model of the resistance, image adapted from [17, 20] 20

8 Density of states and current for the P and AP configurations for TMR, image taken from [17] 20

9 Schematic of the spin transfer torque switching, (a) from AP to P, (b) from P to AP, the blue arrows indicate the initial magnetization and the red arrows indicate the final magnetization, images adapted from [7] 21

10 (a) Evolution of current density according to current pulse width for different thermal stability, (b) Representation of torques applied on the free magnetic moment, images taken from [27] 23

11 Magnetization dynamics induced by an optical excitation of GdFe, image taken from [28] 24

12 Spin valve structure, (a) Composition of the spin valve, (b) Magnetization reversal from AP to P, (c) Magnetization reversal from P to AP, blue electrons are generated from the free layer, red electrons are generated from reference layer, image taken from [30] 24

13 Thin Film composition for AOS-STT sample, on the rigth of the thin film are presented the number multilayers, on the left are presented the function of each multilayer (FL : Free Layer, SAF-RF : Synthetic Antiferromagnetic - Reference Layer) 25

14 Thin film composition for RKKY optimization of Iridium thickness, (a) Multilayer optimization of the SAF, (b) Definition of Ir wedge 26

15 Measured Kerr signal as a function of an applied perpendicular magnetic field for different Ir thickness. 27
16 Different compositions of the bottom layer and their normalized out-of-plane hysteresis, (a, c) Thin film 1521 and its out-of-plane hysteresis, (b, d) Thin film 1526 and its out-of-plane hysteresis, (c, e) Thin film 1527 and its out-of-plane hysteresis . 28
17 All fabricated thin films for STT-AOS optimization, the thin-film compositions on top and their out-of-plane hysteresis curves on the bottom measured using VSM, (a, f) thin film **1528**, (b, g) thin film **1531**, (c, h) thin film **1532**, (d, i) thin film **1533**, (e, j) thin film **1534** 29
18 On (a) each arrow represents its corresponding layer for the thin film **1534**, (b) measurement of the magnetization of the thin film using VSM, (c) measurement of magnetization of the thin film using the Kerr effect, note that the X-axis is in Amperes as we are using an electromagnet, in blue the Kerr signal of the whole substrate, in orange the Kerr signal on the laser spot 30
19 TR MOKE setup, HWP : half-wave plate, QWP : quarter-wave plate, P : polarizer, A : analyzer, C : chopper, S : sample, EM : electromagnet, M : mirror, L : lens, F : filter, CCD Camera : Charge Coupled Device camera, the pump (1030 nm) in red, the probe (550 nm) in orange, image taken from [35] chapter 4.3.4 TR-MOKE Microscopy 31
20 TR MOKE experiments on thin film **1534**, (a) Evolution of the magnetization dynamics as a function of different applied fluences, in the labels are the applied fluences, (b) Evolution of the magnetization dynamics as a function of the different applied fields, for a fluence of 180.1 J/m^2 31
21 (a) Comparison of the magnetization dynamics of the thin films **1532** and **1534** at 122.5 J/m^2, (b) Comparison of the magnetization dynamics of the thin films at 180.1 J/m^2 32
22 State Diagram for a ferrimagnetic spin valve, $TF_{P\rightarrow AP}$: Threshold fluence to observe P to AP switching, $TF_{AP\rightarrow P}$: Threshold fluence to observe AP to P switching, $TF_{FIM\rightarrow MD}$ Threshold fluence to observe multi-domains in the ferrimagnetic layer, TF_{MD} Threshold fluence to observe multi-domain in ferrimagnetic and ferromagnetic layers, image taken from [38] 33
23 (a) Dynamics of angular momentum transfer in ultrafast spintronics, image taken from [36], (b) TR MOKE experiment for the thin film **1534**, with a laser fluence of 180.1 J/m^2, from 0 fs to 200 fs is the ultrafast demagnetization regime, from 200 fs to 2 ps is the non-equilibrium recovery, and after 2 ps is the equilibrium recovery . . 34
24 (a) Imaging of the transition from P- state to AP- state, (b) Imaging from the P+ state to the AP+ state 34
25 Thin films (a) **1532**, and (b) **1534**, have been deposited at IJL, while thin films (c) **H2**, and (d) **H3** have been deposited at Tohoku University 35
26 Layout of the photomasks used for fabrication, (a) Layout of the full chip (1cm x 1cm), design using Klayout, (b) Layout of the 4 terminal device, (c) Layout of the 2 terminal device, (d) 3D view of the 4 terminal device, (e) 3D view of the 2 terminal device 36
27 Schematic of the process flow for the fabrication of nanopillars 37

28 (a) SEM image of the nanopillars after TGMR development, fig. 27c, (b) SEM image of the nanopillars after Lift-Off of Al_2O_3, fig. 27g 37
29 (a) represents the 40° etching angle used to etch the thin film down to Ta/Pt, (b) represents the 80° etching angle used to etch the side wall of the nanopillars, (c) Measured signal from the Hakuto etching tool, in order to monitor the etching of the nanopillars 38
30 (a) Layout of the alignment mark, in red the gold mark, in blue the TGMR resist, the black arrow corresponds to the path of the profilometer tip, (b) Profilometer profile according to the fabrication step, post-development corresponds to step 3, post-etching corresponds to step 4, post-deposition corresponds to step 5 and post-lift-off corresponds to step 7 39
31 (a) presents the first setup using only 2 terminal, it applies a voltage and measures a current, (b) presents the second setup using 4 terminal, it applies a current and measures a voltage 41
32 (a) Multiple hysteresis loop to obtain a distribution of the coercivity field, (b) Distribution of the coercivity field H_{AP} corresponds to the field to switch from P to AP, H_P corresponds to the field to switch from AP to P, (c) Distribution of the coercivity field centered at 0 Oe, (d) Distribution of the coercivity field and curve fitting to obtain thermal stability and anisotropy field 42
33 (a) Multiple hysteresis curve as a function of applied voltage, (b) Distribution and curve fitting to obtain thermal stability and critical switching voltage 44
34 State Diagram of the device, in red corresponds the fact that the device is saturated in one state (AP or P), in blue corresponds the fact that the device stay in its previous state, at the intersection between the blue and red area is the probability of switching from P to AP, or AP to P 44
35 (a) represents the mapping of the TMR in % for every device on **H2**, it has been characterized on the 2 probes setup, (b) represents the mapping of the TMR in % for every 4 terminal device on **H3**, it has been characterized on the 4 probes setup . 45
36 (a) represents the distribution of TMR according to the minimum resistance, (b) represents the distribution of TMR according to minimum resistance but only for device with 500 nm diameter, most of the errorbar are inside the dot 46
37 Evolution of thermal stability as a function of the electrical diameter for some devices, the labels correspond to the position of the devices on the wafer 47
38 (a) shows the hysteresis loop on the minor loop of the device at 1000 uA, (b) shows the hysteresis loop on the major loop of the device at 1000 uA 47
39 (a) is the state diagram of the sample **1532**, (b) is the state diagram of the sample **1534** 48
40 (a) represents the evolution of the coercivity field of the sample **1532** as a function of the applied voltage due to STT effect, (b) represents the evolution of the stray field of the sample **1532**, (c) represents the evolution of the coercivity field of the sample **1534** as a function of the applied voltage, (d) represents the evolution of the stray field according to voltage 50
41 Evolution of the sheet resistance (in blue) and the optical transmission (in red) as a function of the thickness of the Cr(5nm)/Au(Xnm) thin film 51

42 3D view of the potential next electrodes, (a) an ITO electrode to let light flow through the electrode, (b) a separated gold top electrode to let light flow in the center 52
43 53
44 Influence of Copper thickness on threshold fluence for switching in ferromagnetic spin valve, image taken from [30] 53
45 PCB circuit of the Audio Amplifier 77
46 Evolution of collector current as a function of collector voltage 77
47 State diagram defined through automation using labview and python programms . . 78
48 Gantt Diagram presenting our role repartition and deadlines 78

List of Tables

1 Comparison between GMR and TMR 21
2 Measurement flow for P to AP characterization 33

Abstract

Abstract:

Starting in the 1950s with IBM [1], magnetic media have been studied to be used in recording applications as they allow non-volatile memory, down scaling of memory and low power consumption. However, the scaling down of magnetic media also introduces many challenges, ranging from reliability, access and power consumption.

Nowadays, magnetism and spintronics explore multiple ways to obtain more sustainable and faster systems. Ranging from Spin-Transfer Torque (STT) which uses current to reverse magnetization, to processes such as Heat Assisted Magnetization Reversal (HAMR) and All-Optical Switching, which use optical excitations to assist or induce magnetization reversal.

In this work, we attempted to combine both STT switching and AOS on a spin valve device, to study its magnetization dynamics at the picosecond timescale, as well as the influence of STT on magnetization reversal. In order to investigate the effect, some AOS experiments have been performed on blanket films, while other thin films have been patterned in cleanroom into nanopillars.

The experiments performed during this thesis were able to prove and characterize the existence of both AOS and STT on the fabricated thin films. Further experiments could shed light on the dynamics induced by the combination of both mechanism during operation.

Résumé:

Depuis les années 1950 avec IBM, les mémoires magnétiques ont fait l'objet de nombreuses études afin d'être utilisées pour le stockage de données, ils permettent d'avoir une mémoire non-volatile, d'avoir une densité surfacique importante ainsi que de réduire la consommation énergétique. Cependant, la miniaturisation des mémoires magnétiques entraine d'autres défis, tels que la fiabilité des données, leur accès ainsi que leur consommation énergétique.

Aujourd'hui, le magnétisme et la spintronique explorent de nombreuses voies afin d'obtenir des systèmes plus durables et rapides. Allant du STT utilisant le courant afin d'inverser l'aimantation, en passant par le HAMR et l'AOS qui utilisent des excitations optiques afin d'assister ou d'induire l'inversion de l'aimantation.

Dans cette thèse, nous tentons de combiner le principe du STT avec l'AOS sur une *spin valve*, afin d'étudier leur dynamique d'aimantation à l'échelle de la picoseconde, ainsi que l'influence du STT sur l'inversion de l'aimantation. Afin d'étudier ces effets, nous avons réalisé des mesures AOS sur des films minces, tandis que d'autres films minces ont été fabriqués en salle blanche pour réaliser des nanopilliers.

Les expériences réalisées durant cette thèse ont permis de démontrer et caractériser l'existence d'AOS et de STT sur les films minces fabriqués. Des investigations plus poussés seront nécessaires afin d'éclairer les mécanismes d'aimantation combinant STT et AOS.

Riassunto (*Translated from English using DeepL*):

A partire dagli anni '50 con IBM [1], i supporti magnetici sono stati oggetto di studio per il loro impiego in applicazioni di registrazione, poiché consentono una memoria non volatile, la riduzione delle dimensioni della memoria e un basso consumo energetico. Tuttavia, la

riduzione delle dimensioni dei supporti magnetici comporta anche numerose sfide, che vanno dall'affidabilità all'accessibilità fino al consumo energetico.

Oggi, il magnetismo e la spintronica esplorano diverse strade per ottenere sistemi più sostenibili e più veloci. Si va dalla coppia di trasferimento di spin (STT), che utilizza la corrente per invertire la magnetizzazione, a processi quali l'inversione di magnetizzazione assistita dal calore (HAMR) e la commutazione interamente ottica, che utilizzano eccitazioni ottiche per facilitare o indurre l'inversione della magnetizzazione.

In questo lavoro abbiamo cercato di combinare sia la commutazione STT che l'AOS su un dispositivo a valvola di spin, per studiarne la dinamica di magnetizzazione su scala temporale dei picosecondi, nonché l'influenza dell'STT sull'inversione di magnetizzazione. Al fine di indagare tale effetto, sono stati condotti alcuni esperimenti AOS su film uniformi, mentre altri film sottili sono stati modellati in camera bianca in nanopilastri.

Gli esperimenti condotti nell'ambito di questa tesi hanno permesso di dimostrare e caratterizzare l' esistenza sia dell'AOS che dell'STT sui film sottili realizzati. Ulteriori esperimenti potrebbero far luce sulle dinamiche indotte dalla combinazione di entrambi i meccanismi durante il funzionamento.

Acknowledgment:

During my master's thesis at IJL, I had the opportunity to collaborate with IJL and Fukami-Kanai laboratory for the combination of AOS and STT. This experience was sincerely amazing, both from a scientific and human point of view. From a scientific point of view, it gave me the opportunity to dig deeper on thin film optimization and characterization, on microfabrication in cleanroom, and on electrical and optical characterization of thin film and electrical devices.

Even though my thesis gave me a lot of opportunities to learn from a scientific point of view, I think the most important part was from a human point of view. As it was a collaboration between IJL (France) and Tohoku (Japan), I could collaborate with many different people with different expertises. The common point between all these people, was how passionnated they were about their work and to transmit their knowledge and know-how on magnetism and spintronics.

I would like to first of all, thank Professor Stéphane MANGIN and Professor Shunsuke FUKAMI, as both gave insightful views about how the project could evolve, by combining AOS and STT, as well as their support during my thesis, and their willingness to share their expertise on STT and AOS. Moreover, I would also like to thank Michel HEHN for his expertise in thin film growth and characterization, that allow to get quite good spin valve for this project, and for all his explanation on magnetism and thin films. Julius HOHLFELD for his help and explanations about AOS on spin valve, and for all his passions about physics and his will to transmit knowledge. Sebastien PETIT-WATELOT for his help for solving problems on electrical setup. Victor HUET for helping me with the optical and electrical characterization of SOT Hall crosses. Yann LE GUEN for his insight regarding electrical setup and optical setup, during my first months at IJL he always helped me when I faced electrical problems, and Yann was willing to help even late in the evening, his help allow me to progress on AOS and STT/SOT. Moreover, I would like to thank all member of IJL, Jon, Harjinder, Corentin, Jude, Pierre, Guillaume, Theo, for their sympathy, and all the Tarot

games we have done at lunch.

From Fukami-Kanai Laboratory, I would like first of all, to thank Nuno CAÇOILO who was the first person welcoming me in JAPAN, he gave me lot of insight about fabrication of nanopillars and about characterization of MTJ, without him the fabrication of nanopillars in cleanroom would have been far more complicated (or impossible in only 2.5 months), and I would also like to thank him for all the talks we had during my stay in Sendai. Moreover, I would like to give my thanks to Salvatore TERESI and Eva DIAZ, for their help in cleanroom, and for all the time we spend together, the time waiting in cleanroom would have been far more boring without you all.

This work has been possible thank to the help, and the involvement of everyone. Without this collaboration, my thesis could not have exposed so many and different results. Thanks to the great synergy between IJL (for AOS and thin film growth) and Fukami-Kanai laboratory (for STT and fabrication), we could obtain significant results regarding the combination of STT and AOS, showing the possibility of integrating both of them on the same device, even though a few more months would have been great to have a more thorough investigation of STT and AOS combinations.

1 Presentation of the Laboratories:





1.1 Institut Jean Lamour:

Institut Jean Lamour (IJL) is a French Mixed Research Unit (UMR), focusing on fundamental and applied research in material science. It covers themes such as materials, metallurgy, plasma, electronics and magnetism.

Their research is organized into 4 departments:

- Physics of Matter and Materials (P2M)
- Chemistry and Physics of Solids and Surface (CP2S)
- Materials Sciences and Engineering - Metallurgy
- Nanomaterials, Electronics, and Living (N2EV)

The objective of the Spintronics and Nanomagnetism group is to study magnetism at nanometer scale, to understand electronic and magnetic transport properties in magnetic structures ranging from nanopillars to thin films.

Their expertise ranges from thin film deposition and characterization, to the study of magnetization reversal using all-optical switching, as well as current-induced reversal through SOT or STT devices.

1.2 Fukami - Kanai Laboratory:

Fukami - Kanai Laboratory is a Japanese laboratory from the University of Tohoku that has a strong collaboration with IJL. It specializes in Spintronic devices, combining both electrons and spins to explore novel phenomena to contribute to the development of high performance, energy efficient electronics and advanced information and communication technologies.

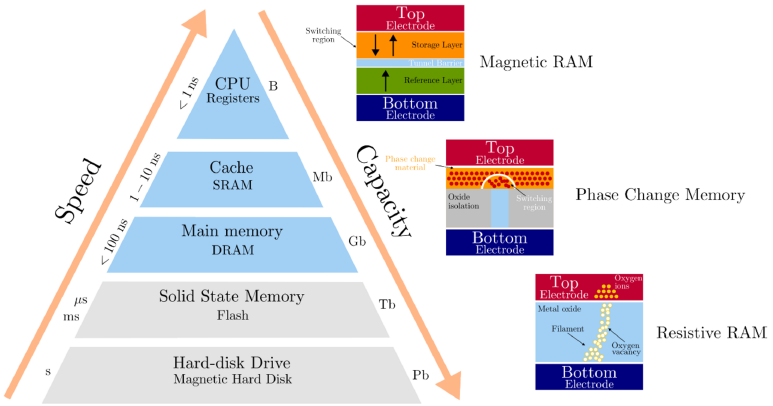
Their research focuses on 5 main areas:

- Non-volatile spintronic memory devices for energy-efficient semiconductors
- Stochastic and analog devices for novel computing paradigms
- Materials and spin properties for quantum computing/sensing/communication
- Novel spintronic physics and functionalities by innovative materials
- New spintronic application technologies for future information society

2 Context of the Internship:

For at least 2 millennia, magnetism has been used and studied, starting with the compass for navigating the globe. Centuries later, in the 1950s, IBM developed the first commercial magnetic tape drive to store data. From the 1980s, with the discovery of Giant Magnetoresistance (GMR), and in the 1990s with the discovery of Tunneling Magnetoresistance (TMR), the development of the non-volatile Magnetic Random Access Memory became possible [1].

Over the last decades, and even more with the development of Artificial Intelligence, the demand for more efficient technologies has become critical. For a memory, its efficiency is measured in terms of power consumption, writing and reading speed, and endurance (number of times information can be rewritten).



(a)



(b)

Figure 1: (a) Memory hierarchy from standalone memory in grey, to embedded memory in blue. On the right of the picture are represented some novel non-volatile memory devices, image taken from [8], (b) Evolution of memory storage according to time, image taken from [3]

As it can be seen from Figure 1, data storage has increased exponentially over the years, reaching 100 ZB in 2023. This data storage can be divided into 2 groups. First, the standalone memory (USB, Solid-State Drive, ...), which are external components with large storage capacity, but a long operating speed. These are non-volatile, as they can retain information while being powered off. On the other hand, we have the embedded memories group, which is usually formed of volatile memories, requiring constant energy to retain information (for example, FLASH and DRAM).

Between embedded and stand-alone memories, there exists a gap between the non-volatile and volatile technologies. This gap could be filled by Storage Class Memory (SCM). This additional hierarchy layer, would introduce an intermediate layer between high density memories, and fast and durable memories. One of the most promising new SCM devices is the Spin-Transfer Torque MRAM (STT-MRAM), as it is a non-volatile device, with high reliability (over 10^{12} cycles), fast reading and writing (10 ns) and energy efficiency (50 pJ/bit) [4].

STT-MRAM allows to read the information through a change in resistance, this change in resistance occurs thanks to the alignment of the ferromagnetic layers separated by a tunnel barrier. Moreover, as this is non-volatile memory, it only needs energy to switch the magnetic layer, but does not require constant energy to maintain the state.

Moreover, beside this development of SCM, stand-alone memories have also been extensively studied to improve energy efficiency, as data centers are expected to use up to 12% of US electricity production in 2028 [5]. From the application of Heat-Assisted Magnetization Reversal (HAMR) in stand-alone memory that allows higher surface density, to the investigation of All-Optical Switching (AOS) for energy efficiency and ultrafast magnetization reversal, the combination of light and magnetization has been studied for energy efficiency and fast recording [6].

In this work, we aim to combine both AOS and STT-driven magnetisation switching on the same multilayered magnetic stack. In the section 3, the basics mechanisms of magnetism and spintronics are described. In the section 4, the optimization of thin film and its cleanroom processing will be described. In the section 5, it will describe the characterization of figures of merit for spin transfer torque device. Finally, in section 6, we will describe some further advancements possible to combine AOS and STT on manufactured devices.

3 Introduction to Magnetism and Spintronics:

In this section we describe the properties of magnetic thin films and some basics on spintronic transport, such as magnetoresistance. In a second part, we explain the principles of magnetization reversal using Spin-Transfer Torque (STT) and All-Optical Switching (AOS).

3.1 Magnetic Interactions:

The magnetic moment of the atom, at the origin of the magnetism, may interact according to different kinds of interactions. Depending on the preponderant interaction, the magnetic properties could be different.

3.1.1 Exchange Interaction:

The exchange interaction occurs between the spin of two neighboring atoms $\overrightarrow{S_i}$ and $\overrightarrow{S_j}$

$$E_{\text{Exchange}} = -2 \cdot J_{ex} \cdot \overrightarrow{S_i} \cdot \overrightarrow{S_j}. \tag{1}$$

Depending on the sign of the exchange constant J_{ex} the spins will have different preferential alignments, and thus different magnetic properties [2]:

- $J_{ex} < 0$: the spins prefer an antiparallel alignment, leading to antiferromagnetism and ferrimagnetism.
- $J_{ex} > 0$: the spins align parallel to each other, leading to ferromagnetism.

3.1.2 Zeeman Interaction:

Zeeman interaction occurs between the magnetic moment of an atom, and an external applied magnetic field [2]. The magnetic moment tends to align with the applied field, as it is a minimum of energy. The energy could be expressed in the following way :

$$E_{\text{Zeeman}} = -\overrightarrow{m} \cdot \overrightarrow{H} \tag{2}$$

where $\overrightarrow{m}$ is the magnetic moment and $\overrightarrow{H}$ an external applied magnetic field.

3.1.3 Magnetocrystalline Anisotropy:

The magnetocrystalline anisotropy originates from the crystalline order of the material, leading to different magnetic properties (for example, easy and hard-axis) along different crystallographic axis [2]. This anisotropy can be expressed as an energy[8]:

$$E_{\text{bulk}} = -K_V \cdot (\hat{n} \cdot \hat{M})^2 \cdot V, \tag{3}$$

where K_V is a volume energy density [J/m^3], V is the volume [m^3], $\hat{n}$ is the normal vector along the easy axis orientation and $\hat{M}$ the magnetization orientation.

3.1.4 Surface Interfacial Anisotropy:

Surface interfacial anisotropy happens at the interface between two materials and is the backbone of perpendicular-based STT-MRAM devices. Due to the breaking of symmetry with regard to the bulk material, surface anisotropy might influence the magnetic moment and even modify the easy axis from in-plane to out-of-plane [8, 9]. Its energy can be defined as [8]:

$$E_{\text{surface}} = -\frac{k_{\text{s}}}{t} \cdot (\hat{n} \cdot \hat{M})^2 \cdot V \tag{4}$$

where k_{s} is the surface anisotropy [J/m^2], and t the thin film thickness [m].

3.1.5 Shape Anisotropy (or Demagnetizing field):

Shape anisotropy corresponds to a demagnetizing field induced by the shape of the magnetic structure. Its energy of the shape anisotropy is defined as [8]:

$$E_{Shape} = \frac{1}{2}\mu_0 M_{\text{s}}^2 \cdot N \cdot (\hat{n} \cdot \hat{M})^2 \cdot V \tag{5}$$

With μ_0 the vacuum permeability [$4\pi \cdot 10^{-7}$H/m], N is the demagnetizing tensor and M_{s} is the spontaneous magnetisation.

In magnetic thin films, all these different anisotropy terms can be present. This would then lead to a total energy of:

$$E_{\text{anisotropy}} = -K_V \cdot (\hat{n} \cdot \hat{M})^2 \cdot V - \frac{k_{\text{s}}}{t} \cdot (\hat{n} \cdot \hat{M})^2 \cdot V + \frac{1}{2}\mu_0 \cdot N M_{\text{s}}^2 \cdot (\hat{n} \cdot \hat{M})^2 \cdot V \tag{6}$$

This anisotropy energy is the minimum energy required to switch the magnetization from one magnetic state to the other. It is the energy barrier to reverse the magnetic state:

$$E_B = -(K_V + \frac{k_{\text{s}}}{t} - \frac{\mu_0}{2} N M_{\text{s}}^2) \cdot V = -K_{\text{eff}} \cdot V \tag{7}$$

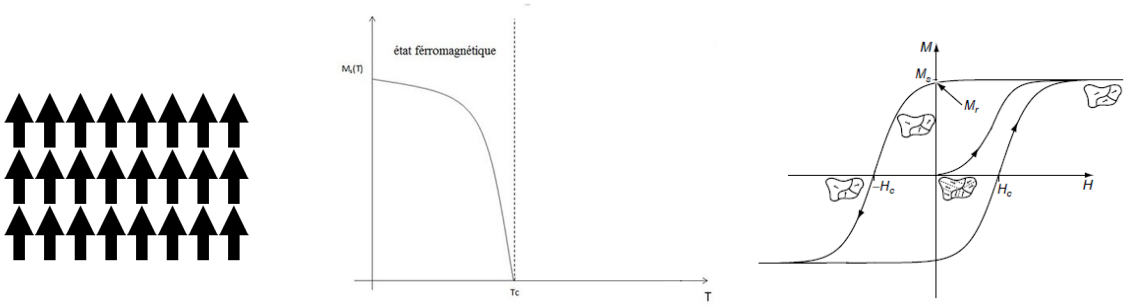
According to the effective anisotropy constant K_{eff}, the magnetization of the material could go from out-of-plane to in-plane magnetization. These are the main interactions in magnetic thin films which will determine the magnetic properties of the structures studied in this thesis.

In the rest of this thesis, we will consider the magnetic moments in the macrospin approximation, all the magnetic moments in the materials act coherently.

3.2 Ferromagnetic Materials:

A ferromagnetic material is a material in which most of the magnetic moments from the lattice are aligned together in parallel, due to exchange interaction. This alignment leads to an intrinsic magnetization along the easy axis of the material.

As observed on Figure 2b, the magnetic ordering of the material depends on the temperature. Below the Curie Temperature T_C, the magnetic moments are aligned thanks to the exchange interaction as seen on Figure 2a, which leads to an intrinsic magnetization. However, when the temperature increases, thermal fluctuations start to disorder the magnetic



(a) (b) (c)

Figure 2: (a) Microscopic ordering in a ferromagnet, image taken from [10], (b) Influence of temperature on the magnetization, image adapted from [11], (c) Hysteresis curve of a ferromagnet [2], the magnetization M changes according to the applied field H . M_S: saturation magnetization, M_R: remanence magnetization, H_C: coercivity field

moments that lead to a decrease in magnetization, until the complete demagnetization above Curie temperature.

- $T < T_C$: Magnetic moments are ordered, the material has a net magnetization. Exchange interaction dominates.
- $T > T_C$: Magnetic moments are disordered, there is no magnetization. Thermal fluctuations dominate.

As shown on Figure 2c, the magnetization of the material as a function of the applied field, is a hysteresis according to the field applied.

From the Stoner-Wohlfarth model [12, 13], we can define the anisotropy field H_K that corresponds to the field necessary to overcome the intrinsic magnetization:

$$H_K = \frac{2K_{\text{eff}}}{\mu_0 M_{\text{s}}} \tag{8}$$

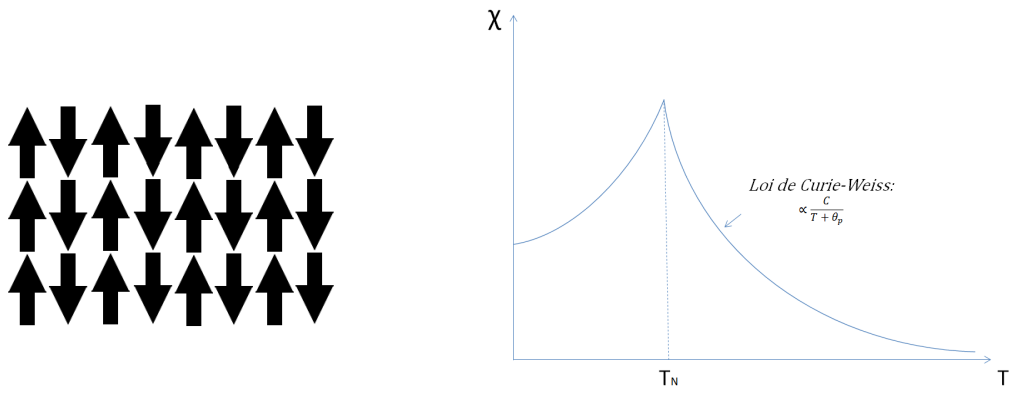
With M_{s} the saturation magnetization, the anisotropy field H_K is the upper limit for the coercivity field H_C, most of the time H_C is lower than 50% of H_K due to defects in the film [13].

3.3 Antiferromagnetic Materials:

As for a ferromagnetic material, the predominant interaction in an antiferromagnetic material is the exchange interaction.. However, in this case the exchange constant J_{ex} is negative, meaning that the magnetic moments are aligned in an antiparallel distribution to minimize the energy. Moreover, as the magnetic moments of every atom are antiparallel and have the same magnitude, there is no net magnetization.

As a ferromagnetic material, the properties of an antiferromagnetic material have a dependence in temperature, as shown in Figure 3b. Below the Néel temperature T_N, the magnetic moments are aligned antiparallel, as shown on Figure 3a, while above T_N the magnetic moments are disordered.

- $T < T_N$: Magnetic moments are ordered in an antiparallel order. Exchange interaction dominates.



(a) (b)

Figure 3: (a) Microscopic view of the 2 sublattices of the antiferromagnet, image taken from [10], (b) Magnetic susceptibility dependence over temperature, image taken from [14]

- $T > T_N$: Magnetic moments are disordered. Thermal fluctuations dominate.

3.4 Synthetic Antiferromagnetic Materials (SAF):

While the previous antiferromagnetic state was due to the lattice configuration and composition of the material, synthetic antiferromagnets can be engineered by putting two ferromagnetic materials separated by a non-magnetic layer, as shown in Figure 4b. This magnetic interaction is called Ruderman-Kittel-Kasuya-Yosida (RKKY) coupling, with an associated energy given by [15, 25, 26]

$$E_{\mathrm{RKKY}} = -J_{\mathrm{RKKY}}(\hat{M}_1 \cdot \hat{M}_2), \tag{9}$$

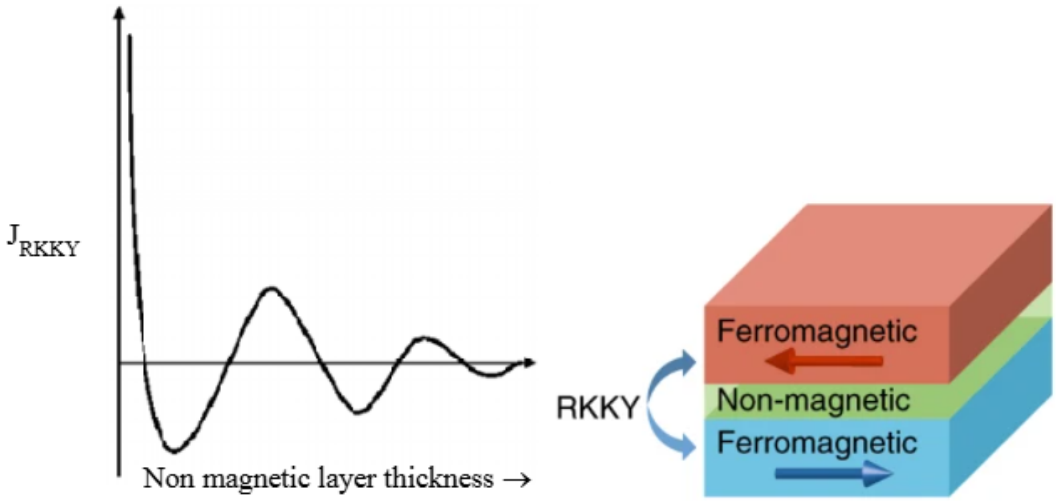
where J_{RKKY} is the RKKY coupling constant and $\hat{M}_i$ the different magnetisation orientations.

Figure 4a shows how the exchange constant depends on the non-magnetic layer thickness. According to the layer thickness the coupling could change from ferromagnetically coupled ($J_{RKKY} > 0$) to antiferromagnetically coupled ($J_{RKKY} < 0$). Another noteworthy point is that the exchange constant can be tuned according to the layer thickness to enhance or reduce the exchange interaction, offering many possibilities for optimization in spintronic devices [15].

3.5 Magneto-optical effects:

In addition to magnetic-magnetic interactions, there also exist interactions between light and magnetism. The first observed magneto-optic effect is the Faraday effect, when a magnetic field is applied along the propagation direction of the light, it will induce a rotation in the polarization of the light.

Another magneto-optic effect is the Kerr effect, which is the change in light polarization after its reflection from a magnetic material. This technique is of high interest for the magnetic characterization of magnetic thin films, as it allows easy access to the magnetic state of the materials, either from a static imaging or even for ultrafast imaging [32].



(a) (b)

Figure 4: (a) Oscillation of the exchange constant as a function of the non-magnetic layer thickness, image taken from [25], (b) Schematic structure of a single synthetic antiferromagnetic layer, image taken from [15]

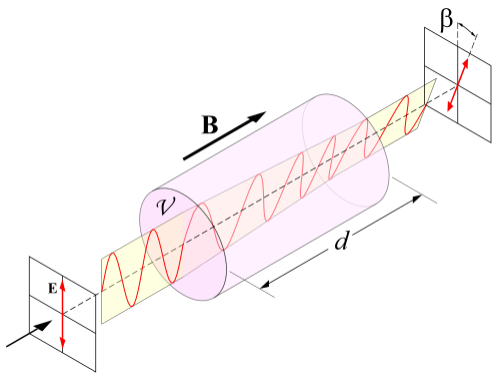


Figure 5: Rotation of the light polarization in a material subjected to an applied magnetic field, image taken from [16].

3.6 Evolution of Magnetoresistance from AMR to TMR:

Another interesting effect in magnetism is the effect of magnetization on the electronic transport properties. According to an external applied field, or even the intrinsic magnetic moment of the material, the electronic transport properties such as the resistance can change.

Due to this change in resistance, two states can be defined, one with a high resistance value, and another one with a low resistance value. From these two resistance states, the magnetoresistance (MR) ratio can be defined as [17]:

$$\mathrm{MR} = \frac{R_{\max} - R_{\min}}{R_{\min}} \tag{10}$$

This phenomenon is the magnetoresistance, it was discovered in 1857 by Thomson along

with the anisotropic magnetoresistance (AMR), where the resistance of the material varies according to the applied field angle and magnitude. However the AMR is limited to a few percent or even less [17].

In order to obtain a larger MR ratio, optimization through nanofabrication process to fabricate spin valve structure started in the 1980s, this kind of structure allow Giant Magnetoresistance (GMR). On Figure 6 is represented the architecture of the spin valve, it is composed of 2 magnetic layers, the reference and the free layer, separated by a non-magnetic layer. Usually for a GMR device, the non-magnetic layer is a metallic spacer such as copper. The reference layer has usually a fixed magnetization orientation, while the free layer could be switched by an external magnetic field or other means [17, 18].

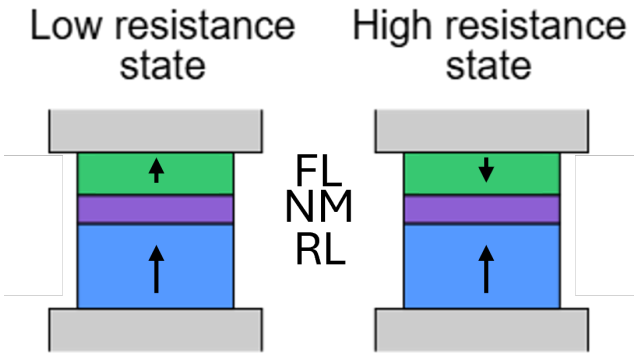


Figure 6: Architecture of a spin valve structure, black arrows indicate the magnetization direction of the thin films, gray squares are the electrical contacts, green squares are the free magnetic layers (FL), blue squares are the pinned magnetic layers (RF), violet squares are non-magnetic spacers (NM), image adapted from [19]

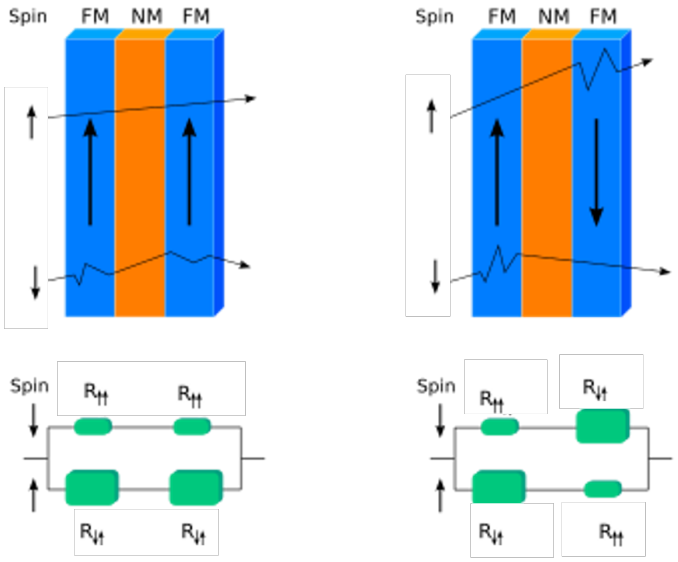
As shown on Figure 7 the conduction in spin valves could be modeled as a two-channel conduction path, one for each spin orientation. The electrical current could be modeled as two spin currents flowing in the same direction, and each spin current will have a different scattering length due to the magnetization of the thin film [21, 22]. If both thin films have parallel magnetization, electrons with the same spin polarization will see a low resistance state due to low scattering mechanism. While if the thin films have antiparallel magnetization, both spin population will observe middle resistance.

$$R_{\mathrm{P}} = \frac{2R_{\uparrow\uparrow}R_{\uparrow\downarrow}}{R_{\uparrow\uparrow} + R_{\uparrow\downarrow}} \tag{11}$$

$$R_{\mathrm{AP}} = \frac{R_{\uparrow\uparrow} + R_{\uparrow\downarrow}}{2} \tag{12}$$

$$R_{\mathrm{P}} < R_{\mathrm{AP}} \tag{13}$$

While GMR has a higher MR ratio, it is still limited to $10 \sim 50\%$. In order to further improve MR ratio, the spacer layer can be modified from a metallic spacer to an insulating spacer layer such as AlO or MgO. Due to this oxide layer, there is tunneling happening



(a) (b)

Figure 7: (a) Parallel configuration (P) of the GMR on the left and two-channel model of the resistance, (b) Antiparallel configuration (AP) of the GMR on the right and two-channel model of the resistance, image adapted from [17, 20]

according to the spin density of states (DOS), This process is known as tunneling magnetoresistance (TMR) [17, 23]. Figure 8 shows the tunneling between the DOS according to the P or AP configuration. Table 1 summarizes the difference between GMR and TMR.

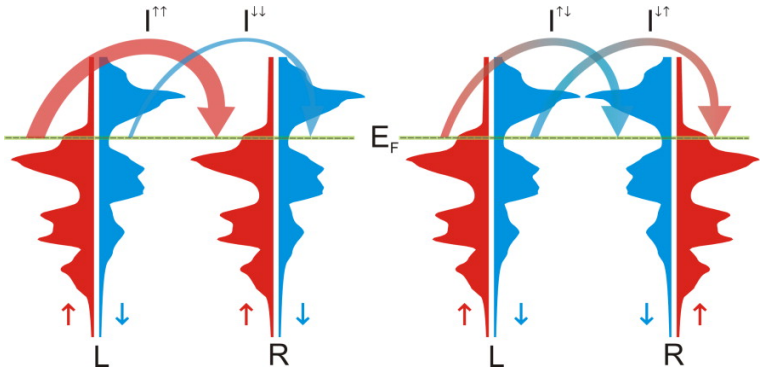


Figure 8: Density of states and current for the P and AP configurations for TMR, image taken from [17]

Table 1: Comparison between GMR and TMR

	GMR	TMR
MR ratio	$> 10\%$	$> 100\%$
Mechanism	Electron scattering	Tunneling
Resistance	$\sim 100\ \Omega$	$\sim 10\ \text{k}\Omega$
NM layer	Cu, metals	MgO, AlO, Oxides

3.7 Spin-Transfer Torque (STT):

An interesting feature of spin valve architecture is the fact that the magnetization of the free layer could be switched through an electrical current. When an unpolarized electron flow passes through one of the magnetic layer, it will become polarized and could transfer spin angular momentum from one layer to another, to switch the magnetic state of the free layer [24].

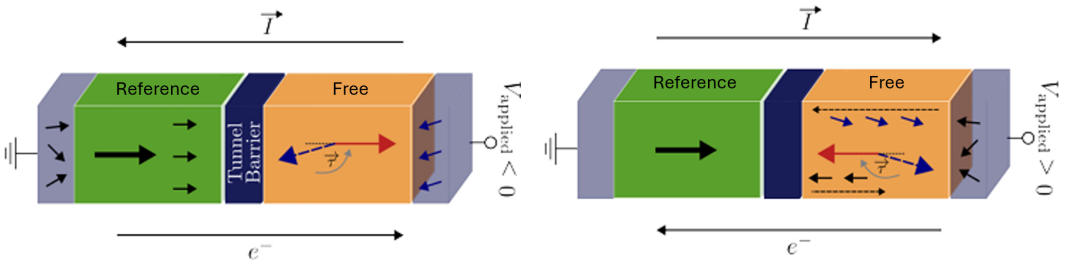


Figure 9: Schematic of the spin transfer torque switching, (a) from AP to P, (b) from P to AP, the blue arrows indicate the initial magnetization and the red arrows indicate the final magnetization, images adapted from [7]

Figure 9 shows the switching from AP to P state, and from P to AP state. On Figure 9a, to switch from the AP to P configuration, an unpolarized electron flow passes through the reference layer and becomes spin polarized, when tunneling through the free layer, the polarized electron will generate a torque on the free layer, if the torque is strong enough it will switch the magnetization of the free layer. On Figure 9b, to switch from the P to AP configuration, an unpolarized electron flow passes through the free layer and becomes spin polarized. The electron with the same polarization as the reference layer will tunnel through the tunnel barrier, while electrons with the opposite spin will be backscattered and exert an opposite torque on the free layer [7].

STT devices such as Magnetic Tunnel Junction (MTJ) are used for memory applications. Some figures of merit for STT could be defined in the following way [8, 7, 27]:

3.7.1 Reading STT:

The readability of the device corresponds to a measurable change in resistance value between P and AP states. It is the definition of the TMR:

$$\mathrm{TMR} = \frac{R_{\mathrm{AP}} - R_{\mathrm{P}}}{R_{\mathrm{P}}} \tag{14}$$

3.7.2 Writing STT:

To account for the current influence in magnetization reversal of the free layer, the magnetization dynamics could be studied with the Landau-Lifshitz-Gilbert-Slonczewski (LLGS) equation [27]:

$$\frac{\partial \overrightarrow{m}}{\partial t} = \overrightarrow{\Gamma}_{\mathrm{prec}} + \overrightarrow{\Gamma}_{\mathrm{damp}} + \overrightarrow{\Gamma}^{\mathrm{IP}}_{\mathrm{STT}} + \overrightarrow{\Gamma}^{\mathrm{P}}_{\mathrm{STT}} \tag{15}$$

$$\overrightarrow{\Gamma}_{\mathrm{prec}} = -\gamma\mu_0 \overrightarrow{m} \times \overrightarrow{H} \tag{16}$$

$$\overrightarrow{\Gamma}_{\mathrm{damp}} = -\alpha\gamma\mu_0 \overrightarrow{m} \times (\overrightarrow{m} \times \overrightarrow{H}) \tag{17}$$

$$\overrightarrow{\Gamma}^{\mathrm{IP}}_{\mathrm{STT}} = \gamma\mu_0\eta \frac{\hbar J}{2eM_{\mathrm{s}}t} \overrightarrow{m} \times (\overrightarrow{m} \times \overrightarrow{m}_{\mathrm{RL}}) \tag{18}$$

$$\overrightarrow{\Gamma}^{\mathrm{P}}_{\mathrm{STT}} = \gamma\mu_0\eta' \frac{\hbar J}{2eM_{\mathrm{s}}t} \overrightarrow{m} \times \overrightarrow{m}_{\mathrm{RL}} \tag{19}$$

With $\overrightarrow{m}$ the magnetization of the free layer, $\overrightarrow{m}_{\mathrm{RL}}$ the magnetization of the reference layer, $\overrightarrow{H}$ the effective magnetic field, α the Gilbert damping, γ the gyromagnetic ratio, μ_0 the vacuum permeability, J the current density, t the free layer thickness, η the spin transfer efficiency [27]. And $\overrightarrow{\Gamma}$ the applied torques on the magnetic moment are shown on Figure 10b, the damping torque $\overrightarrow{\Gamma}_{\mathrm{damp}}$ acts to align the magnetic moment and the field $\overrightarrow{H}$, the damping-like torque $\overrightarrow{\Gamma}^{\mathrm{IP}}_{\mathrm{STT}}$ can either enhance the damping or counteract it depending on the current direction, the precession torque $\overrightarrow{\Gamma}_{\mathrm{prec}}$ induces a precession of the magnetic moment around the applied field $\overrightarrow{H}$, and the field-like torque $\overrightarrow{\Gamma}^{\mathrm{P}}_{\mathrm{STT}}$ can enhance or dampen the precession around the field [27].

The current necessary to obtain the perpendicular magnetization reversal should be high enough, so the damping-like torque can counteract the damping torque [27].

$$\overrightarrow{\Gamma}_{\mathrm{damp}} = \overrightarrow{\Gamma}^{\mathrm{IP}}_{\mathrm{STT}} \tag{20}$$

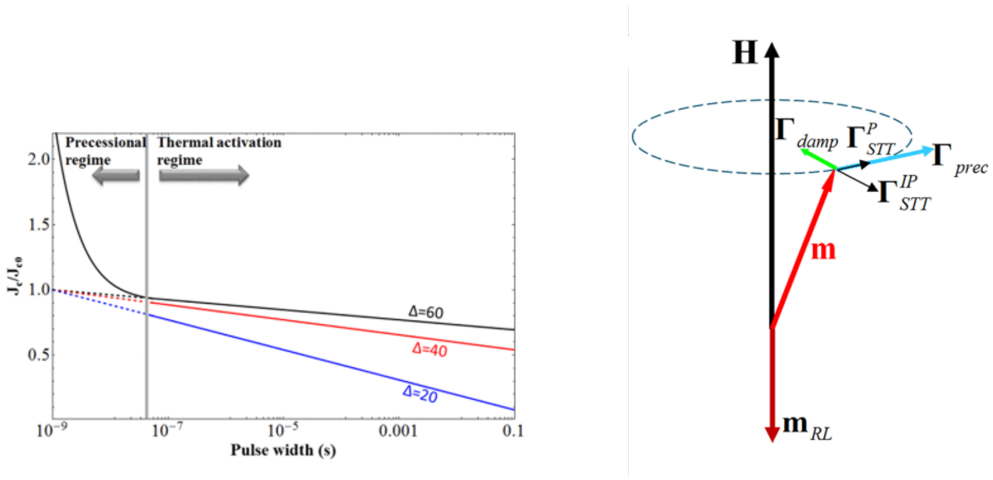
$$-\alpha\gamma\mu_0 \overrightarrow{m} \times (\overrightarrow{m} \times \overrightarrow{H}) = \gamma\mu_0\eta \frac{\hbar J_{c0}}{2eM_{\mathrm{s}}t} \overrightarrow{m} \times (\overrightarrow{m} \times \overrightarrow{m}_{\mathrm{RL}}) \tag{21}$$

$$J_{c0} = \frac{\alpha 2eM_{\mathrm{s}}tH_K}{\hbar\eta} \tag{22}$$

Moreover, according to the current pulse width, the switching will come from different physical processes, and it will impact the current density necessary for switching. At short pulse width, it will be in the precessional regime, and at long pulse width, it is in the thermally activated regime [27]. At short pulse width, the current density increases as shown on Figure 10a.

3.7.3 Stability STT:

Another important figure of merit for STT device is the thermal stability, which corresponds to the data retention time. It is related to the energy barrier (E_B) to overcome going



(a) (b)

Figure 10: (a) Evolution of current density according to current pulse width for different thermal stability, (b) Representation of torques applied on the free magnetic moment, images taken from [27]

from one configuration to another. The energy barrier comes from anisotropy, such as shape anisotropy, interfacial anisotropy and magnetocrystalline anisotropy [7].

$$\Delta = \frac{E_B}{k_B T} = \frac{K_{\text{eff}} V}{k_B T} \tag{23}$$

3.8 All Optical Switching (AOS) and ultrafast spin dynamics:

In the last sections, we described that magnetization could be reversed from an applied magnetic field or current. However, an ultrafast laser beam can also induce magnetization reversal, such as in ferrimagnetic alloys [28].

Figure 11 shows the ultrafast heating induced by optical excitation, can lead to magnetization reversal in ferrimagnetic alloys. The mechanism is effective due to a difference in demagnetization rates between the Gd and Fe sublattices. The Fe sublattice is completely demagnetized after 300 fs, while the Gd sublattice demagnetizes after 1.5 ps. This leads to a ferromagnetic alignment of Fe and Gd at short timescale, during the non-equilibrium state between the two sublattices [28]. Due to angular momentum exchange, the antiparallel alignment is recovered after a few picoseconds, with both sublattices having switched magnetization.

Similarly, in spin valve structure ultrafast magnetization reversal could also happen, due to angular momentum transfer between the reference and free layer. From angular momentum conservation, when one of the layer demagnetizes, it should generate a polarized spin current that may switch the other layer [30].

Figure 12 shows some spin valve architecture for AOS, as well as describing the mechanism for magnetization reversal in spin valve. Even though the magnetization reversal from P to AP state is still debated, some mechanisms are proposed to explain this reversal [30].

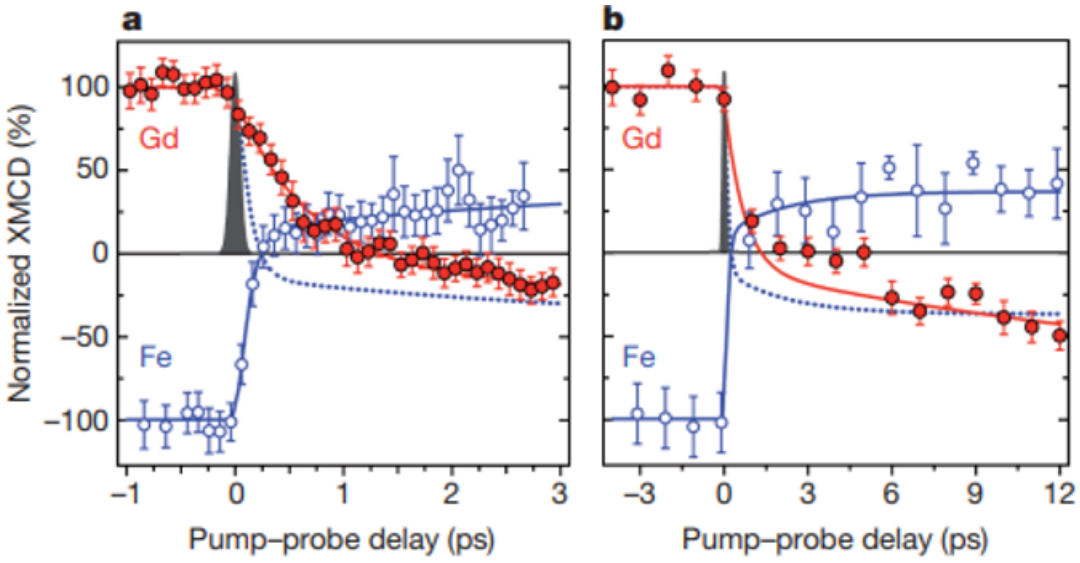


Figure 11: Magnetization dynamics induced by an optical excitation of GdFe, image taken from [28]

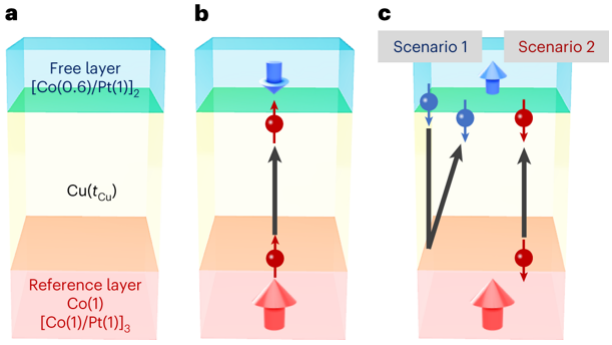


Figure 12: Spin valve structure, (a) Composition of the spin valve, (b) Magnetization reversal from AP to P, (c) Magnetization reversal from P to AP, blue electrons are generated from the free layer, red electrons are generated from reference layer, image taken from [30]

- Scenario 1: similarly to STT, the free layer generates a minority spin current that flows through the spacer layer, and is reflected back by the reference layer
- Scenario 2: during remagnetization the reference layer could pump back the magnetization lost through minority spin current

The mechanism to switch from AP to P configuration, is due to the spin current generated during demagnetization. While the mechanism to switch from P to AP configuration, could come from the remagnetization of the reference layer [31].

Based on this introduction on magnetism and spintronics fundamentals, we saw the basic structure for a spin valve, as well as some magnetization reversal mechanisms. The magnetization of a spin valve could be reversed, through an applied field, a current or a optical excitation. In the next section, we will explain the optimization of thin films to combine AOS and STT, and to define a fabrication process flow to fabricate spin valves.

4 Fabrication of STT devices:

In the context of this work, we aim to combine All-Optical Switching (AOS) and Spin-Transfer Torque (STT), as both mechanisms might lead to more energy efficient devices [30]. To combine both mechanisms, an architecture investigated is the spin valve, as both mechanisms have already been observed in spin valves.

4.1 Optimization of Thin Films for STT and AOS

In order to have a thin film that could be used for both STT and AOS, some studies have been necessary. We have grown a perpendicular spin valve structure (Figure 13), composed of (from the bottom-up): (Si/SiO_2) | Ta (3) | Pt (10) | [Co (X) / $Pt(0.5)]_5$ | Ir (0.72) | [Co (X) / $Pt(0.5)]_2$ | Co (X) | Cu (5) | [Ni (0.6) / Co $(0.2)]_2$ / Cu (5) | Pt (3) in parenthesis is the thickness of the layer in nanometers. Individually, each layer/multilayer, serves a different purpose. The Ta layer serves as an adhesion layer to the Si/SiO_2 substrate and Pt is a buffer for the correct growth of the Co/Pt multilayer with perpendicular anisotropy. This initial set of multilayers are coupled to the Co/Pt reference layer through a Ir spacer, forming a synthetic antiferromagnetic layer (subsection 3.4) because of the RKKY coupling. Our free layer is composed of Ni/Co multilayers, and separated by the reference layer by a layer of Cu, commonly used in GMR stacks. The following Cu and Pt layers serve as capping layers for oxidation prevention and further fabrication. The reference layer used was a synthetic antiferromagnetic, in order to compensate the magnetic field generate by the reference layer, the top SAF creates a magnetic field in +z-axis, while the bottom SAF generates a magnetic field in −z-axis. To study different parameters, the thickness of Co is varied in the SAF, with $X \in \{0.6, 0.7\}$ nm. The details of the thin film optimisation done are described in the following section.

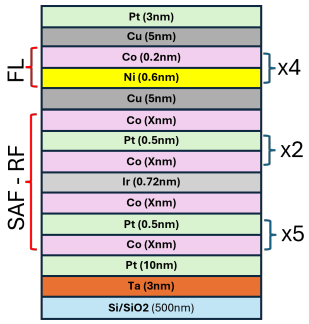


Figure 13: Thin Film composition for AOS-STT sample, on the rigth of the thin film are presented the number multilayers, on the left are presented the function of each multilayer (FL : Free Layer, SAF-RF : Synthetic Antiferromagnetic - Reference Layer)

Three optimization steps were done in our thin film, for both SAF and free layer. First, a study on the thickness of the Ir spacer layer to have an antiferromagnetically coupled reference layer. Second, a study to have a perpendicular magnetic free layer. And third, an investigation about the Co thickness to have AOS.

4.1.1 Investigation of Ir thickness to obtain an antiferromagnetically coupled layer

In order to study RKKY interaction between the [Co/Pt] multilayer and the Ir layer, a wedge-shaped thin film was grown and characterized at *Institut Jean Lamour*. The growth of the thin film was made by Magnetron Sputtering deposition and consists of: Si/SiO2 (500) | Ta (3) | Pt (5) / [Co (0.4) / Pt (0.5)]$_2$ | Co (0.4) | Ir (wedge: 0.2 to 1.0) | Co (0.4) - [Co (0.4) / Pt (0.5)]$_5$ | Pt (2) (thicknesses in nm) as shown on Figure 14a.

To characterize the antiferromagnetic coupling between the multilayers as a function of the Iridium thickness Figure 14b, we used a Kerr Magnetometer from *Institut Jean Lamour*, to measure the Kerr rotation and Kerr ellipticity for different Ir thicknesses.



(a) (b)

Figure 14: Thin film composition for RKKY optimization of Iridium thickness, (a) Multilayer optimization of the SAF, (b) Definition of Ir wedge

The Kerr magnetometer uses the Kerr effect to access the magnetic state of the system. Through a laser irradiation on a magnetic sample, the light polarization could change, and through the use of a PhotoElastic Modulator (PEM) and a lock-in amplifier, the Kerr rotation and ellipticity could be measured during the same measurement.

The light intensity at the output of the analyzer could be expressed as a function of Bessel functions, and from the use of a lock-in amplifier, it gave access to both Kerr rotation and ellipticity [32]. The signal measured by the photodetector is expressed as:

$$I = I_0(1 - 2\theta J_0(\delta_0) + 4\eta J_1(\delta_0)\sin(2\pi f t) - 4\theta J_2(\delta_0)\cos(4\pi f t)) = I_{\mathrm{DC}} + I_{1f} + I_{2f} \qquad (24)$$

- I_0 is DC current generated from the incident light
- θ is the Kerr rotation
- δ_0 is the retardation phase of the function
- η the Kerr ellipticity
- f the frequency of the lock-in amplifier
- t the time

It should be noted that one could tune the δ_0 retardation phase to obtain more signal from the Kerr rotation or ellipticity, in our case we used an intermediate value of δ_0 to

obtain both signals in the same measurement. The expression of the signal measured by the photodetector, allows a direct expression of the Kerr values [32]:

$$\theta = \frac{I_{2f}}{-4I_0 J_2(\delta_0)}, \tag{25}$$

$$\eta = \frac{I_{1f}}{4I_0 J_1(\delta_0)}. \tag{26}$$

Using an electromagnet from -700 mT to 700 mT, we observed the Kerr rotation of the thin film as a function of the Ir thickness. According to the nature of the hysteresis curve, this gives information about the ferromagnetic or antiferromagnetic coupling of the [Co/Pt] multilayers.

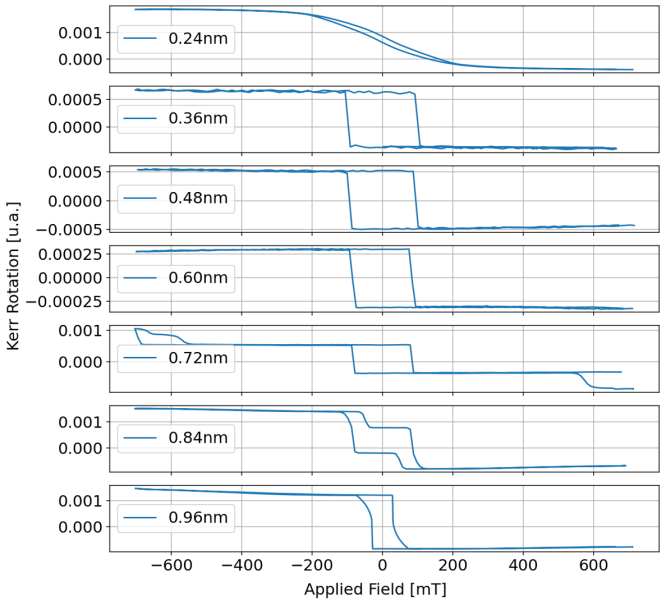


Figure 15: Measured Kerr signal as a function of an applied perpendicular magnetic field for different Ir thickness.

From Figure 15, we could remark a few things. First of all, below 0.24 nm, the magnetization of the multilayer seems to become in-plane, while we are looking for out-of-plane magnetization. Meanwhile from 0.36 nm to 0.6 nm, we observe that the magnetization is completely out-of-plane from the hysteresis loop, however we could not observe the second switching due to the second magnetic layer, meaning we could not assume if it is antiferromagnetic or ferromagnetic coupling. Finally from 0.72 nm, we observed the antiferromagnetic coupling between the multilayers, through the multiple switchings of the layers. For the fabrication of Spin Valves, we will use RKKY coupling between [Co/Pt] | Ir | [Co/Pt] with 0.72nm of Iridium to ensure that we have a Synthetic antiferromagnet, even though the coupling could be optimized with a better characterization of the coupling constant according to Iridium thickness. A further investigation could be done through the use of Vibrating Sample Magnetometer (VSM) to obtain extended hysteresis curve.

4.1.2 Investigation of the bottom layer for perpendicular magnetization of Co/Ni layer

After this optimization of the reference layer, the free layer also needed to be optimized. Our first idea was to deposit the free layer on a transparent substrate to allow easier access for AOS exposure. In this context, we tried different compositions of the seed/bottom layer to obtain perpendicular magnetization in the [Co/Ni] multilayers.

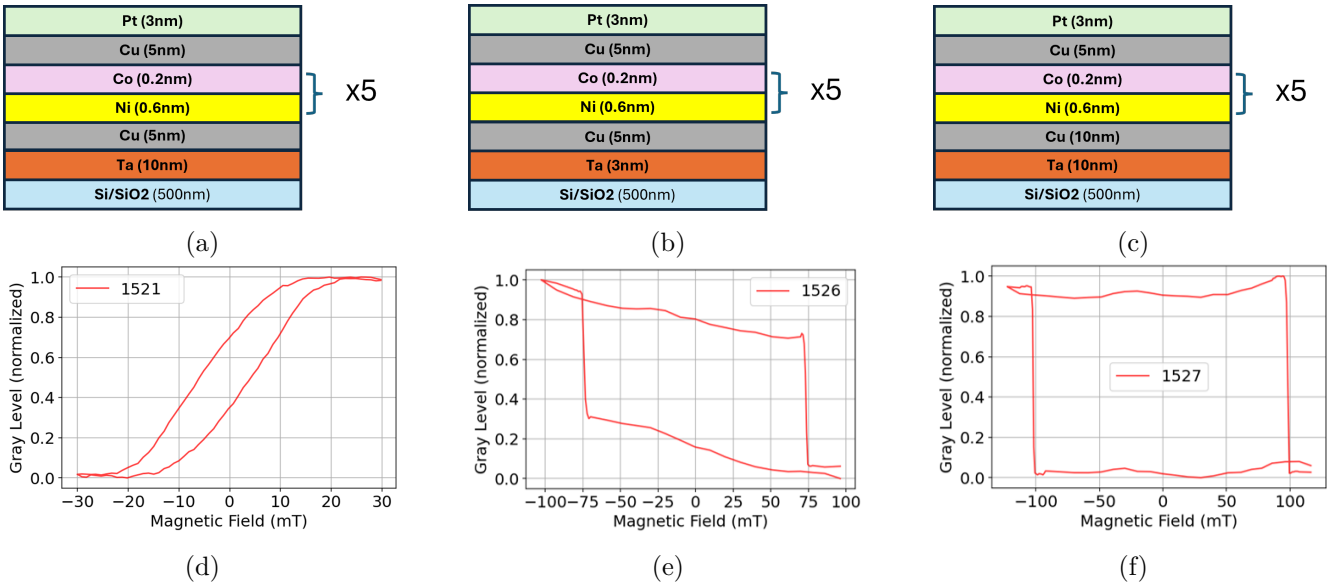


Figure 16: Different compositions of the bottom layer and their normalized out-of-plane hysteresis, (a, c) Thin film 1521 and its out-of-plane hysteresis, (b, d) Thin film 1526 and its out-of-plane hysteresis, (c, e) Thin film 1527 and its out-of-plane hysteresis

It can be observed from figs. 16a and 16d, that due to the thick layer of Ta (10 nm) the magnetization of the [Co/Ni] multilayer became in-plane due to crystalline structure of tantalum that differs according to Ta thickness. Two ways to obtain perpendicular magnetization were tested: reducing the Ta thickness (figs. 16b and 16e), and increasing the Cu thickness to limit the influence from Ta (figs. 16c and 16f).

Both approaches allowed to obtain a perpendicular magnetization for the [Co/Ni] multilayer. This study might become relevant when moving from a silicon to a glass substrate for AOS.

4.1.3 Investigation of Co Thickness to Obtain Different Curie Temperature, and Influence on AOS

After the previous optimization steps, the following spin valve structures have been defined and characterized on Vibrating Sample Magnetometer (VSM).

As seen on Figure 17, 5 different thin film compositions have been tested. One of the first ideas, shown on figs. 17a and 17f was to grow the ferromagnetic layer on direct contact with the silicon substrate, that way by switching to glass substrate we could easily access the ferromagnetic layer for AOS. Figure 17f shows the out-of-plane hysteresis curve of the sample

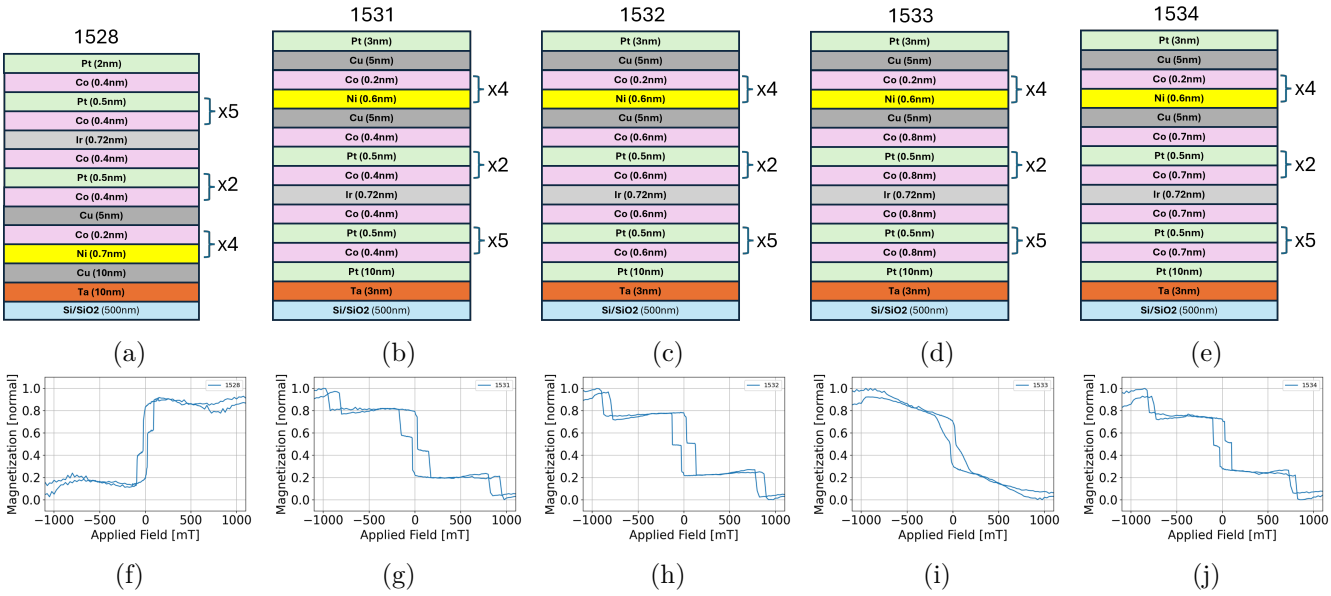


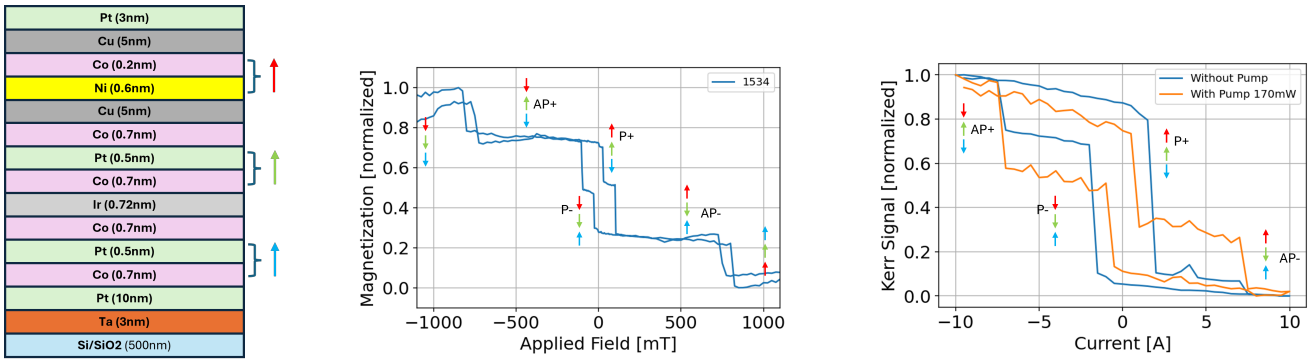
Figure 17: All fabricated thin films for STT-AOS optimization, the thin-film compositions on top and their out-of-plane hysteresis curves on the bottom measured using VSM, (a, f) thin film **1528**, (b, g) thin film **1531**, (c, h) thin film **1532**, (d, i) thin film **1533**, (e, j) thin film **1534**

from −1.5 T to 1.5 T, on the center of the curve between −250 mT to 250 mT, the reversal of the free and the top reference layers could be observed. However, the free and reference layer might not be fully aligned at high field, which can be detrimental.

From these results, we decided to reverse the reference and the free layer disposition (figs. 17b to 17e). In this case, to access the magnetic layer we will need to resort to a transparent top electrode such as Indium Tin Oxide (ITO) [33]. Through figs. 17b, 17c, 17e, 17g, 17h and 17j, it can be observed that by switching the reference and free layer, the perpendicular magnetization could be kept even by varying the Cobalt thickness in the [Co/Pt] multilayer.

However, from figs. 17d and 17i it could be observed that a too thick layer of Co (0.8 nm) from the SAF has an important effect on the hysteresis curve. From the hysteresis curve, we observed a curvature close to 0 mT, and the switching of each layer could not be determined anymore, this might be an effect of the reduction of the interfacial anisotropy, and so the thin film might have an in-plane magnetization.

Based on these characterization results, we perform AOS measurements on the thin films with stack structures **1532** and **1534**. It should be noted that, as the Co thickness is quite thick, it should have a high Curie temperature, which will be relevant for AOS. Before doing AOS measurement, we should define the name for each magnetic configuration. On Figure 18a, 3 arrows have been defined, one for each magnetic layer. They are reported on Figure 18b which is the VSM measurement of the thin film, and on Figure 18c which is the measurement of the Kerr signal on the AOS laser setup. In order to facilitate AOS measurement, the difference between the higher and lower plateaus should be as high as possible on the blue curve to obtain the best contrast possible for latter image processing.



(a) (b) (c)

Figure 18: On (a) each arrow represents its corresponding layer for the thin film **1534**, (b) measurement of the magnetization of the thin film using VSM, (c) measurement of magnetization of the thin film using the Kerr effect, note that the X-axis is in Amperes as we are using an electromagnet, in blue the Kerr signal of the whole substrate, in orange the Kerr signal on the laser spot

A good contrast on Figure 18c will allow to have a clear definition of the states. Furthermore, another noteworthy point is the difference between the blue and the orange curves. The blue curve corresponds to the complete Kerr signal of the image, while the orange curve corresponds to the Kerr signal on the laser spot, it could be seen that on the laser spot the switching to another state happens at lower current (thus field), due to Heat Assisted Magnetization Reversal (HAMR) [34].

In order to study the magnetization dynamics and reversal of the spin valves, a Time-Resolved MOKE (TR MOKE) setup must be used. On Figure 19, is represented a 3D view of the experimental TR-MOKE setup (image taken from [35]), a Light Conversion PHAROS amplified laser is used to generate ultrafast laser pulses at high energy. The laser pulse has a wavelength of 1030 nm, and its pulse duration ranges from 300 fs to 10 ps. On the setup is also integrate a pulse picker to tune the repetition rate of the laser, and to control the number of pulses irradiating the sample. Afterward, the laser passes through 2 Light Conversion ORPHEUS Optical Parametric Amplifier (OPA), in order to modify the output wavelength from 300 nm to 1600 nm. The main output of the laser can directly be used as the pump to reverse the magnetization of the sample, and to generate the probe, it could pass through a Beta Barium Borate (BBO) crystal to generate the probe light at 550 nm [37]. It should be noted, that all the following experiment were realized with a repetition rate of 50 kHz and a laser pulse duration of 300 fs.

In order to study magnetization dynamics, we need to be able to control the power of the pump, as well as the delay between the probe and the pump. To control the power of the pump, a half-wave plate is coupled with a polarizer at the output of the pump laser, by changing the angle of the half-wave plate, the power of the pump can be tuned. To control the delay between the pump and the probe, a delay line is inserted in the optical path of the pump beam.

Figure 20 shows some ultrafast dynamics measurement using TR-MOKE setup, for the thin film **1534**. On Figure 20a, we start by saturating the sample with ± 10 A so in AP$\mp$

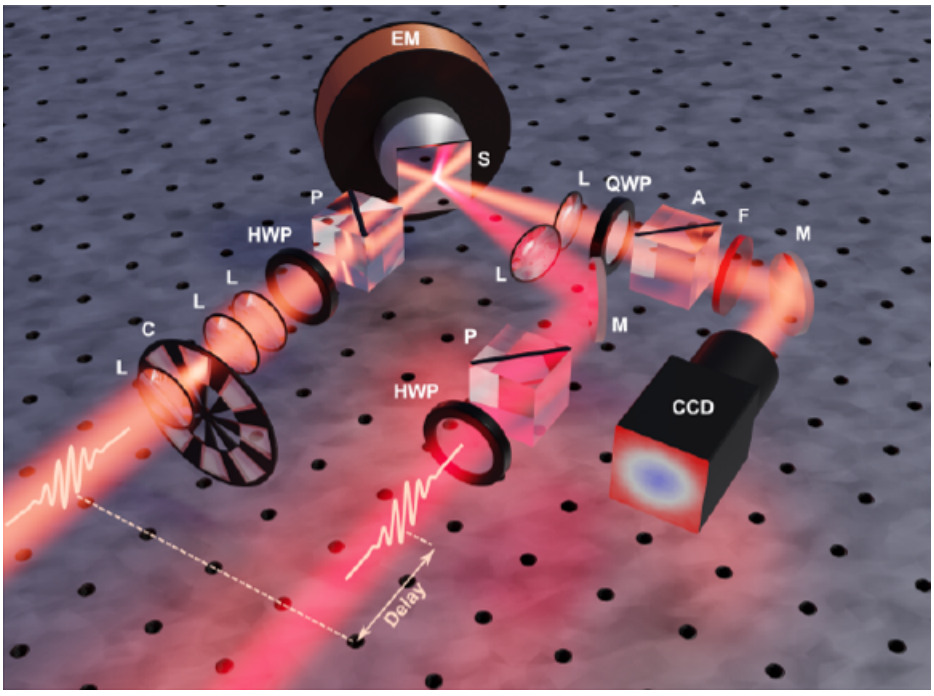
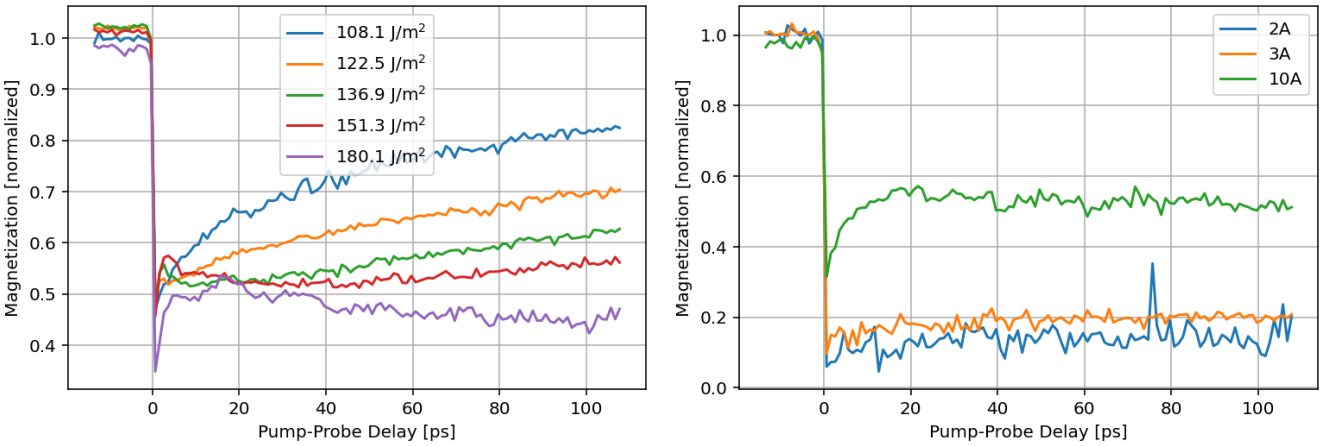


Figure 19: TR MOKE setup, HWP : half-wave plate, QWP : quarter-wave plate, P : polarizer, A : analyzer, C : chopper, S : sample, EM : electromagnet, M : mirror, L : lens, F : filter, CCD Camera : Charge Coupled Device camera, the pump (1030 nm) in red, the probe (550 nm) in orange, image taken from [35] chapter 4.3.4 TR-MOKE Microscopy



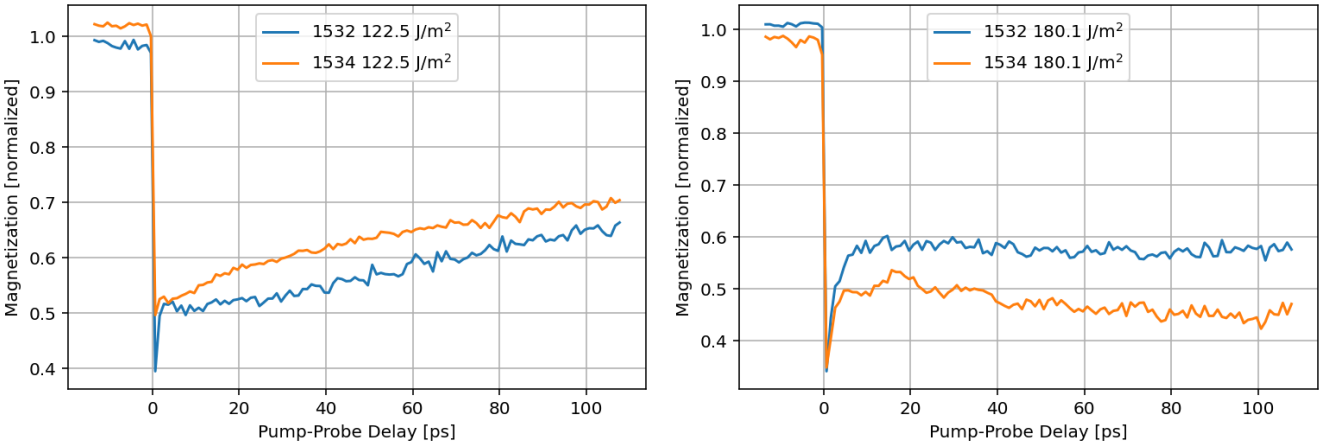
(a) (b)

Figure 20: TR MOKE experiments on thin film **1534**, (a) Evolution of the magnetization dynamics as a function of different applied fluences, in the labels are the applied fluences, (b) Evolution of the magnetization dynamics as a function of the different applied fields, for a fluence of 180.1 J/m^2

state (fig. 18c), and we take a background image every time for latter image processing, the pump irradiates the sample causing the demagnetization of the magnetic layers. Different laser fluences were tested to switch the sample from AP to P state, however even at high

fluence we could only observe demagnetization and remagnetization of the sample. By further increasing the fluence of the laser beam, we started to burn the sample.

Figure 20b shows the same experiment as in fig. 20a, but using a different saturating current for the initialization. A higher demagnetization could be observed, but not yet the switching from AP to P.



(a) (b)

Figure 21: (a) Comparison of the magnetization dynamics of the thin films **1532** and **1534** at 122.5 J/m^2, (b) Comparison of the magnetization dynamics of the thin films at 180.1 J/m^2

On Figure 21 are plotted the magnetization dynamics for **1532** and **1534** at different laser fluences. From this comparaison between the samples, we note that at low fluence (122.5 J/m^2) the thin film **1534** remagnetizes faster. While at high fluence (180.1 J/m^2), the thin film **1532** remagnetizes faster.

Until now, the switching from AP to P state in the thin films **1532** and **1534** could not be observed before burning the sample, with a pulse duration of 300 fs and a repetition rate of 50 kHz. However, from Figure 22 it could be seen that the switching of the layer also depends on the pulse duration, with a pulse duration of only 300 fs we might not be under the right conditions to obtain AP to P switching, increasing the pulse duration may solve this problem, although further investigation will be necessary.

Nonetheless, while the switching from AP to P could not be observed experimentally on our thin film, the switching from P to AP could be observed. The following protocol has been used Table 2:

The results from this experiment are shown on figs. 23 and 24. Figure 23a explains the different mechanisms happening at ultra-short timescale after the laser irradiation. That could be linked to Figure 23b, where all the transitions could be observed on the sample **1534**. This experiment confirms the switching from the P- (resp. P+) to AP- (resp. AP+) configuration from a single laser pulse at 300 fs and a fluence of 180.1 J/m^2.

Furthermore, from Figure 24 we could observe the partial imaging through MOKE imag-

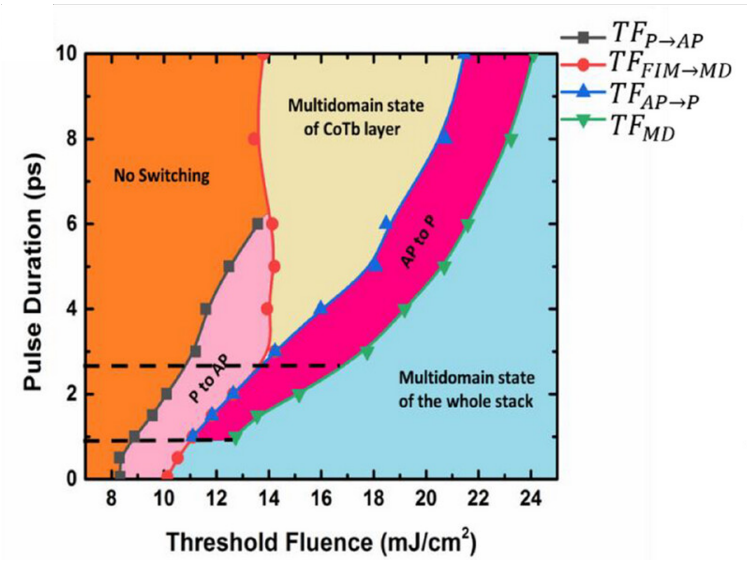


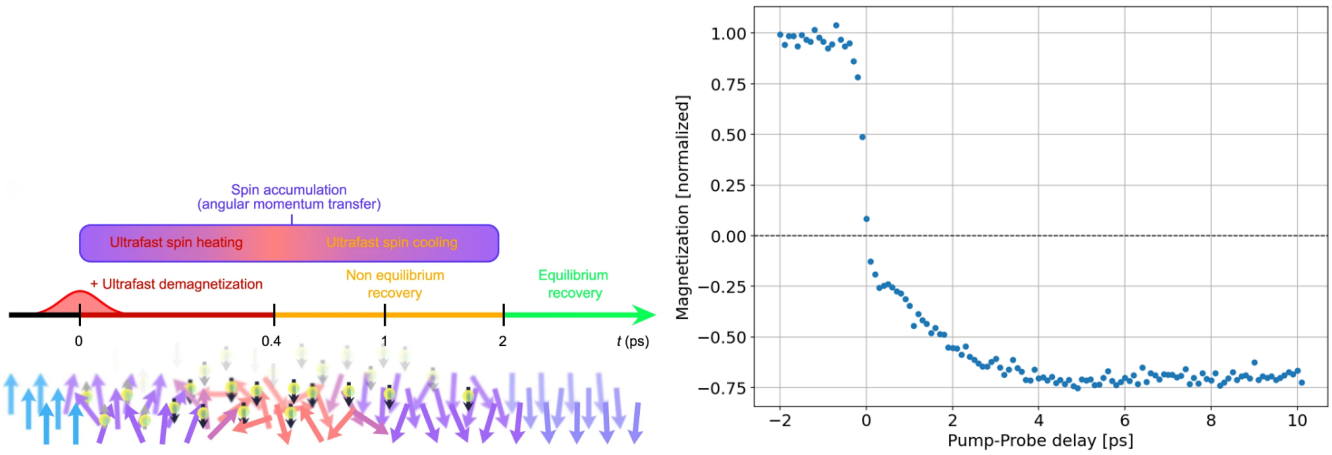
Figure 22: State Diagram for a ferrimagnetic spin valve, $TF_{P\to AP}$: Threshold fluence to observe P to AP switching, $TF_{AP\to P}$: Threshold fluence to observe AP to P switching, $TF_{FIM\to MD}$ Threshold fluence to observe multi-domains in the ferrimagnetic layer, TF_{MD} Threshold fluence to observe multi-domain in ferrimagnetic and ferromagnetic layers, image taken from [38]

Table 2: Measurement flow for P to AP characterization

Step	P- to AP-	P+ to AP+
1	Apply 10 A to initialize the AP- state.	Apply −10 A to initialize the AP+ state.
2	Apply −3 A to initialize the P- state.	Apply 3 A to initialize the P+ state for the P+ state.
3	Save a background image at 0 A for the P- state.	Save a background image at 0 A.
4	Apply a constant field at −1.25 A (to reinitialize the state between laser pulse).	Apply a constant field at 1.25 A (to reinitialize the state between laser pulse).
5	Apply the laser pulse and save the image.	Apply the laser pulse and save the image.

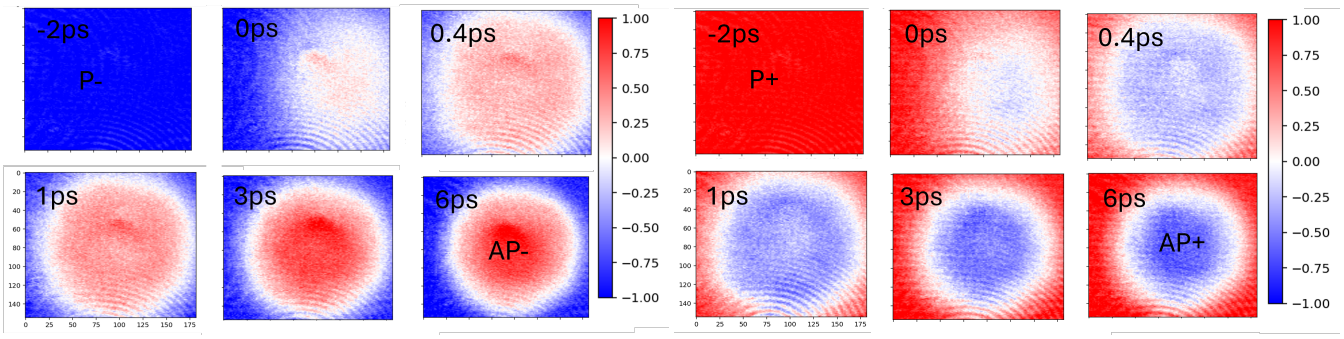
ing. Either starting from P- or P+ state, we observe the formation of a large area between 0 ps and 1 ps, that starts to stabilize after 2 ps it is correlated with the equilibrium recovery of magnetization.

This confirms the switching from P to AP in the sample **1534** through AOS, however it still needs to be confirmed for the sample **1532**. As well as to investigate the reversal from AP to P. Nonetheless, this proves that this kind of spin valve structures are a good candidate to obtain AOS, but they still need to be fabricated into nanostructures.



(a) (b)

Figure 23: (a) Dynamics of angular momentum transfer in ultrafast spintronics, image taken from [36], (b) TR MOKE experiment for the thin film **1534**, with a laser fluence of 180.1 J/m^2, from 0 fs to 200 fs is the ultrafast demagnetization regime, from 200 fs to 2 ps is the non-equilibrium recovery, and after 2 ps is the equilibrium recovery



(a) (b)

Figure 24: (a) Imaging of the transition from P- state to AP- state, (b) Imaging from the P+ state to the AP+ state

4.2 Process flow for the Fabrication of 4 Terminal STT Device

In subsection 4.1, the thin film composition and optimization have been explained. However, STT devices need to be patterned into nanopillars using the usual semiconductor fabrication process (Lithography, Etching and Deposition).

The process flow and fabrication were carried out on the following thin film:

- **1532**: Figure 25a
- **1534**: Figure 25b
- **H2**: Figure 25c
- **H3**: Figure 25d

The first two thin film were deposited at IJL, and were optimized to get both STT and AOS measurement. While the last two thin films were deposited at Tohoku University and were optimized for STT. These last samples will be used to verify whether the process flow

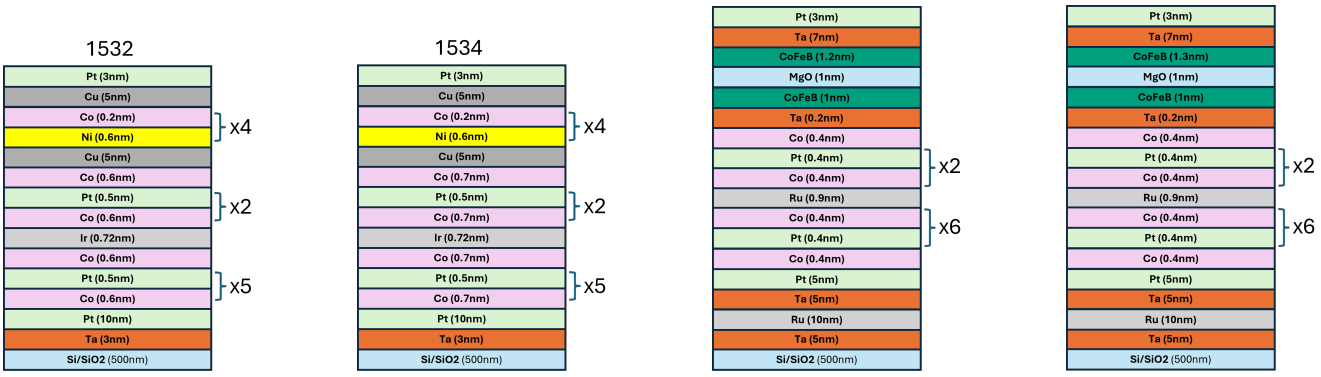


Figure 25: Thin films (a) **1532**, and (b) **1534**, have been deposited at IJL, while thin films (c) **H2**, and (d) **H3** have been deposited at Tohoku University

works for GMR devices, as these thin films are already known to have TMR ratio over 100% [39, 40]. The composition of **H2** and **H3** is from bottom to top: (Si/SiO_2) | Ta (5) | Ru (10) | Ta (5) | Pt (5) | Co (0.4) | $[Pt\ (0.4)\ /\ Co\ (0.4)]_6$ | Ru (0.9) | $[Co\ (0.4)\ /\ Pt\ (0.4)]_2$ | Co (0.4) | Ta (0.2) | CoFeB (1) | MgO (1) | CoFeB (X) | Ta (7) | Pt (3). The Ta layer served as an adhesion with the (Si/SiO_2), and Ru | Ta | Pt is a buffer layer for the correct growth Co/Pt multilayer with perpendicular anisotropy. The following set of multilayers Co/Pt coupled with Ru, forms a SAF to reduce the resulting magnetic field from the reference layer. The thin Ta layer serves two purposes, to absorb the boron from CoFeB after annealing, and to separate the two magnetic layer. The layer CoFeB (1) | MgO (1) | CoFeB (X), with X $\in \{1.2, 1.3\}$ nm, is the magneto tunneling junction. The top layer Ta | Pt serves to absorb the boron and to avoid oxidation thanks to Pt layer.

The following process flow and fabrication were performed in the cleanroom of the *Research Institute of Electrical Communication, Fukami-Kanai Laboratory*, where all the samples from Figure 25 have been patterned to obtain STT devices.

The devices have been patterned according to the following photomasks Figure 26, on Figure 26a is represented the completed layout that will be patterned on the sample. On figs. 26d and 26e are represented the two kinds of devices patterned. A device with only 2 terminals if we expect high GMR ratio, and another device with 4 terminals as the GMR ratio will likely be a few percent.

Here will be presented the main steps of the process flow, which consists of roughly 15 steps. Figure 27 shows the schematic process flow for the fabrication of nanopillars.

- $1 \rightarrow 2$: Spin coating of TGMR resist (200 nm) for electron beam lithography
- $2 \rightarrow 3$: Post baking and development of TGMR resist
- $3 \rightarrow 4$: Ion Beam Etching for nanopillars
- $4 \rightarrow 5$: Al_2O_3 deposition (28nm)
- $5 \rightarrow 6$: IBE of the side wall
- $6 \rightarrow 7$: Lift Off of Al_2O_3
- $7 \rightarrow 8$: Spin coating of photoresist and development
- $8 \rightarrow 9$: IBE to separate lower and upper electrodes
- $9 \rightarrow 10$: Al_2O_3 deposition (70nm)

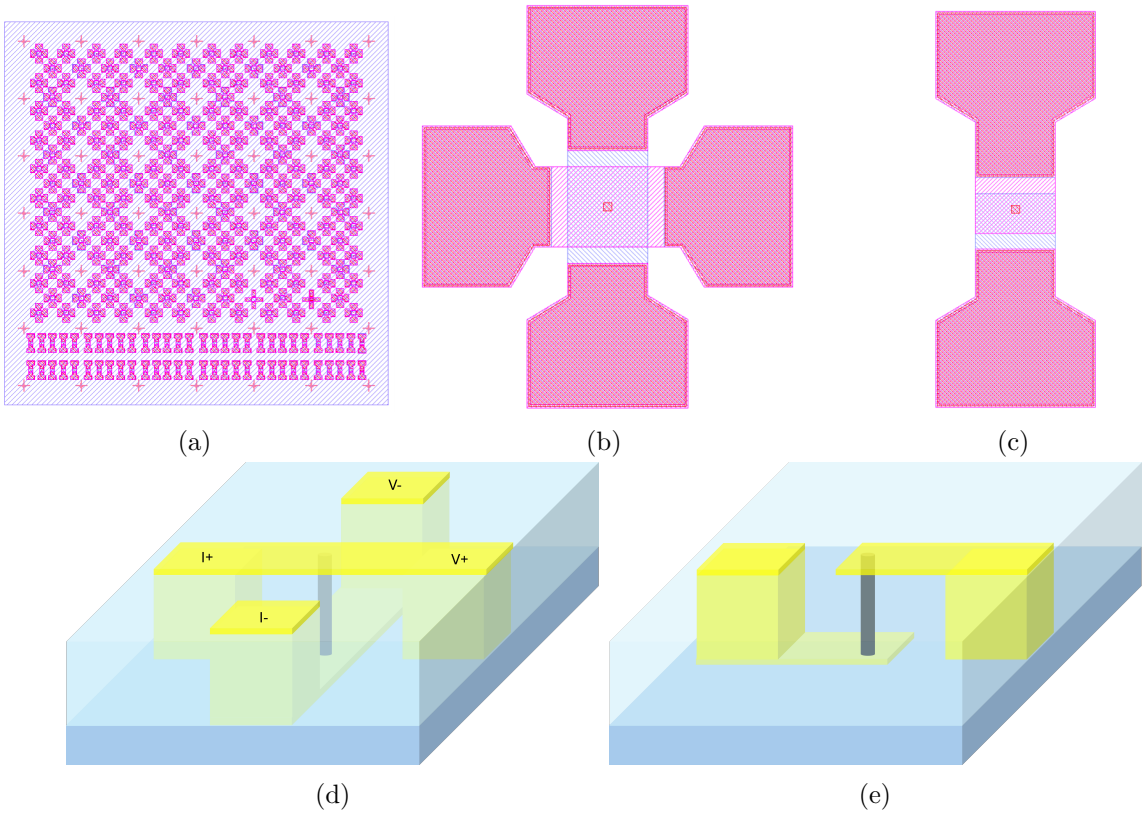


Figure 26: Layout of the photomasks used for fabrication, (a) Layout of the full chip (1cm x 1cm), design using Klayout, (b) Layout of the 4 terminal device, (c) Layout of the 2 terminal device, (d) 3D view of the 4 terminal device, (e) 3D view of the 2 terminal device

- 10 → 11: Lift Off of Al_2O_3, and spin coating of photoresist
- 11 → 12: IBE to access bottom layer for better adhesion
- 12 → 13: Spin coating
- 13 → 14: Au deposition (100nm)
- 14 → 15: Lift-off of Au to isolate each device

4.2.1 Electron-Beam Lithography

First of all, the nanopillars used for STT devices need to be defined, in order to pattern the nanopillars down to a few tens of nanometers Electron-Beam Lithography (EBL) should be used, as it has a precision down to $10 \sim 20$ nm.

As the samples are covered in Platinum, which is hydrophobic, they need to be treated so the resist could adhere on the platinum. With this aim, we used plasma ashing to obtain a better adhesion with the negative EB resist. After the spin coating of the TGMR resist on the sample, it should be pre-baked to evaporate the solvent, which improves the adhesion and the resolution [41]. Therefore the initial 200 nm of EB resist might become slightly lower, allowing slightly reduced diameter for nanopillars.

The layout on Figure 26a presents nanopillar diameters ranging from 500 nm, 200 nm, 100 nm, 80 nm and 50 nm, this will allow to investigate the effect of diameter on STT

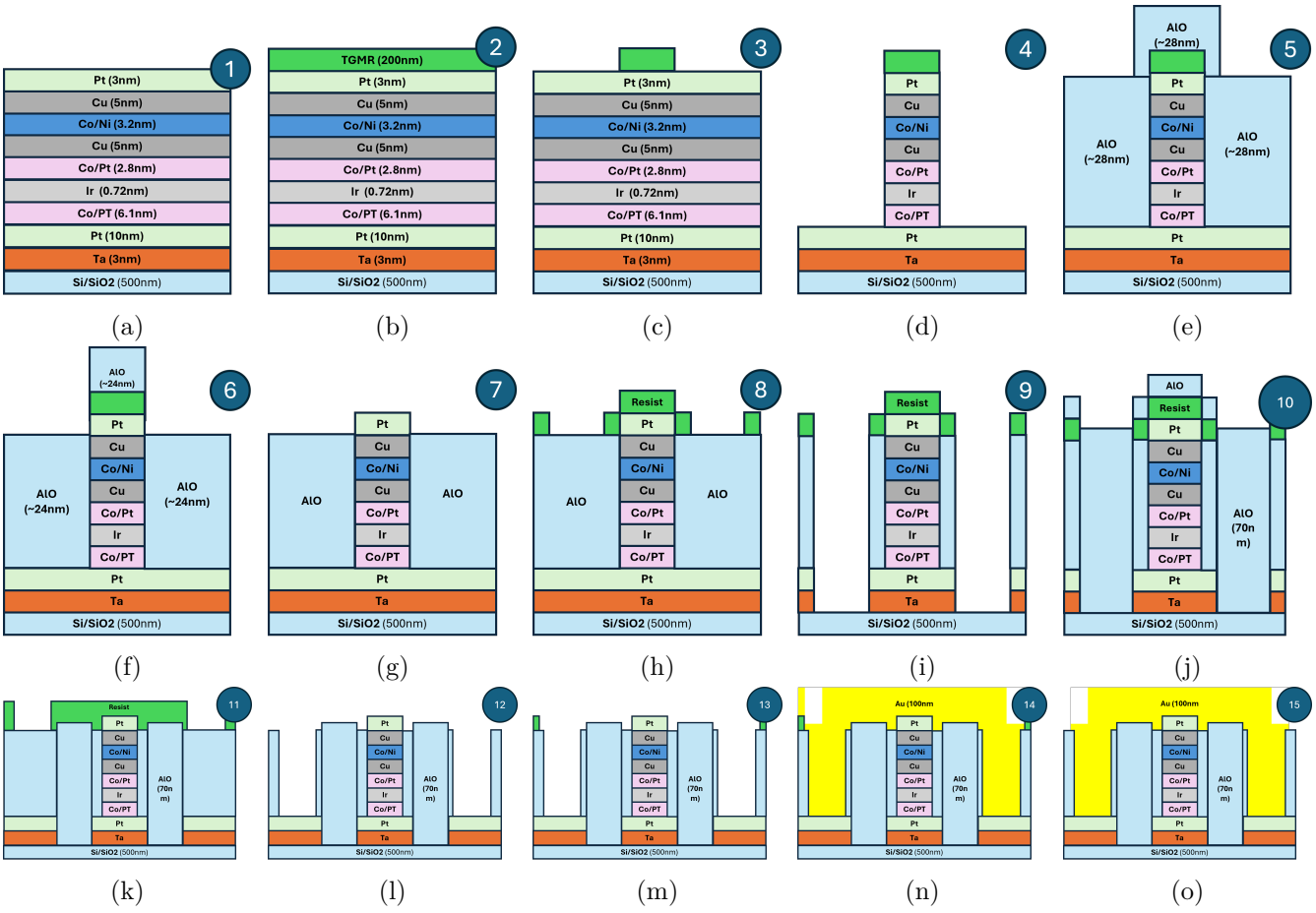


Figure 27: Schematic of the process flow for the fabrication of nanopillars

properties such as thermal stability.

However, in order to investigate these properties, the nanopillars should have the right diameter, to verify the correct fabrication of these pillars, a Scanning Electron Microscope (SEM) was used to verify the diameter of each pillar.

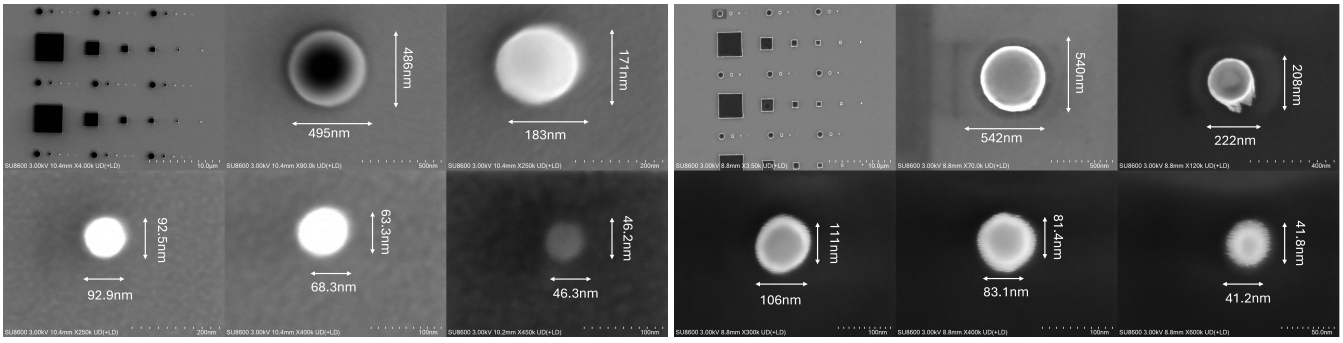


Figure 28: (a) SEM image of the nanopillars after TGMR development, fig. 27c, (b) SEM image of the nanopillars after Lift-Off of Al_2O_3, fig. 27g

Figure 28 shows the SEM images of the nanopillars. Figure 28a shows the nanopillars just after TGMR post-baking, development and stripping, it can be seen that the nanopillars could be well defined down to 50 nm.

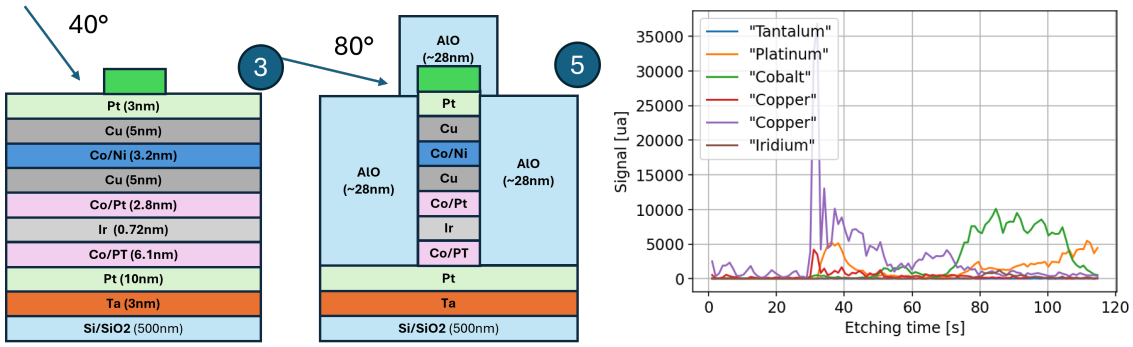
However, this observation is only realized on the TGMR resist on top of the sample (Figure 27c), it should be checked whether the nanopillars will still be defined after all the process.

In order to verify, that the nanopillars are still defined after etching and lift-off, we again used SEM, on Figure 28b we observe that the nanopillars are not affected much by the process, the process steps do not affect the definition of the pillars, even the 50 nm pillars are still defined.

4.2.2 Ion Beam Etching

In order to etch the thin film to obtain nanopillars, we used the Hakuto's Ion Beam Milling Etching system, it could etch material with a good uniformity, moreover many parameters of the etching tool can be tuned, such as the angle of incidence or the voltage.

Depending on the voltage intensity of the etching tool, we modify the etch rate of the material, an oxide might need higher voltage to have efficient etching. Regarding the angle of incidence of the ion beam, we define it according to the perpendicular of the sample, the angle might be tuned according to what needs to be etched (wall of the pillar, or electrode), but it also affects the redeposition of the etched material on the nanopillars. When etching the thin films, some of the etched material might redeposited on the nanopillar, this can be detrimental to the MR ratio, as there will be parallel resistance, lowering the total resistance of the device and the MR ratio.



(a) (b) (c)

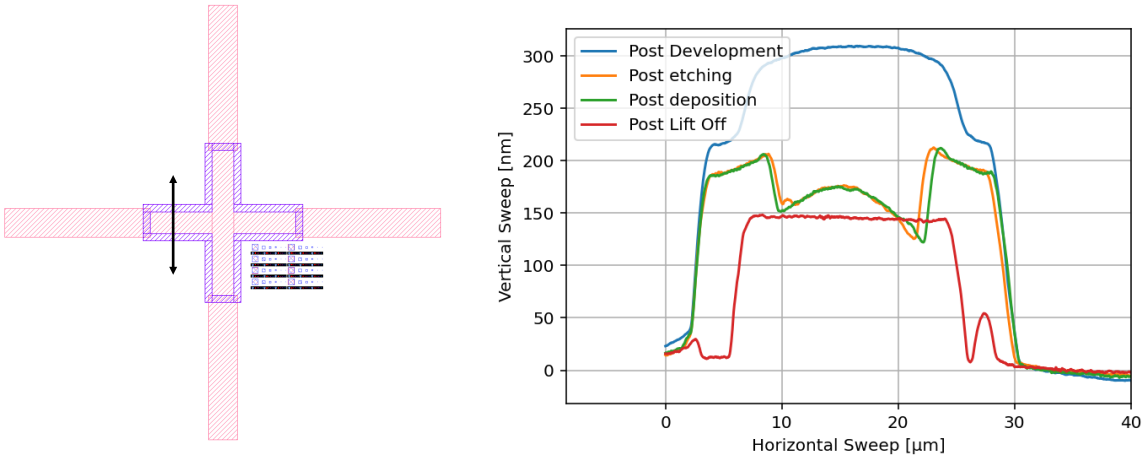
Figure 29: (a) represents the 40° etching angle used to etch the thin film down to Ta/Pt, (b) represents the 80° etching angle used to etch the side wall of the nanopillars, (c) Measured signal from the Hakuto etching tool, in order to monitor the etching of the nanopillars

Figure 29 represents the different angles used to etch the thin film. With the 40° angle is used to etch everything around the nanopillars down to the Ta/Pt. While the 80° angle is used to etch the side wall after aluminum oxide deposition, etching the side wall of the pillars will allow to lift off the TGMR resist and to have electrical access to the pillars later on.

Moreover, the Hakuto's etching tool has some measurement tools allowing to monitor the etching signal of every material in the thin film. For reference, we have completely etched a whole thin film, in order to have a rough time estimate for the etching of the thin film. Figure 29c is the measurement of the etching of the thin film, down to the Ta/Pt layer, the fall of the green cobalt signal indicates that we have etched everything down to the SAF, and the rising of the orange platinum signal indicates that we are starting to etch the bottom layer.

4.2.3 Lift Off

Finally, the lift-off is the last step to release the nanopillars, it uses a chemical solution which dissolves the TGMR resist, and therefore removes the aluminum oxide on top of the resist. Sometimes, the lift off of TGMR could be difficult, we could soften the resist by using plasma ashing. To verify the lift off of aluminum oxide, we could use optical microscopy and check the color before and after lift off. Another way is presented on Figure 30b, we use a profilometer to monitor the thickness. On the alignment mark (fig. 30a), there is a red layer which is gold covered only by Al_2O_3, the blue layer which is the thin film covered with TGMR and Al_2O_3.



(a) (b)

Figure 30: (a) Layout of the alignment mark, in red the gold mark, in blue the TGMR resist, the black arrow corresponds to the path of the profilometer tip, (b) Profilometer profile according to the fabrication step, post-development corresponds to step 3, post-etching corresponds to step 4, post-deposition corresponds to step 5 and post-lift-off corresponds to step 7

To monitor the lift off of Al_2O_3, on Figure 30b is the profile of the alignment mark after different process steps. From step 3, everything is covered in TGMR resist, it allows the confirmation that our TGMR is roughly 200 nm thick. Step 4 is after the etching of the thin film to define the nanopillar, on the center between 10 μm and 20 μm is the gold layer, and the sides correspond to the TGMR resist, the gold layer should be 150 nm, while the TGMR should be 200 nm, which is consistent with our measurement. Step 5 is the deposition of the Al_2O_3. And finally, step 7 shows the lift off of Al_2O_3, due to the difference between the gold

central plateau and the side, we could assume that the TGMR has been lifted off, as the gold layer is 150 nm thick compared to the thin film.

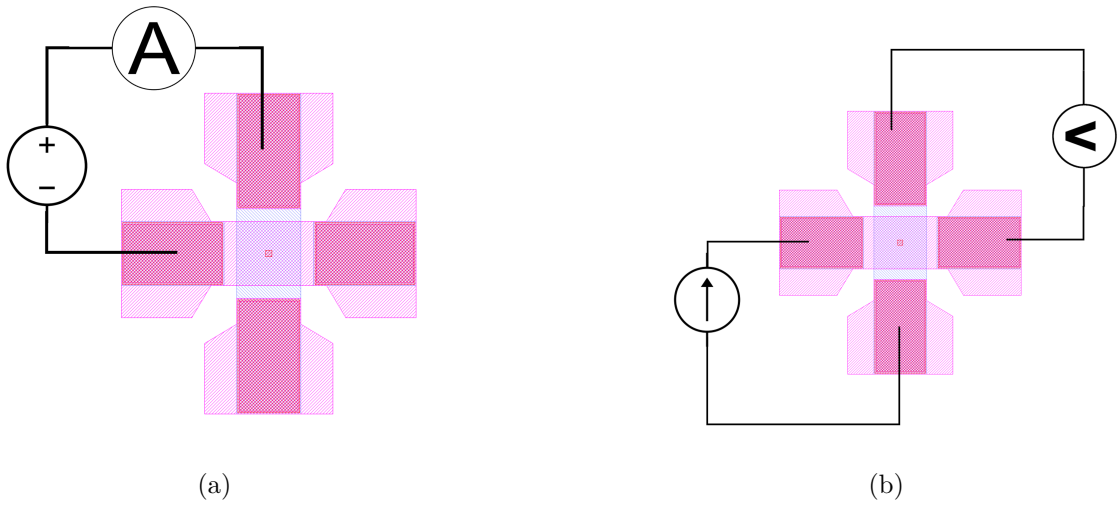
In this section, we explain the architecture and optimization of the spin valve, and demonstrate the AOS from P to AP state. In the last part, we define the fabrication process flow to manufacture devices, that will be characterized in the following section.

5 Characterization of STT devices:

The electrical characterization is necessary to determine the reliability of the fabrication process flow and the STT influence on the spin valve.

5.1 Presentation of the characterization setup

On our layout, there are two kinds of devices, a 2 terminal device, and a 4 terminal device. In the case of MTJ, the 4 terminal devices could be characterized with a 2 probes setup, as the TMR ratio will be high enough to be observable. While for spin valve, they must be characterized on a 4 probes setup, as their GMR ratio will be quite low. The two setups are described below.



(a) (b)

Figure 31: (a) presents the first setup using only 2 terminal, it applies a voltage and measures a current, (b) presents the second setup using 4 terminal, it applies a current and measures a voltage

Figure 31a, the 2 probes setup uses a sourcemeter Keithley 2400, it is used as a DC voltage source, and measures the current of the device. Moreover, it is also composed of an electromagnet to switch the magnetization, the range extends from -500 mT to 500 mT. In summary, we apply a voltage and measure the current.

Figure 31b, the 4 probes setup uses a Yokogawa GS200 DC Voltage and Current source, and a Nanovoltmeter Keithley 2182A to measure the voltage of the device. There is also an electromagnet, with a range from -500 mT to 500 mT. In summary, we apply a current and measure the voltage.

Both setups are manual, to move from one device to another, we need to manually move the wafer, and restart the characterization process.

5.2 Characterization of MgO based MTJ (H2 and H3)

H2 and **H3** are MTJ, they have been used to validate the process flow, and to obtain

some figure of merits of MTJ, from thermal stability, dispersion in TMR ratio or in R_{min}.

5.2.1 Thermal stability of STT device

The thermal stability is an important parameter of STT devices, as it is related to the stability and reliability of the device. However, to characterize the thermal stability of the device, statistical measurements are needed to characterize switching from AP to P, and from P to AP. The resistance as a function of the applied field (R-H loop) must be measured multiple times, to determine the switching probability [8, 42]:

$$P(H) = 1 - \exp\left(-\left|\frac{H_K}{2t_0 R_s}\right| \sqrt{\frac{\pi}{\Delta_0}} \text{erfc}\left(\left|\sqrt{\Delta_0}\left(1 - \frac{H}{H_K}\right)\right|\right)\right) \tag{27}$$

with H_K the anisotropy field in Oersted (10 Oe = 1 mT), t_0 the switching attempt time (1 ns), R_s the sweeping rate of the magnetic field (in our case 0.04 Oe/s), Δ_0 the thermal stability and erfc the error function. H_K and Δ_0 are used as fitting parameters for the function, that will be extracted from the fitting of the function.

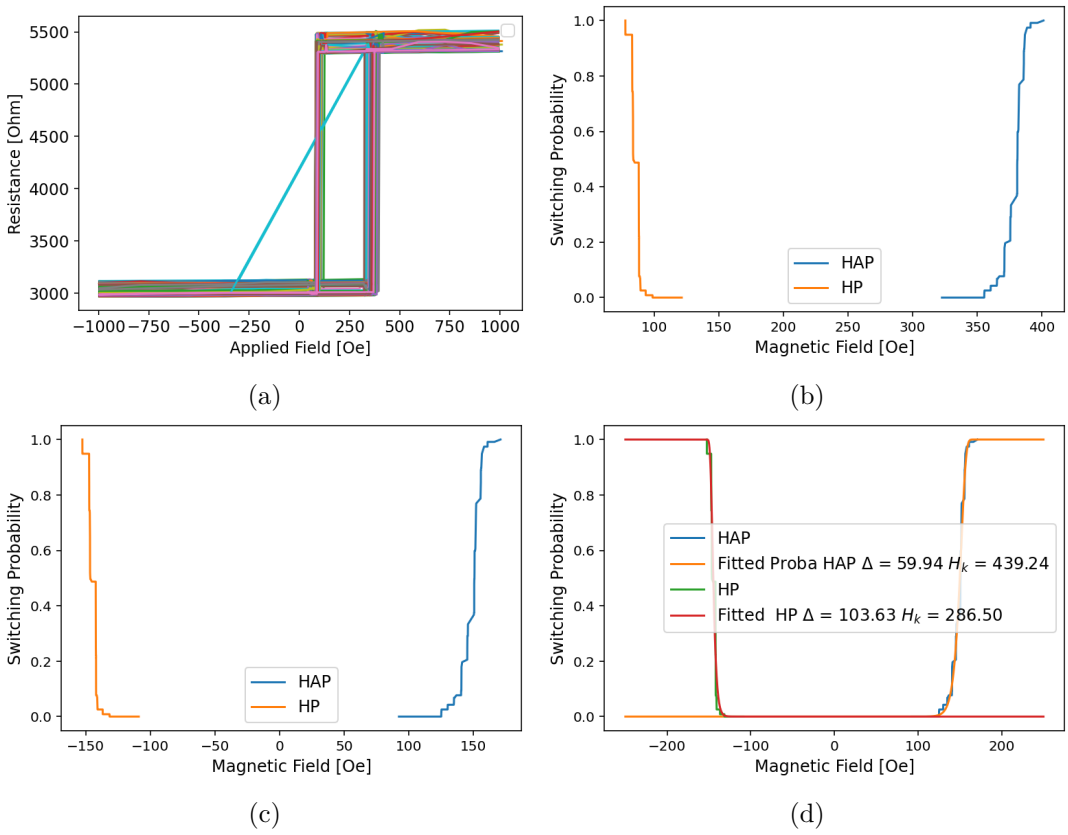


Figure 32: (a) Multiple hysteresis loop to obtain a distribution of the coercivity field, (b) Distribution of the coercivity field H_{AP} corresponds to the field to switch from P to AP, H_{P} corresponds to the field to switch from AP to P, (c) Distribution of the coercivity field centered at 0 Oe, (d) Distribution of the coercivity field and curve fitting to obtain thermal stability and anisotropy field

On Figure 32a, is the measured R-H loops for 120 loops, to allow the extraction of coercivity field for P to AP and AP to P. We could extract the coercivity field from P to AP (H_{AP}), and the coercivity from AP to P (H_{P}). The distribution of both coercivity fields can be plotted as a histogram, as on Figure 32b it could be observed that the coercivity fields are shifted around roughly 250 Oersted (25 mT), this stray field could be numerically compensated to center the coercivity fields around 0 Oe. That has been done on Figure 32c where the coercivity fields are centered around 0 Oe, this will be relevant to obtain a better fit for the thermal stability and anisotropy field. The fitting according to Equation 27 is represented on Figure 32d, this allows to extract the fitted parameter for $\Delta_{\mathrm{AP}} = 59.94$ and $\Delta_{\mathrm{P}} = 103.63$. We could express the thermal stability for P and AP according to the thermal stability of the device Δ_0 and the stray field H_s, adapted from [43]:

$$\Delta_{\mathrm{P}} = \Delta_0 \left(1 - \frac{H_s}{H_K}\right) \tag{28}$$

$$\Delta_{\mathrm{AP}} = \Delta_0 \left(1 + \frac{H_S}{H_K}\right) \tag{29}$$

$$\Delta_0 = \frac{\Delta_{\mathrm{P}} + \Delta_{\mathrm{AP}}}{2} \tag{30}$$

This experiment and statistical fitting give access to the thermal stability of the device, with $\Delta_0 = 81.7$ which corresponds to more than 10 years of data retention.

5.2.2 State Diagram

While in the previous subsection, statistical measurements on R-H loops have been realized, we could do similar statistics on the resistance as a function of voltage loops (R-V loop). Through the voltage application across the device, a current flows and generates a spin transfer torque, that will switch the magnetization state without any applied field. The R-I loop is measured multiple times, to allow the fitting of the following switching probability [8, 42]:

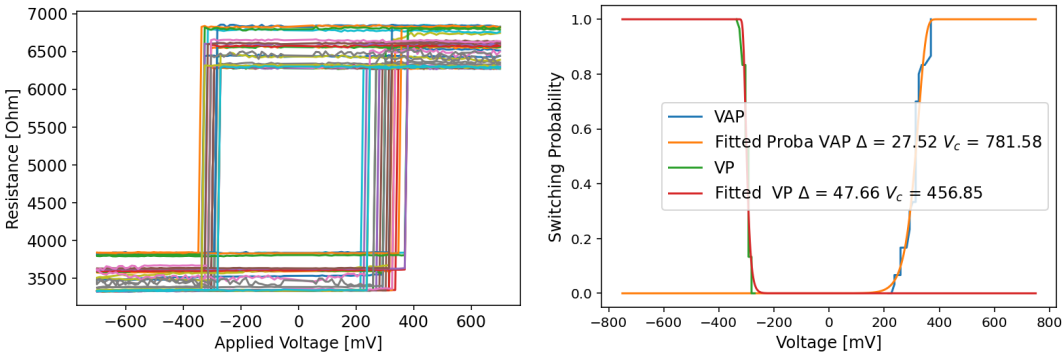
$$P(V) = 1 - \exp\left(\frac{t_P}{t_0}\exp\left(\Delta\left(1 - \frac{V}{V_{C0}}\right)\right)\right) \tag{31}$$

With t_p the voltage pulse length (10ms), V_{C0} the critical switching voltage.

Figure 33a is the repetition of 30 R-I loops to obtain statistic on the voltage distribution for switching, it should be noted that the stray field has been compensated by applying a magnetic field, so the distribution of voltage will be centered at 0 mV. The fitting of voltage distribution, on Figure 33b allows to extract the value for thermal stability and critical voltage.

By repeating the same experiment with different applied fields, we could obtain a kind of state diagram. We applied a certain magnetic field, we measured multiple R-I loops to obtain statistic on the thermal stability and critical voltage, that could be plotted on a state diagram. It should be noted, that usual state diagrams apply a constant voltage, and do a sweep in magnetic field. While we are applying a constant magnetic field, and doing a sweep in voltage. This is due to a long measurement time when measuring R-H loops.

The state diagram of Figure 34 has been plotted using the extracted thermal stability and critical voltage, for each applied field. There are three main areas on this state diagram, on



(a) (b)

Figure 33: (a) Multiple hysteresis curve as a function of applied voltage, (b) Distribution and curve fitting to obtain thermal stability and critical switching voltage

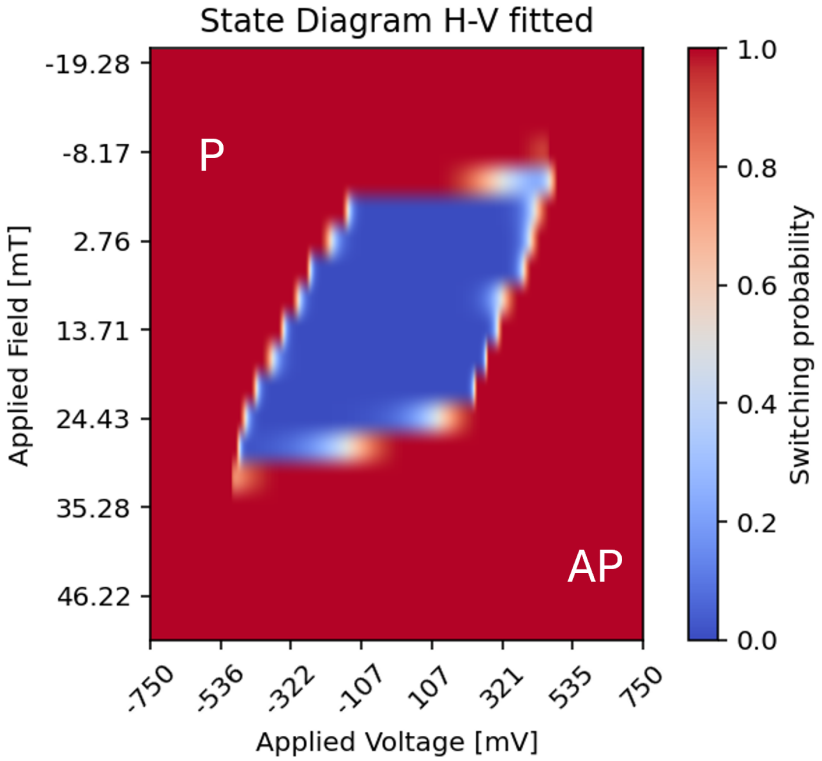
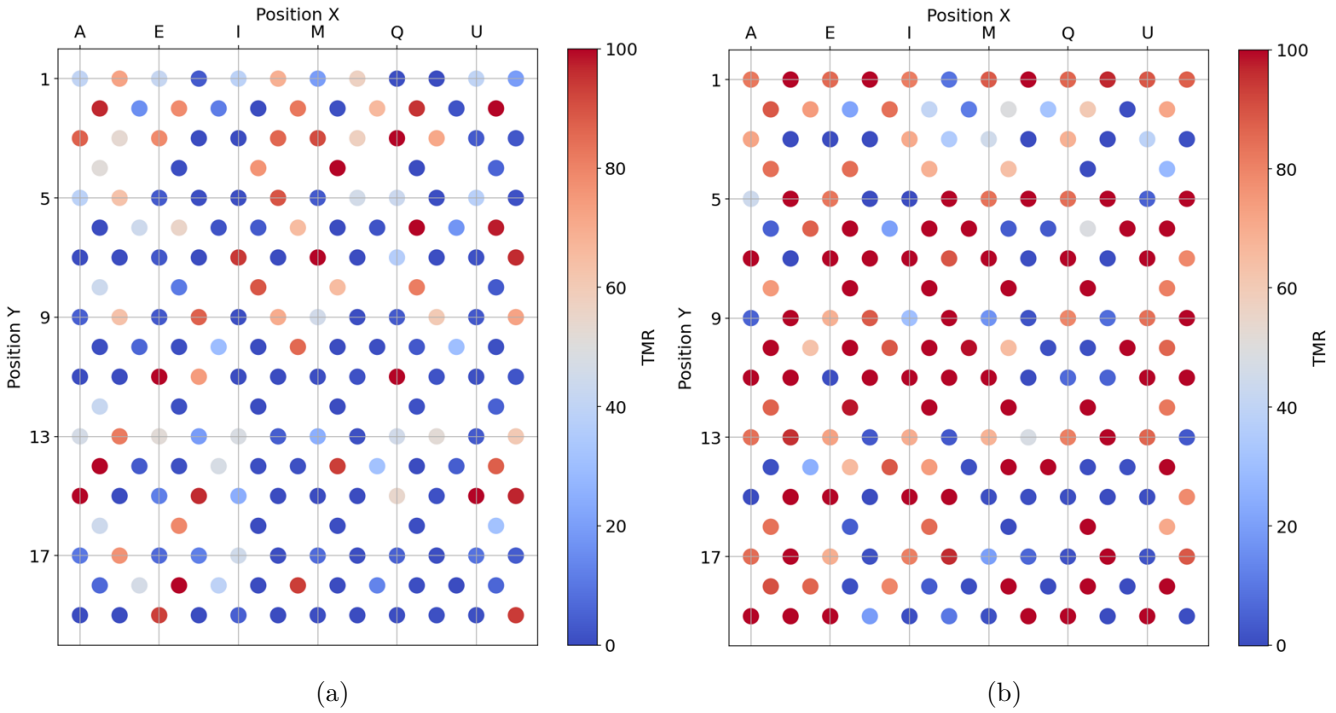


Figure 34: State Diagram of the device, in red corresponds the fact that the device is saturated in one state (AP or P), in blue corresponds the fact that the device stay in its previous state, at the intersection between the blue and red area is the probability of switching from P to AP, or AP to P

the bottom right the device will be saturated in AP state, on the top left the device will be saturated in P state. While in the middle of the graph, the device will remain in its previous state (either P or AP, according to where it came from) and could have a certain probability to switch to the opposite state.

5.3 Mapping of the wafers H2 and H3

Previously, the characterization has been focused on single device to extract its thermal stability, or critical voltage. While this section focuses on wafer characterization. Every device on the wafer have been characterized on the manual prober, to have a mapping of the wafer, and to obtain distribution of TMR and R_{min}. Figure 35 presents the TMR distribution for the sample **H2** and **H3**, it could be seen that **H3** has more devices with high TMR ratio. This could be explained by different etching time between the two samples, **H2** has been etched until the bottom Ta/Pt layer, while **H3** was slightly overetched after the Ta/Pt layer. We assume this lead to more Pt redeposition on **H2**'s nanopillars, leading to parallel resistance and a reduction in TMR.



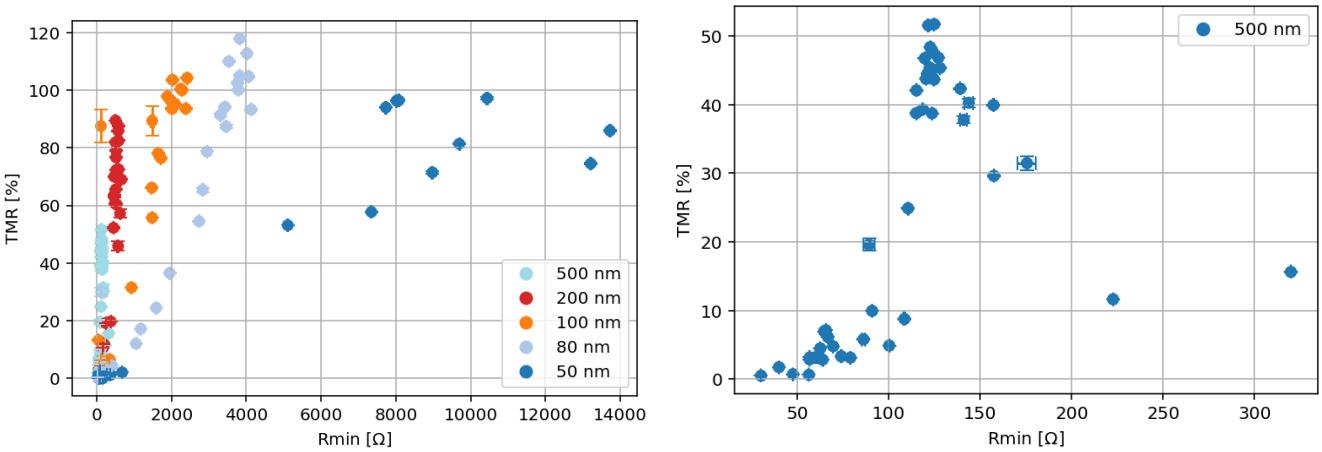
(a) (b)

Figure 35: (a) represents the mapping of the TMR in % for every device on **H2**, it has been characterized on the 2 probes setup, (b) represents the mapping of the TMR in % for every 4 terminal device on **H3**, it has been characterized on the 4 probes setup

Another distribution worth examining is the distribution of TMR according to $R_{\text{min}} \equiv R_{\text{P}}$, on Figure 36a it is shown for every device on the wafer. We observe an important dispersion in R_{min} for devices with a diameters of 80 nm and 50 nm, this might come from variations during fabrication. By looking only at 500 nm devices, on Figure 36b we could observe another interesting behavior, the TMR and R_{min} seem to have an optimum value around TMR = 50%, and $R_{\text{min}} = 130\ \Omega$. This distribution could be explained through serie and parallel resistance:

- Serie resistance: increases R_{min}, decreases TMR
- Parallel resistance: decreases R_{min}, increases TMR

During fabrication, we defined nanopillars of various diameters, however while fabricating



(a) (b)

Figure 36: (a) represents the distribution of TMR according to the minimum resistance, (b) represents the distribution of TMR according to minimum resistance but only for device with 500 nm diameter, most of the errorbar are inside the dot

various issues could occur such as oxidation of nanopillars leading to smaller diameters, to account for these unexpected events, we defined the electrical diameter:

$$D_{\text{elec}} = 2\sqrt{\frac{RA}{\pi R_{\text{P}}}} \tag{32}$$

with R_{P} the minimum resistance of the device, and RA the resistance-area product of the MTJ ($10\ \Omega \cdot \mu\text{m}^2$).

Finally, we could study the dispersion of thermal stability as a function of the electrical diameter of the device, as decreasing the diameter should induce a drop in thermal stability. From Figure 37, there is a plateau in thermal stability between roughly 100 nm and larger diameters. Below 80 nm, a clear drop in thermal stability occurs. The thermal stability drop in device F18 was not investigated in detail, however we expected this drop to result from fabrication issues.

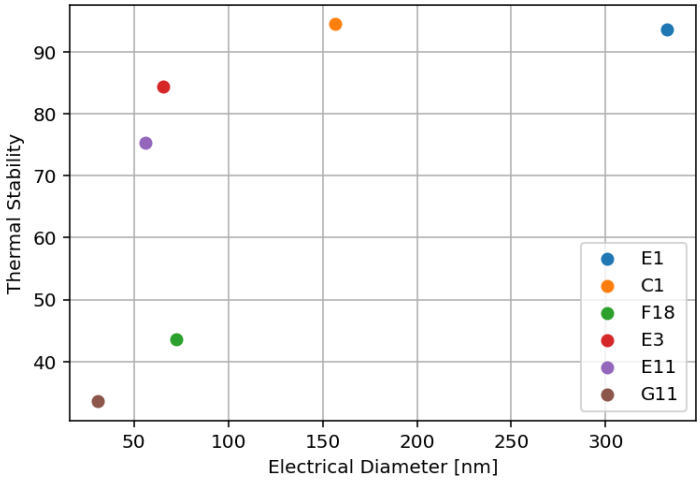


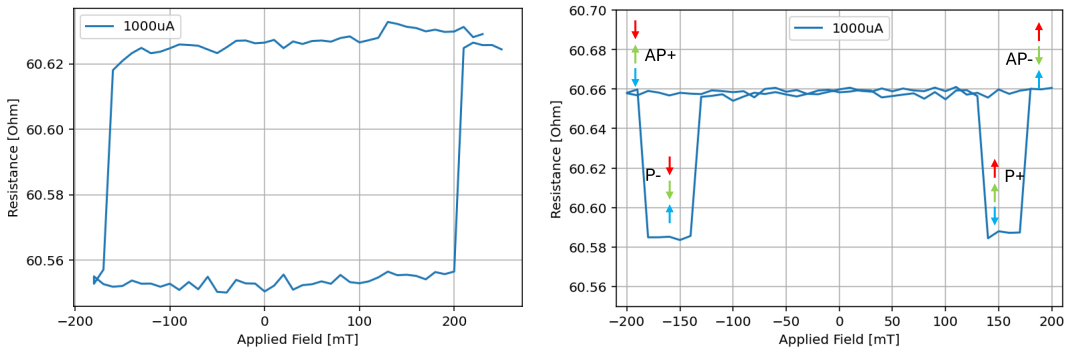
Figure 37: Evolution of thermal stability as a function of the electrical diameter for some devices, the labels correspond to the position of the devices on the wafer

5.4 Characterization of 1532 and 1534

The previous section confirmed that the process flow work to fabricate 4 terminal device, the same process flow will be used to manufacture GMR devices.

5.4.1 Field switching

First of all, the devices should be characterized through R-H measurements, to determine if the change in resistance is high enough to be observed on the 4 probes setup. Figure 38a shows the minor loop of the device, between -190 mT and 220 mT, a change in resistance of only 0.08 Ω and a GMR ratio of roughly 0.1% is observed.



(a) (b)

Figure 38: (a) shows the hysteresis loop on the minor loop of the device at 1000 uA, (b) shows the hysteresis loop on the major loop of the device at 1000 uA

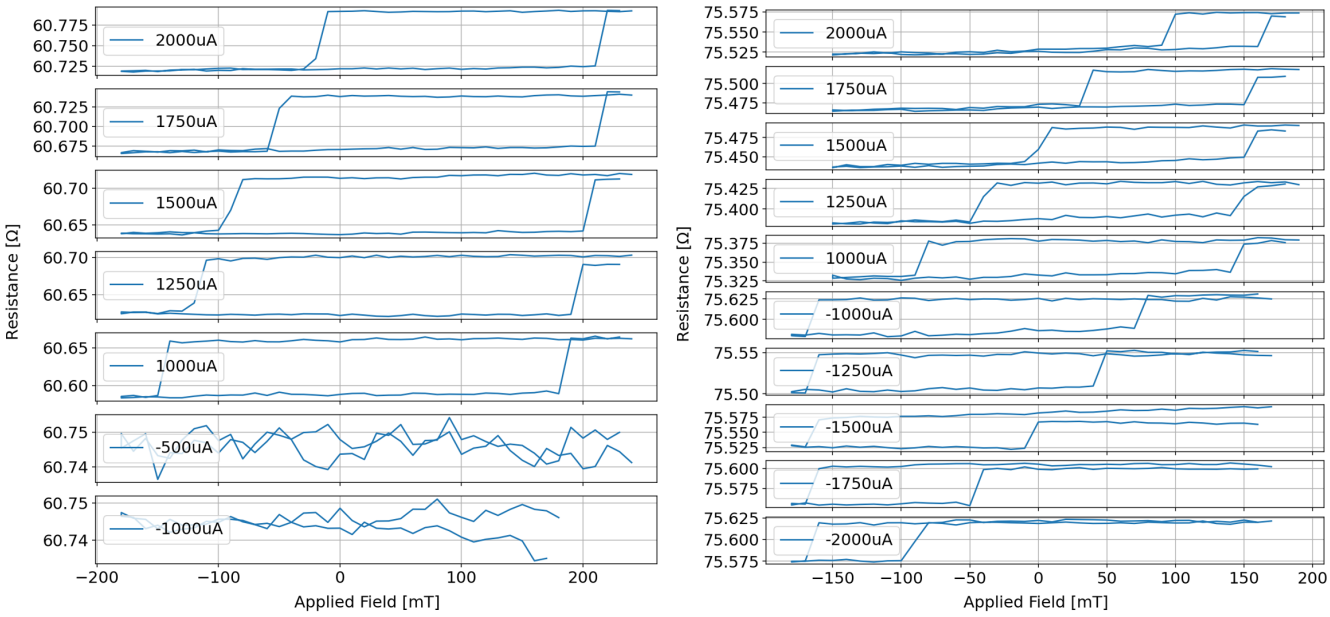
By applying larger magnetic field on Figure 38b, we could observe the switching of both the free and top reference layers. When starting from AP- state, reducing the field down to

−150 mT switches the free layer to go in P- state, however by further reducing the field below -190mT, it flip-flops the magnetization of the SAF switching to the AP+ state.

This proves that the fabrication process flow is also working for the spin valve, even though contact resistance and some process steps might be optimized to improve GMR ratio. Now, it should be investigated if there are STT effects in the spin valves.

5.4.2 State Diagram

In order to investigate STT effects in these spin valves, R-H loops have been measured at different applied currents. A constant current is applied across the device, and a magnetic field sweep is done to obtain R-H loop for different currents. On Figure 39, the state diagram for both sample are plotted, the X-axis corresponds to the sweep in magnetic field, the Y axis corresponds to the measured resistance and the labels in the subfigures are the applied current on the device. Both characterizations have been performed on the same device B2, which corresponds to a 100 nm nanopillars.



(a) (b)

Figure 39: (a) is the state diagram of the sample **1532**, (b) is the state diagram of the sample **1534**

From the state diagram of the device **1532** (fig. 39a), a modification of the coercivity field could be observed as the current increased, but only the coercivity field from AP to P is modified, the coercivity from P to AP is roughly constant around 200 mT. While positive currents show clear hysteresis loop and STT effect, negative currents produced unexpected results as the switching never happens from AP to P state, some tests were performed going from −400 mT to 400 mT and the switching could not be observed anymore. One might assume that the device burned in the meantime going from positive to negative current, however measuring the R-H loop again with positive current restored the hysteresis behavior. We could not explain this behavior of the device.

Nonetheless, for the state diagram of **1534** (fig. 39b), the STT effect could be observed both at positive and negative currents. Applying a positive current modifies the coercivity field to pass from AP to P, while the coercivity field from P to AP is kept constant around 150 mT. On the other hand, a negative voltage modifies the coercivity field from P to AP, and the coercivity field from AP to P is constant around −160 mT. The modification of the coercivity field could be linked to the STT efficiency in MTJ.

In MTJ, the STT efficiency can be expressed as the derivative of the coercivity field according to the derivative of the voltage [8]:

$$\frac{\partial H}{\partial V} = \frac{2e\eta}{\hbar\alpha RAM_s t} \tag{33}$$

For spin valve, the expression could be slightly different, however the STT efficiency is still related to the derivative of the field [44]:

$$\eta_{\text{eff}} \propto \frac{\partial H}{\partial V} \tag{34}$$

By plotting the evolution of the coercivity field according to the applied voltage, a linear fit allows to extract the STT efficiency of the two devices. For the sample **1534**, the STT efficiencies are $\eta_{\text{eff}}^{+} = -2061$ mT/V and $\eta_{\text{eff}}^{-} = 2168$ mT/V, for the positive and negative applied voltage. And for the sample **1532**, the STT efficiency for positive applied voltage is $\eta_{\text{eff}}^{+} = -1969$ mT/V. Between the two samples, the STT efficiency is quite similar, there is only a relative variation of 4.5%, the composition of the SAF layer has only a slight influence on STT efficiency. Moreover, for sample **1534** both STT efficiencies for positive and negative voltage are quite similar, with a relative variation of 5.2%, thus, the STT efficiency is nearly symmetric in this device and does not favor one switching state.

From these measurements, the process flow for the 4 terminal devices can be validated, furthermore, it is confirmed that the spin valve could have both STT and AOS mechanisms.

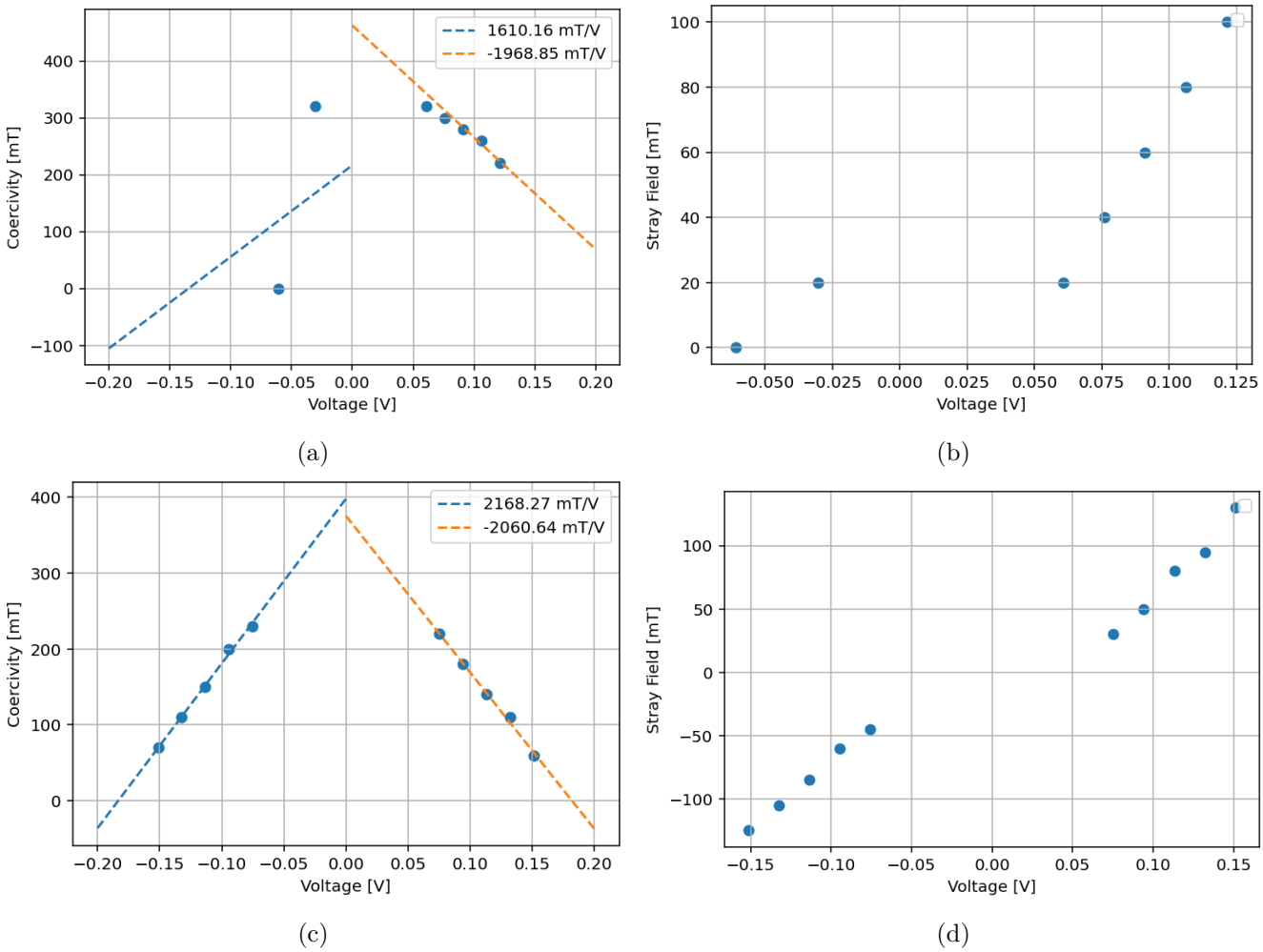


Figure 40: (a) represents the evolution of the coercivity field of the sample **1532** as a function of the applied voltage due to STT effect, (b) represents the evolution of the stray field of the sample **1532**, (c) represents the evolution of the coercivity field of the sample **1534** as a function of the applied voltage, (d) represents the evolution of the stray field according to voltage

6 Further Development of the AOS–STT Combination:

From the previous sections, we have demonstrated that our spin valve devices could exhibit at the same time AOS and STT behavior, which opens interesting opportunities for the combination of STT and AOS on the same device architecture. This may allow more energy efficient device at the picosecond timescale, even though there is still a need to investigate the effect of current and light-induced magnetization reversal at the same time.

In this thesis, we demonstrated that the spin valve studied has both STT and AOS behavior, however the STT behavior has been studied on fabricated devices, and AOS has been studied on thin films, so we should verify AOS on manufactured devices. That will required some adaptation for the fabrication process that are presented in this section.

6.1 Modification of the top electrode

During the fabrication in Fukami-Kanai laboratory cleanroom, we deposited a thick gold electrode over 100nm thick, so due to light absorption by the gold layer, we could not access the nanopillar for AOS. However, to verify AOS on nanofabricated devices, they should be accessible by laser irradiation.

One approach to access the nanopillars is the reduction of the gold thickness for the top electrode, Figure 41 as the gold becomes thinner, more light can be transmitted through the gold layer. The investigation of gold thickness was carried during this thesis, multiple thicknesses of Cr(5nm)/Au(Xnm) have been deposited on Glass substrate. Their electrical resistivity could be measured with a 4 probe measurements. Regarding the optical transmission, we have the reference optical transmission of the glass substrate, and through the measurement of the transmitted power of the gold thin film, we obtain the optical transmission of gold according to this thickness.

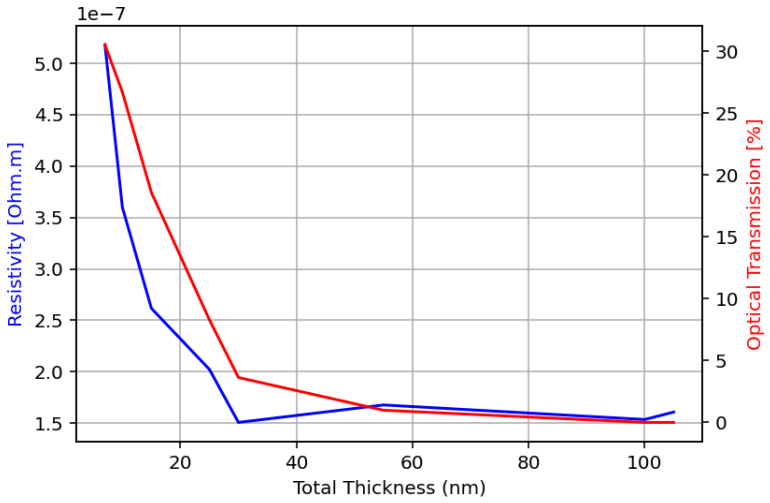
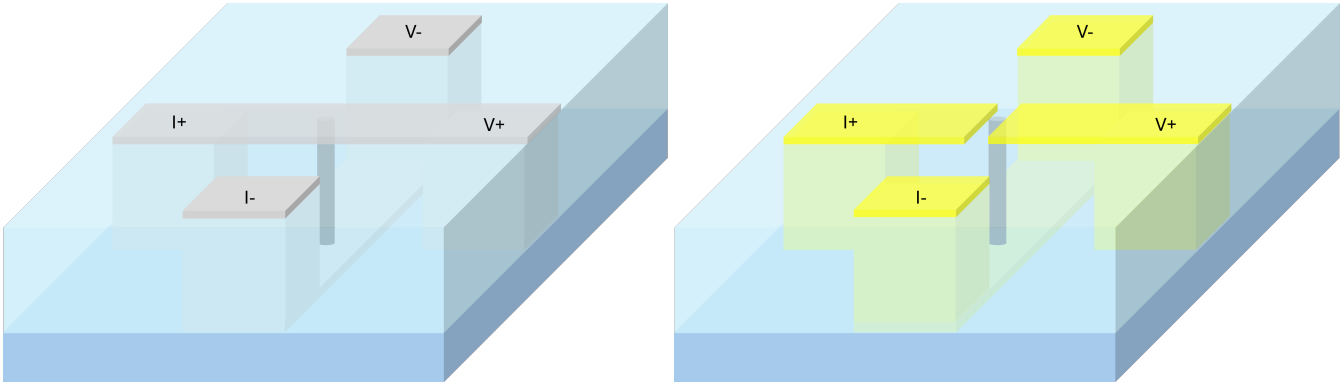


Figure 41: Evolution of the sheet resistance (in blue) and the optical transmission (in red) as a function of the thickness of the Cr(5nm)/Au(Xnm) thin film

This study allows to confirm, that gold could become fairly transparent below 30 nm, however while the optical transmission increases for thinner gold, the resistivity also increases. As our GMR ratio is quite low, and the resistance of the device is roughly tens to hundreds of Ohms, the increase in resistivity with thinner gold, might make the GMR impossible to measure due to high contact resistance.

Due to the influence of contact resistance, it seems unlikely to obtain efficient STT and AOS by lowering the top electrode thickness. In order to combine both STT and AOS, some new structures might be investigated. On Figure 42, other materials and architectures are described.

One way to obtain low resistance and optical transmission is to use an ITO thin film, such as Figure 42a, it has already been used for voltage assisted AOS [46]. Another way, would be to separate the top electrode into 2 electrodes Figure 42b, in order to have optical access in the middle between the two top electrodes, moreover it might improve GMR ratio at the same time [45].



(a) (b)

Figure 42: 3D view of the potential next electrodes, (a) an ITO electrode to let light flow through the electrode, (b) a separated gold top electrode to let light flow in the center

6.2 Modify the Copper interlayer

In order to improve the GMR ratio, an optimization of the free layer will be necessary to have more than 0.1 %. Another reason for this low GMR, might be redeposition during IBE, that causes parallel resistance and so a drop in GMR. Moreover, for AOS there is also an influence from the spacer thickness of the spin valve. According to the spacer layer, the threshold fluence to go from P to AP configuration, or from AP to P, could be reduced [30].

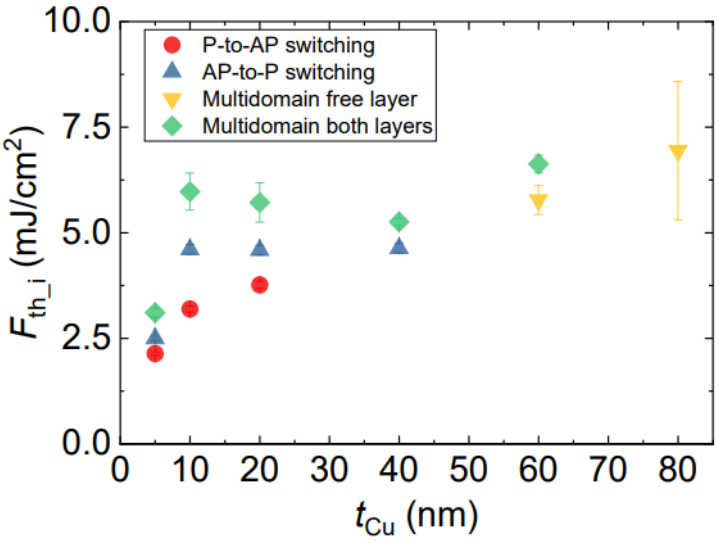


Figure 43

Figure 44: Influence of Copper thickness on threshold fluence for switching in ferromagnetic spin valve, image taken from [30]

7 Conclusion:

The combination of STT and AOS might lead to really interesting opportunities in the field of ultra-fast magnetization reversal and energy efficiency. It allows for the combination of magnetic, photonic and electronic functionnalities.

Regarding the characterization of AOS and STT in the spin valve sample, the two mechanisms have been characterized independently, AOS on thin films, and STT on manufactured devices. However, to combine AOS and STT, there is still a need for characterization of both at the same time.

From the combination of STT and AOS, we could achieve sub-picosecond writing time, as well as better energy efficiency for magnetization reversal [38]. Moreover, it would provide greater tunability from a design point of view, the tunability would extend across optical parameters (such as laser fluence, laser pulse width...), electrical parameters (current amplitude, current pulse width...) and magnetic parameters (magnetoresistance, energy barrier, anisotropy...). This could allow us to use the advantage from each field, even though there will obviously be trade-offs necessary.

This thesis opened the investigation of STT-AOS combination on the studied GMR structure, even though some challenges are ahead with the modification of the electrodes and AOS for AP to P. The first proof of concept for STT-AOS in GMR device is demonstrated.

This might lead to the development of hybrid photonic and spintronic devices, the laser beam would be used for ultra-fast and energy efficient switching, while the spin valve would be used as a non-volatile memory. One limitation of using a spin valve, would be the low readability of the resistance as the GMR is quite small, however moving toward a MTJ architecture might allow better readability at the cost of a trade-off with AOS performance

8 Bibliography:

References

[1] Bhushan, B. *Historical evolution of magnetic data storage devices and related conferences.* Microsyst Technol 24, 4423–4436 (2018) :https://doi.org/10.1007/s00542-018-4133-6

[2] Coey J.M.D. *Magnetism and Magnetic Materials.* Cambridge University Press, June 2012 :https://doi.org/10.1017/CBO9780511845000

[3] Sharma, Ravi and Mannava, Purna and Wingreen, Stephen. *Reverse-Engineering the Design Rules for Cloud-Based Big Data Platforms.* Cloud Computing and Data Science, 2022 :https://doi.org/10.37256/ccds.3220221213

[4] *Emerging Non-Volatile Memory,* Yole Group, 2017 :https://fr.slideshare.net/slideshow/emerging-nonvolatile-memory-2017-report-by-yole-developpement/77177130#4

[5] *2024 United States Data Center Energy Usage Report,* Berkeley Lab, Energy Analysis and environmental impacts division, 2024 :https://escholarship.org/uc/item/32d6m0d1

[6] M. Strungaru et al., *All-Optical Switching: A Path to Recording Technology Beyond HAMR.* IEEE Transactions on Magnetics, vol. 61, no. 4, pp. 1-9, April 2025 :https://doi.org/10.1109/TMAG.2025.3530769

[7] Nuno Caçoilo, Shunsuke Fukami, Olivier Fruchart, Ioan-Lucian Prejbeanu *Towards Ultra Scalability of Non-Volatile Magnetic Tunnel Junctions with a 3D Storage Layer.* arXiv:2608.20850 [cond-mat.mes-hall] :https://doi.org/10.48550/arXiv.2608.20850

[8] Nuno Caçoilo, *Fundamentals of ultra scaled 3D magnetic tunnel junctions and integration routes for high density memory arrays.* Université Grenoble Alpes 2020-2023, :https://theses.hal.science/tel-04417023v1

[9] Bruno, P., Renard, J.P., *Magnetic surface anisotropy of transition metal ultrathin films.* Appl. Phys. A 49, 499–506 (1989) :https://doi.org/10.1007/BF00617016

[10] *Curie Temperature,* Wikipedia, August 20th 2026 :https://en.wikipedia.org/wiki/Curie_temperature

[11] *Ferromagnetism,* Wikipedia, August 20th 2026 :https://en.wikipedia.org/wiki/Ferromagnetism

[12] E.C. Stoner, F.R.S. and E.P. Wohlfarth *A Mechanism of Magnetic Hysteresis in Heterogeneous Alloys* Physics Department, University of Leeds, 24 July 1947

[13] Alex Aubert and Konstantin Skokov and Oliver Gutfleisch, *Determining the anisotropy field of permanent magnets: A comparison of current methodologies.* Journal of Magnetism and Magnetic Materials, Vol 643, 15 November 2025 :https://doi.org/10.1016/j.jmmm.2025.173566

[14] *Antiferromagnetism,* Wikipedia, August 20th 2026 :https://fr.wikipedia.org/wiki/Antiferromagnetisme

[15] Duine, R.A., Lee, KJ., Parkin, S.S.P. et al. *Synthetic antiferromagnetic spintronics.* Nature Phys 14, 217–219 (2018) :https://doi.org/10.1038/s41567-018-0050-y

[16] *Faraday Effect* Wikipedia, August 26th 2026 :https://en.wikipedia.org/wiki/Faraday_effect

[17] Christian Heiliger, Peter Zahn, Ingrid Mertig. *Microscopic origin of magnetoresistance.* Materials Today, volume 9, 2006 :https://doi.org/10.1016/S1369-7021(06)71694-7

[18] Binasch, G. and Grünberg, P. and Saurenbach, F. and Zinn, W. *Enhanced magnetoresistance in layered magnetic structures with antiferromagnetic interlayer exchange.* Phys. Rev. B, volume 39, issue 7, 1989 :https://doi.org/10.1103/PhysRevB.39.4828

[19] *Spin valve,* Wikipedia, August 26th 2026 :https://en.wikipedia.org/wiki/Spin_valve

[20] *Giant magnetoresistance* Wikipedia, August 16th 2026 :https://en.wikipedia.org/wiki/Giant_magnetoresistance

[21] Schuhl, Alain and Lacour, Daniel, *Spin dependent transport: GMR and TMR.* Comptes Rendus Physique - C R PHYS, Volume 6, 2005 :https://doi.org/10.1016/j.crhy.2005.10.010

[22] Fert, A. and Campbell, I. A, *Two-Current Conduction in Nickel.* Phys. Rev. Lett., volume 21, issue 16, 1968 :https://doi.org/10.1103/PhysRevLett.21.1190

[23] M Julliere, *Tunneling between ferromagnetic films.* Physics Letters A, volume 54, 1975 :https://doi.org/10.1016/0375-9601(75)90174-7

[24] J.C. Slonczewski, *Current-driven excitation of magnetic multilayers.* Journal of Magnetism and Magnetic Materials, volume 159, 1996 :https://doi.org/10.1016/0304-8853(96)00062-5

[25] Samal, Dibyajyoti, Kumar, Anil. *Giant magnetoresistance: Nobel Prize in Physics 2007.* Resonance, August 2008 :https://doi.org/10.1007/s12045-008-0015-z

[26] Parkin, S. S. P. and More, N. and Roche, K. P. *Oscillations in exchange coupling and magnetoresistance in metallic superlattice structures: Co/Ru, Co/Cr, and Fe/Cr.* Phys. Rev. Lett. 64, 2304 – Published 7 May, 1990 :https://doi.org/10.1103/PhysRevLett.64.2304

[27] D. Apalkov, B. Dieny and J. M. Slaughter, *Magnetoresistive Random Access Memory.* Proceedings of the IEEE, vol. 104, no. 10, pp. 1796-1830, Oct. 2016 :https://doi.org/10.1109/JPROC.2016.2590142

[28] Radu, I., Vahaplar, K., Stamm, C. et al. *Transient ferromagnetic-like state mediating ultrafast reversal of antiferromagnetically coupled spins.* Nature 472, 205–208 (2011) :https://doi.org/10.1038/nature09901

[29] Fukami, S., Anekawa, T., Zhang, C. et al. *A spin–orbit torque switching scheme with collinear magnetic easy axis and current configuration.* Nature Nanotech 11, 621–625 (2016) :https://doi.org/10.1038/nnano.2016.29

[30] Igarashi, J., Zhang, W., Remy, Q. et al. *Optically induced ultrafast magnetization switching in ferromagnetic spin valves.* Nat. Mater. 22, 725–730 (2023) :https://doi.org/10.1038/s41563-023-01499-z

[31] Singh, Harjinder and Anadón, Alberto and Igarashi, Junta and Remy, Quentin and Mangin, Stéphane and Hehn, Michel and Gorchon, Jon and Malinowski, Gregory *Ultrafast Spin Accumulations Drive Magnetization Reversal in Multilayers* Phys. Rev. Lett. 136, 2026 :https://doi.org/10.1103/z2sz-2tdz

[32] Yooleemi Shin, Ji-Wan Kim *Fundamental basics on measurement instruments and techniques for ultrafast magnetism dynamics.* Current Applied Physics, Volume 61, 2024, Pages 34-46, ISSN 1567-1739, :https://doi.org/10.1016/j.cap.2024.01.008

[33] A Olivier, L Avilés-Félix, et al. *Indium Tin Oxide optical access for magnetic tunnel junctions in hybrid spintronic–photonic circuits.* Nanotechnology, Volume 31, Number 42 (2020) :https://doi.org/10.1088/1361-6528/ab9c56

[34] K. Waseda, R. Doi, B. Purnama, S. Yoshimura, Y. Nozaki and K. Matsuyama, *Heat-Assisted Magnetization Reversal Using Pulsed Laser Irradiation in Patterned Magnetic Thin Film With Perpendicular Anisotropy,* IEEE Transactions on Magnetics, vol. 44, no. 11, pp. 2483-2486, Nov. 2008 :https://doi.org/10.1109/TMAG.2008.2003068

[35] Quentin Remy, *Ultrafast spin dynamics and transport in magnetic metallic heterostructures,* Université de Lorraine, 2021 :https://hal.univ-lorraine.fr/tel-03560783v1

[36] Remy, Q., Hohlfeld, J., Vergès, M. et al. *Accelerating ultrafast magnetization reversal by non-local spin transfer.* Nat Commun 14, 445 (2023) :https://doi.org/10.1038/s41467-023-36164-1

[37] Yann Le Guen, *All-optical helicity-dependent switching in magnetoplasmonic structures.* Université de Lorraine, 2025 :https://theses.hal.science/tel-05619627v1

[38] W. Zhang, M. Hehn, Y. Peng, et al. *Deterministic Ultra-Fast All-Optical Switching in Gd free Ferrimagnetic Spin Valve Structures.* Adv. Funct. Mater. 35, no. 52 (2025) :https://doi.org/10.1002/adfm.202505423

[39] Funatsu, T., Kanai, S., Ieda, J. et al. *Local bifurcation with spin-transfer torque in superparamagnetic tunnel junctions.* Nat Commun 13, 4079 (2022) :https://doi.org/10.1038/s41467-022-31788-1

[40] Amara, S., Al Saidi, W., Al Ma'Mari, F. et al. *Enhanced tunneling magnetoresistance and thermal stability in magnetic tunnel junctions with multiple CoFeB/Ta interfaces.* Sci Rep 16, 22131 (2026) :https://doi.org/10.1038/s41598-026-53080-8

[41] H. Kirchauer, *Photolithography Simulation,* PhD Dissertation, TU Wien 1998 :https://www.iue.tuwien.ac.at/phd/kirchauer/node31.html

[42] L. Tillie et al. *Data Retention Extraction Methodology for perpendicular STT-MRAM.* 2016 IEEE International Electron Devices Meeting (IEDM), San Francisco, CA, USA, 2016 :https://doi.org/10.1109/IEDM.2016.7838492

[43] Funatsu, T., Kanai, S., Ieda, J. et al. *Local bifurcation with spin-transfer torque in superparamagnetic tunnel junctions.* Nat Commun 13, 4079 (2022) :https://doi.org/10.1038/s41467-022-31788-1

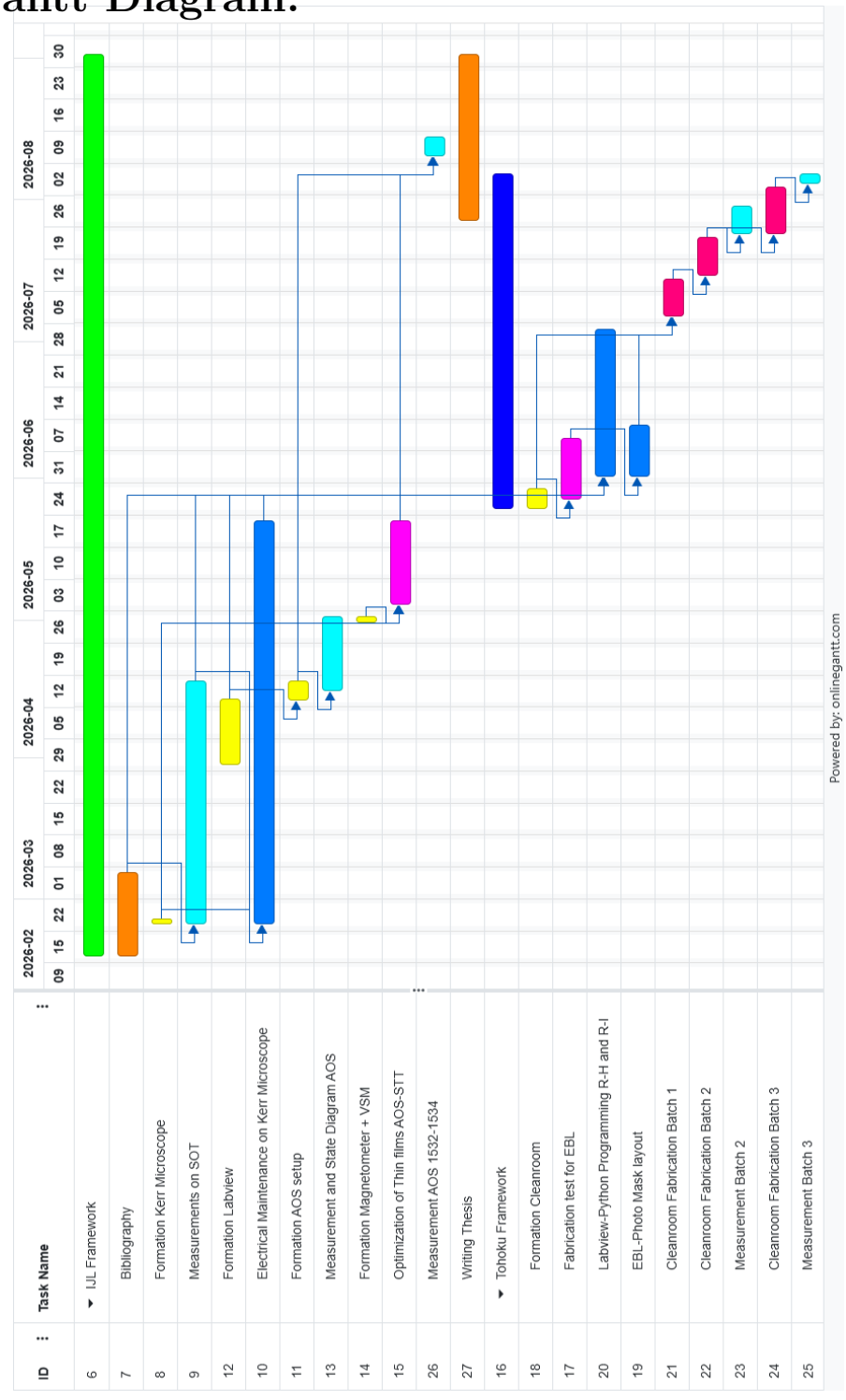
[44] M. C. Hickey, D.-T. Ngo, S. Lepadatu, D. Atkinson, D. McGrouther, S. McVitie, C. H. Marrows, *Spin-transfer torque efficiency measured using a Permalloy nanobridge.* Appl. Phys. Lett. 97, 202505 (2010) :https://doi.org/10.1063/1.3520144

[45] Lagarrigue, Aurélien and Sanchez-Manzano, David and al. *Bipolar spin-valve effect in complex-oxide superconductor/half-metallic ferromagnet junctions.* Phys. Rev. Mater., volume 10, issue 1, 2026 :https://doi.org/10.1103/gr8k-15wt

[46] Quoc Trung Trinh, Jun-Xiao Lin, Boonthum Kunyangyuen, and al. *Voltage-assisted all-optical switching in magnetic tunnel junctions based on Tb/Co multilayers.* APL Mater. 1 June 2026 :https://doi.org/10.1063/5.0331782

[47] A. Hütten and S. Mrozek and S. Heitmann and T. Hempel and H. Brückl and G. Reiss, *Evolution of the GMR-effect amplitude in copper/permalloy-multilayered thin films.* Acta Materialia, Volume 47, Issues 15–16, November 1999 :https://doi.org/10.1016/S1359-6454(99)00283-9

A Gantt Diagram:



B Summary sheet:

Sujet stage 5 à 6 Mois – Master 2

Étude expérimentale de la dynamique d'aimantation induite par la lumière dans des nanostructures magnéto-plasmoniques

Contexte :
Ce stage s'inscrit dans le cadre d'une collaboration internationale entre l'Institut Jean Lamour (Université de Lorraine, Nancy, France) et le groupe du Prof. Shigemi Mizukami à Tohoku University (Sendai, Japon), reconnu mondialement pour ses travaux sur la spintronique, la dynamique ultra-rapide du magnétisme et les dispositifs magnétiques avancés.

Face à la crise climatique et à la consommation croissante d'énergie des technologies numériques, la recherche de solutions électroniques plus sobres est devenue un enjeu majeur. Les technologies spintroniques et photo-spintronique offrent des perspectives prometteuses pour réduire l'impact énergétique de l'électronique en exploitant les propriétés quantiques du spin et de la lumière plutôt que le déplacement de charges. Comprendre et maîtriser ces phénomènes à l'échelle nanométrique est essentiel pour concevoir les dispositifs de mémoire et de traitement de l'information du futur, alliant vitesse, efficacité énergétique et durabilité**.**

L'objectif général est d'explorer les phénomènes de conversion lumière–spin et de contrôle optique de l'aimantationdans des nanostructures hybrides combinant métaux ferromagnétiques et matériaux plasmoniques (Au, Pt, CoPt, etc.). Ces recherches contribuent au développement de nouvelles générations de dispositifs photo-spintronique et ultra-rapides pour les mémoires optiques et les sources térahertz.

Objectifs du stage :
Le stage vise à mettre en œuvre et à exploiter des expériences permettant d'étudier la réponse magnétique et optique de couches minces et de nanostructures magnéto-plasmoniques soumises à des impulsions laser femtosecondes.

L'élève participera aux activités suivantes :

- Préparation d'échantillons : dépôt de couches minces (sputtering, évaporation), lithographie électronique ou optique pour la fabrication de nanostructures plasmoniques.
- Caractérisations structurales et magnétiques :
  - Microscopie MEB et AFM pour la morphologie,
  - Mesures magnétiques statiques (VSM, MOKE station),
  - Spectroscopie optique et plasmonique (réflectométrie, spectres de transmission).

- Expériences de dynamique ultra-rapide :
  Participation à des mesures de dynamique d'aimantation par effet Kerr optique résolu en temps (TR-MOKE).

Une partie du stage pourra être réalisée à **Tohoku University**, au sein du laboratoire du Prof. Mizukami, pour la mise en œuvre d'expériences spécifiques (croissance d'échantillons CoPt, mesures optiques femtosecondes, etc.).

Livrables attendus :

- Rapport détaillé sur la préparation et la caractérisation des échantillons.
- Résultats expérimentaux de dynamique d'aimantation (courbes TR-MOKE).
- Discussion des effets plasmoniques et comparaison avec les modèles théoriques.

Compétences requises :

- Intérêt pour la physique des matériaux et le magnétisme.
- Connaissances de base en optique et en techniques expérimentales sous vide.
- Rigueur expérimentale, autonomie et goût pour le travail en équipe internationale.
- Bon niveau d'anglais (communication avec le laboratoire japonais).

Encadrants :

- Prof. Stéphane Mangin – Institut Jean Lamour, Université de Lorraine (Nancy, France)
  stephane.mangin@univ-lorraine.fr
- Prof. Shigemi Mizukami – Tohoku University (Sendai, Japon)

UNIVERSITÉ DE LORRAINE

東北大学
TOHOKU UNIVERSITY

Institut Jean Lamour
2 allée André Guinier BP 50840 Campus Artem
54011 Nancy Cedex
www.ijl.univ-lorraine.fr

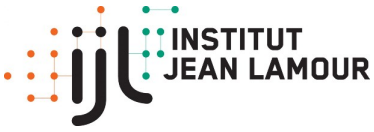
Id: Julien DECHELETTE

Master degree: MNIS (Micro and Nanotechnologies for Integrated Systems)

Academic Year: 2026

Internship Title: Experimental study of light-induced magnetization dynamics in magneto-plasmonic nanostructures - Etude expérimentale de la dynamique d'aimantation induite par la lumière dans des nanostructures magnéto-plasmonique

Hosting institution: Institut Jean Lamour, Université de Lorraine,
2 allée André Guinier, BP 50840, 54011 Nancy CEDEX



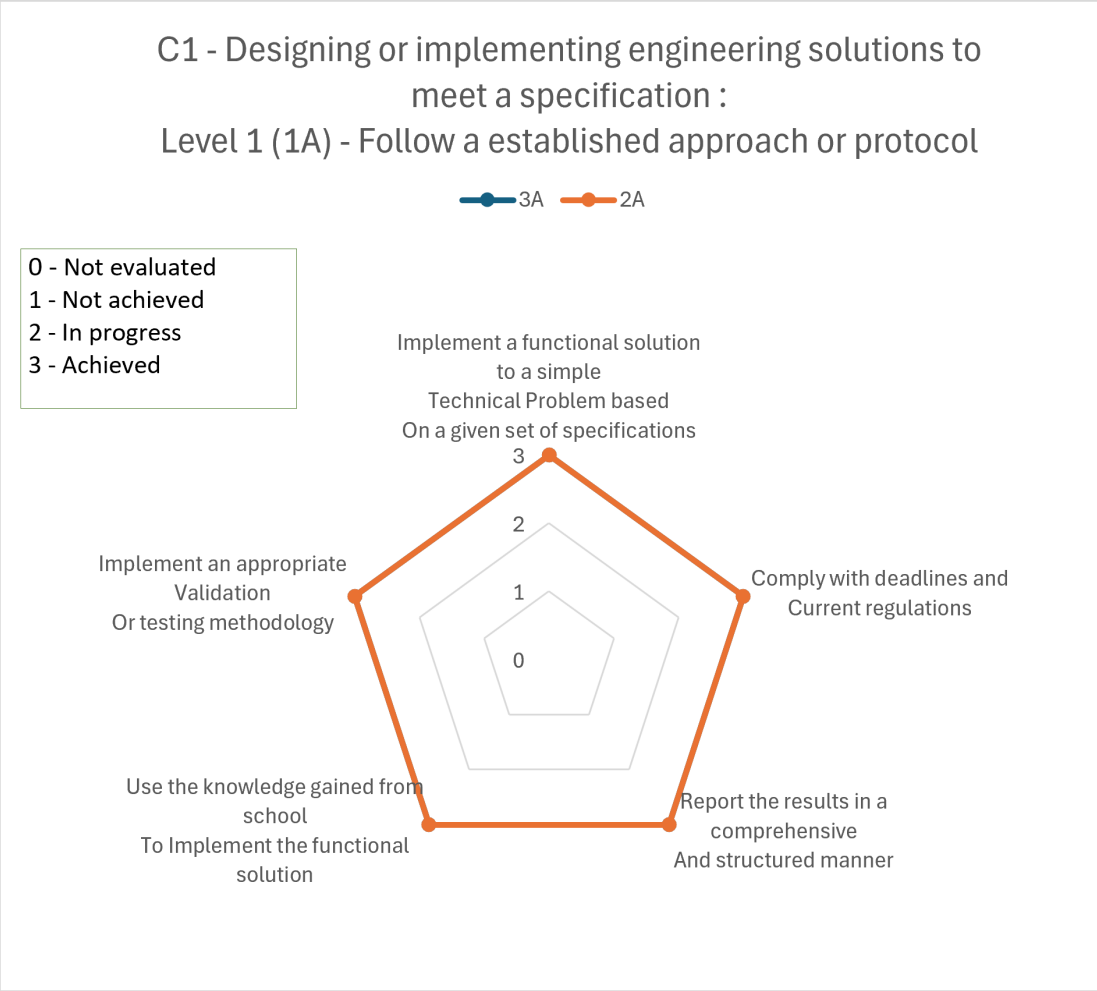
Internship supervisor: Stéphane, MANGIN, stephane.mangin@univ-lorraine.fr

School supervisor: Liliana, BUDA-PREJBEANU, liliana.prejbeanu@grenoble-inp.fr

Resources at disposition: Office space, characterization setup for AOS, Kerr microscopy, VSM, cleanroom, electrical setup...

C Skill Report:

C.1 C1: Designing or Implementing engineering solutions to meet a specification



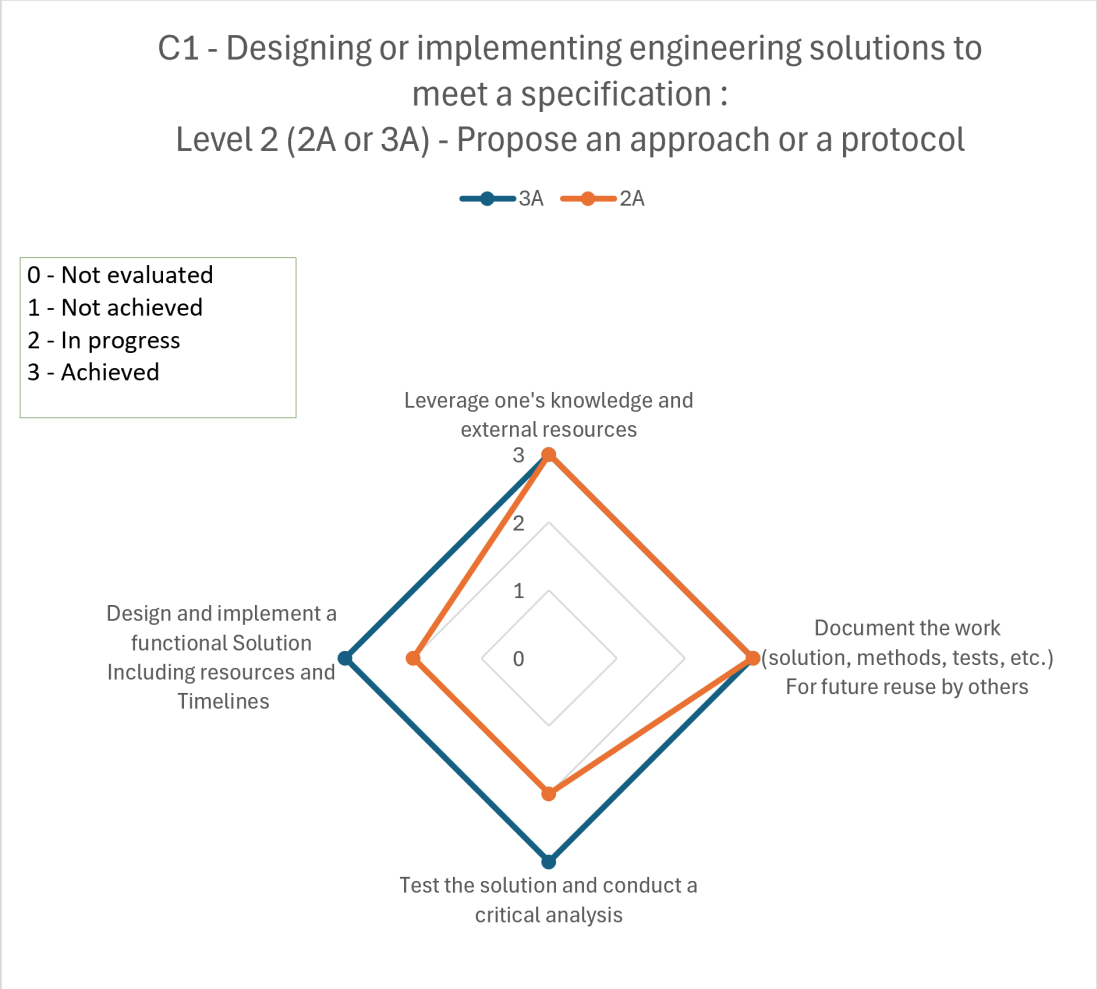
During my first year at PHELMA, I took part into a project to fabricate an arcade station. We were a group of 8 people, from different curriculums in electronics and material sciences. Together with our tutor, we had to define the specifications and deadlines of the project and organize the different tasks. To improve our efficiency, we divided the group into four smaller teams. I was part of the team responsible for the audio system, while also contributing to the administrative management of the project.

The four smaller teams were the following: Audio amplifier, Fabrication of the Arcade box, Communication and Finance group, and Programming the Raspberry Pi. While these were the main team distribution, each members participated in the different teams according to the need at the time being. I was mainly part of the Audio amplifier team, and the Communication and Finance team.

Along the speaker group, I used my knowledge acquired in electronic classes at PHELMA,

to develop a stereo speaker, and to link it to the Raspberry Pi card simulating the arcade station. It goes from design of an audio amplifier (fig. 45), to its assembly on a PCB. Moreover, along the Communication and Finance group, I took part in the organization of the project, such as defining the provisional Gantt Diagram to have a rough idea of the project's deadlines and goal, in the finance part, I was in charge of ordering some tools, such as buttons and joysticks for the arcade station.

This experience gave me the opportunity to apply my electronic courses, as well as developing my communication and time-management skills, through the Gantt Diagram and the report.



During my 2nd year internship, I studied the characterization and simulation of Bipolar Junction Transistor. With the help from my supervisor from CROMA and Arturia, I have defined a physical characterization protocol for Bipolar Junction Transistor, using a curve tracer Agilent B1500a. From these characterization, the transistor would be simulated through Virtual Analog for musical circuit.

I did not had any knowledge on BJT beforehand, at the start of my internship, I needed to leverage this gap through the literature. At the same time, I also propose a protocol to

characterize the parameter of the BJT according to the Ebers-Moll model, which is a compact model to describe the operating of a BJT.

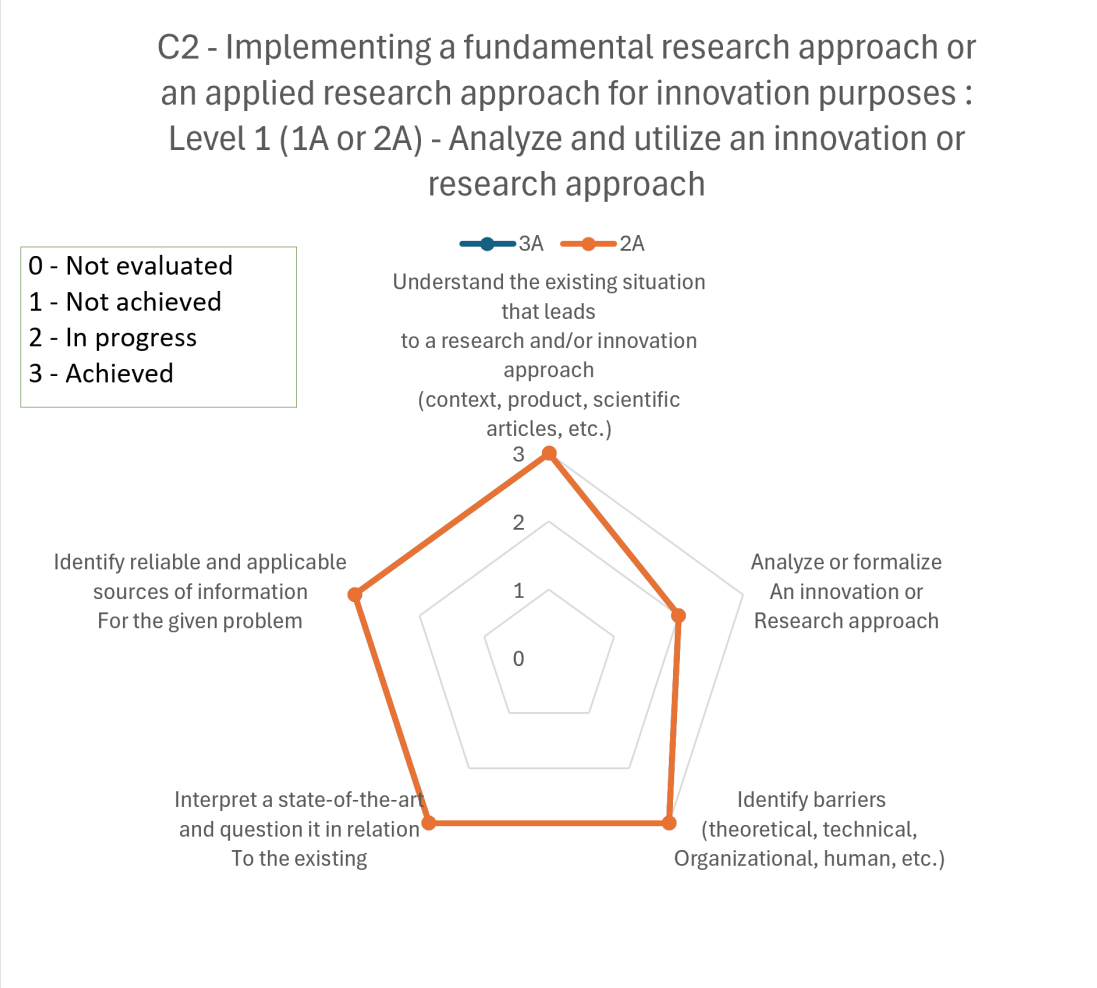
By using the protocol to characterize the BJT, we could after simulate it and compare the simulation with the analog circuit. Basically, we have an analog test circuit on a perforated electronic board, which is the control circuit. And on the other hand, we characterize the physical parameter of the BJT, and implement it in the numerical circuit, this is the test circuit. From the test and control circuit, we could observe the fitting between both, and how the BJT parameter affects the sound of the audio circuit. On Figure 46, we can observe the classical curve of a BJT, which measure the collector current as a function of the collector voltage.

This experience gave me the opportunity, to develop a protocol to characterize BJT, as well as leveraging my knowledge through literature and the help from my supervisors.

Moreover, during my master's thesis, I had the opportunity to leverage the two last points, I did not achieved during my 2nd year's internship. I designed and implemented, in labview and python programs, a semi-automated programs to generate the State Diagram of MTJ devices. After the semi-automated characterization of MTJ, a python script compute the figure of merit (thermal stability, coercivity field, etc...) and these results should be checked afterward in order to verify their physical meaning. During my first computation of thermal stability, I got values over 200 which is unlikely to happen, so I needed to test and modify the code, which was taking wrong inputs.

In conclusion, during my studies at PHELMA, I develop both competences to apply a specific protocol, as well as defining a protocol for characterization of BJT. I learn the importance to have a clear path, by defining clearly the goal of the project and the experimental protocol in order to have reproducible experiments.

C.2 C2: Implementing a fundamental research approach or an applied research approach for innovation purposes



During my 2nd year internship, I studied the characterization and simulation of Bipolar Junction Transistor, through 2 models: the Ebers-Moll model and the Gummel-Poon model.

This project was a novel approach tested by Arturia, to see if the characterization done experimentally by us, would have an important difference with the parameters used by LTSpice. Moreover, Arturia wanted to know if the difference could be heard.

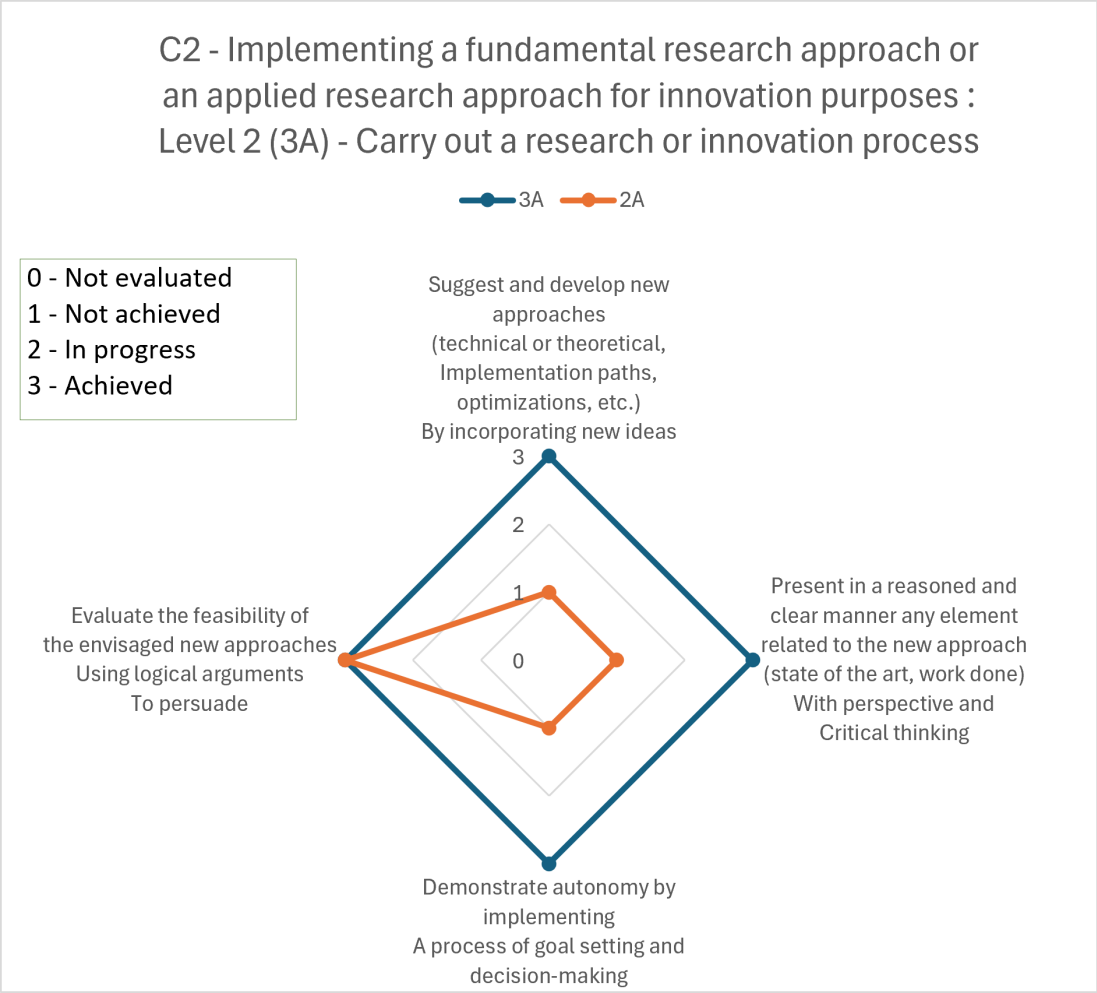
Before characterizing bipolar junction transistor, I needed to read the literature and resources on BJT to fill my knowledge on BJT. To fill these gaps, I read papers from the 1950s which describe the fundamental principles and characterization of the BJT. Afterward, I study the compact model (Ebers-Moll and Gummel-Poon) and how to characterize their parameters.

Concerning these two models, they should be implemented for real-time simulation. In this context, the computation time is highly important. The Gummel-Poon model is far more demanding than the Ebers-Moll model, so the Gummel-Poon model could not be used in every circuit due to the fact it will impact the computation time and the sound will be

distorted. The Gummel-Poon model should be used with caution to avoid over-calculation that will resorts in unwanted distorted sounds, these distorsions would not come from the circuit and transistor, but from the computer struggling to compute everything fast enough for real-time music plugin.

When using real-time simulation, a trade-off should be made between an accurate physical modelling and the computation time. This would allow to have an accurate model which will not distorts the sound from too many computation time. The computation time is one of the most important consideration, it should be small enough to not distort the sound, and to be used in parallel with other plugins.

During this internship, I learnt to leverage my knowledge through scientific literature, as well as to take into consideration the different sides of an engineering problem, going from characterization to define a compact model, to accounting for calculation time of audio circuit.



During my master's thesis, I had the opportunity to participate in a scientific project, in order to investigate the combination of AOS and STT. Starting from optimization of magnetic film, to obtain the wanted properties.

Both mechanisms, AOS and STT, were already well studied in the literature, although in AOS some switching mechanisms remain discussed. So in the first part of my work, I

collaborated with people from IJL and Tohoku to optimize thin film properties to obtain relevant magnetic properties. The first step, was to optimize the different building blocks of the spin valve individually. The optimization of the Synthetic AntiFerromagnet through Iridium coupling, the optimization of the seed layer to have a perpendicular magnetization for Co/Ni. From these optimization, we can integrated the blocks together to have a spin valve structure.

After this optimization of the thin film at IJL, these thin film have been patterned at Tohoku University. During my stay at Tohoku university, we modify the existing process flow for a 2 terminal MTJ, to define a process flow for a 4 terminal spin valve, as the resistance of a metallic spin valve is quite low, having 4 terminal allows a 4-probes like characterization.

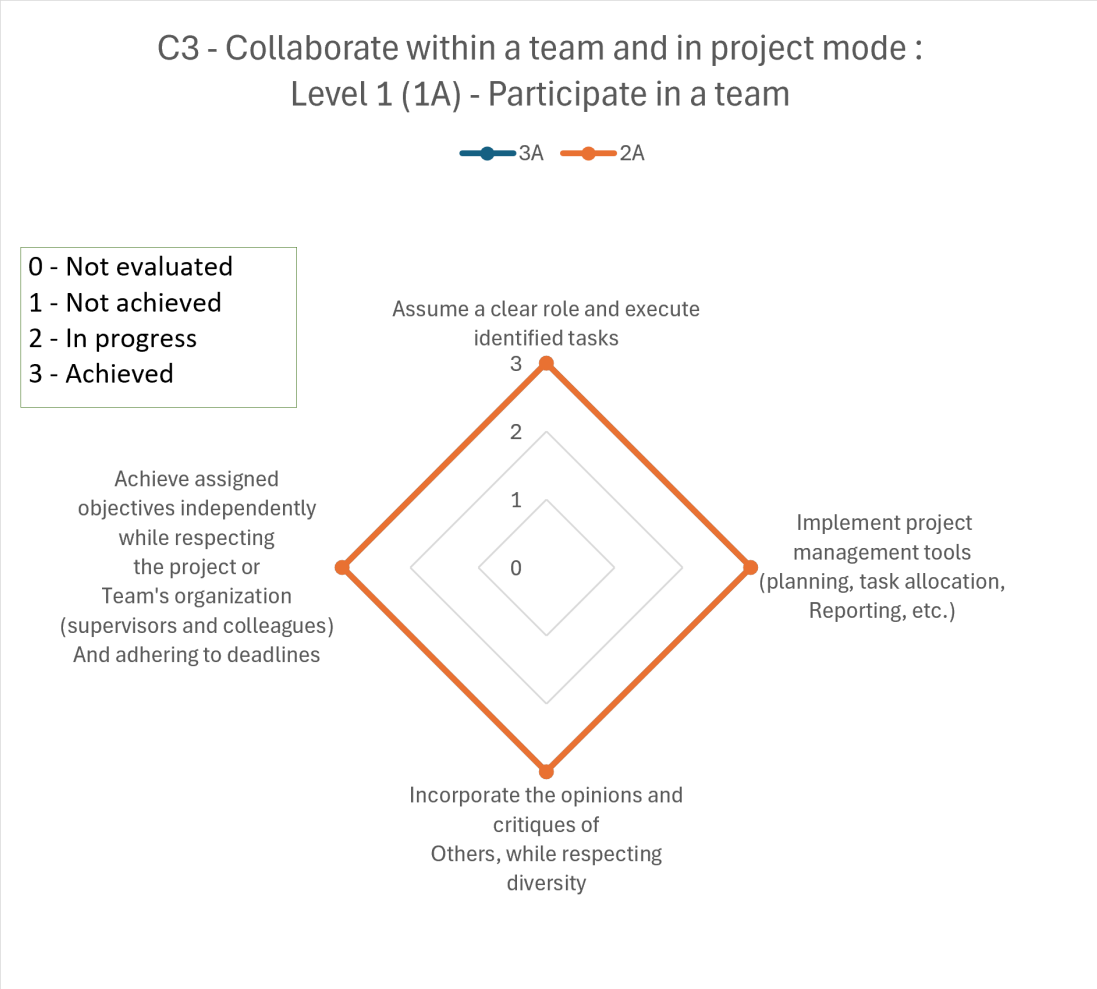
Moreover, in the case of electrical measurement for STT device, I worked on labview programs and python programs, in order to semi-automatize the measurement for thermal stability and state diagram (fig. 47).

Regarding the All-Optical Switching experiment, we needed to slightly adapt the experiment procedure to measure P to AP switching in spin valves, and through this modification we also changed the python workflow to characterize and plot ultrafast magnetization dynamics.

As we have only characterized AOS on thin film, and STT separately. We considered how to modify the layout and material of the top electrode, in order to have an optical access to the top free layer.

During both my 2 year's internship and my master thesis, I had the opportunity to work on innovative process. For Arturia, I developed a characterization protocol for BJT and their implementation on real-time simulation of audio circuit, which was a novel approach tested by Arturia. And during my master's thesis, I worked on top-of-the-art research on magnetic thin film, both on AOS and STT part, and I participated on their combination, at least the first proof of concept, to obtain energy efficient device. One way to improve my work would be to be less focused on "measurable", such as characterizing device, writing python code and so on, and to focus more thoroughly on the "global" picture of the work, why are we doing it, why does it work that way etc...

C.3 C3: Collaborate within a team and in project mode



During my first year at PHELMA, I took part into a project to fabricate an arcade station. We were a group of 8 people, from different bachelors.

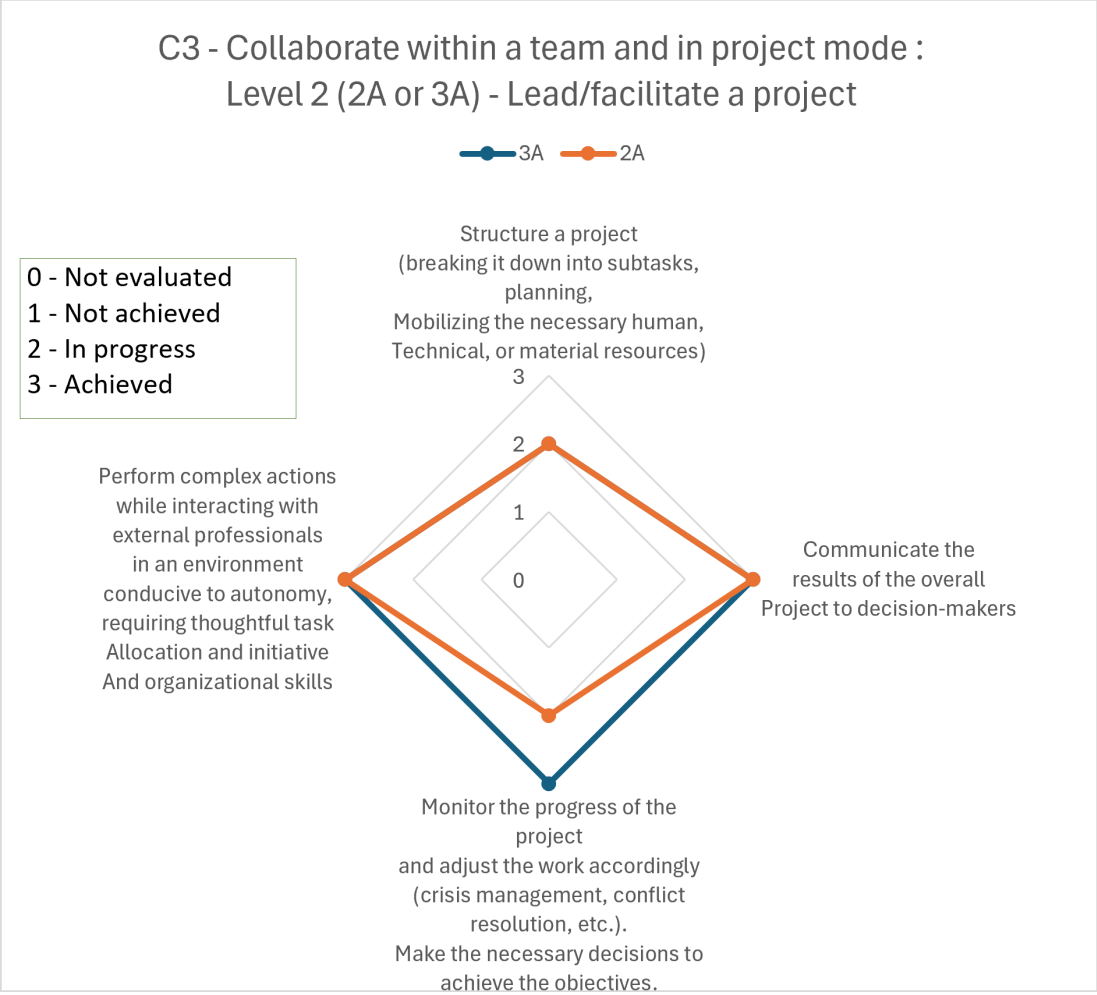
We needed to organize ourselve to define the specifications and deadlines of the project alongside our tutor. We had divided our group of 8, into 4 subgroups to be more efficient. I took part into the group doing a speaker and the communication and finance group.

At the beginning of the project, a predictive Gantt diagram and deliverables have been defined. We have estimated the time duration and risks of every deliverables, and their relation to each other, in order which deliverables was the most critical for the success of the project. That way, when facing unexpected situation, like waiting for a component for example, we know how it will affect the project, and come with a solution. Along the speaker group, I used my knowledge acquired in electronic classes at PHELMA, to develop a stereo speaker, and to link it to the Raspberry Pi card simulating the arcade station.

While implementing the audio amplifier in the arcade box, we found that due to the small space between the wall of the box, the screen monitor and the Raspberry Pi, we had no place left to implement the audio amplifier and the speakers. That was an unexpected problem,

however we find a solution by putting the speaker on top of the arcade box, it impacts the sound, but it was a better solution than having no sound.

Moreover, we had have meeting every weeks to describe the progress of the arcade station. During theses meeting, we discuss about what we were struggling with, and the next steps of the project.



During my 2nd year at PHELMA, I took part in the project to simulate FDSOI at cryogenic temperature through the use of the TCAD Sentaurus. For everyone of us, it was the first time working on a TCAD software.

We were a group of 8 people, and we divided into 3 subgroup according to the necessity of the project. However, the group were not fixed, a person could switch from one to another according to the need, if a team encountered a problem for example. There were 3 main subgroups, one for the simulation of dynamic thermal heating in the channel of the FDSOI, another one to compare the different transport model, and a last one for defining thermal contact and its implication on the device (fig. 48).

Knowing that Sentaurus is a difficult software to use, we share our experience between each team to acquire a better understanding of the software's possibilities. Moreover, we had regular meeting with our supervisor to explain our progress and the next steps of our

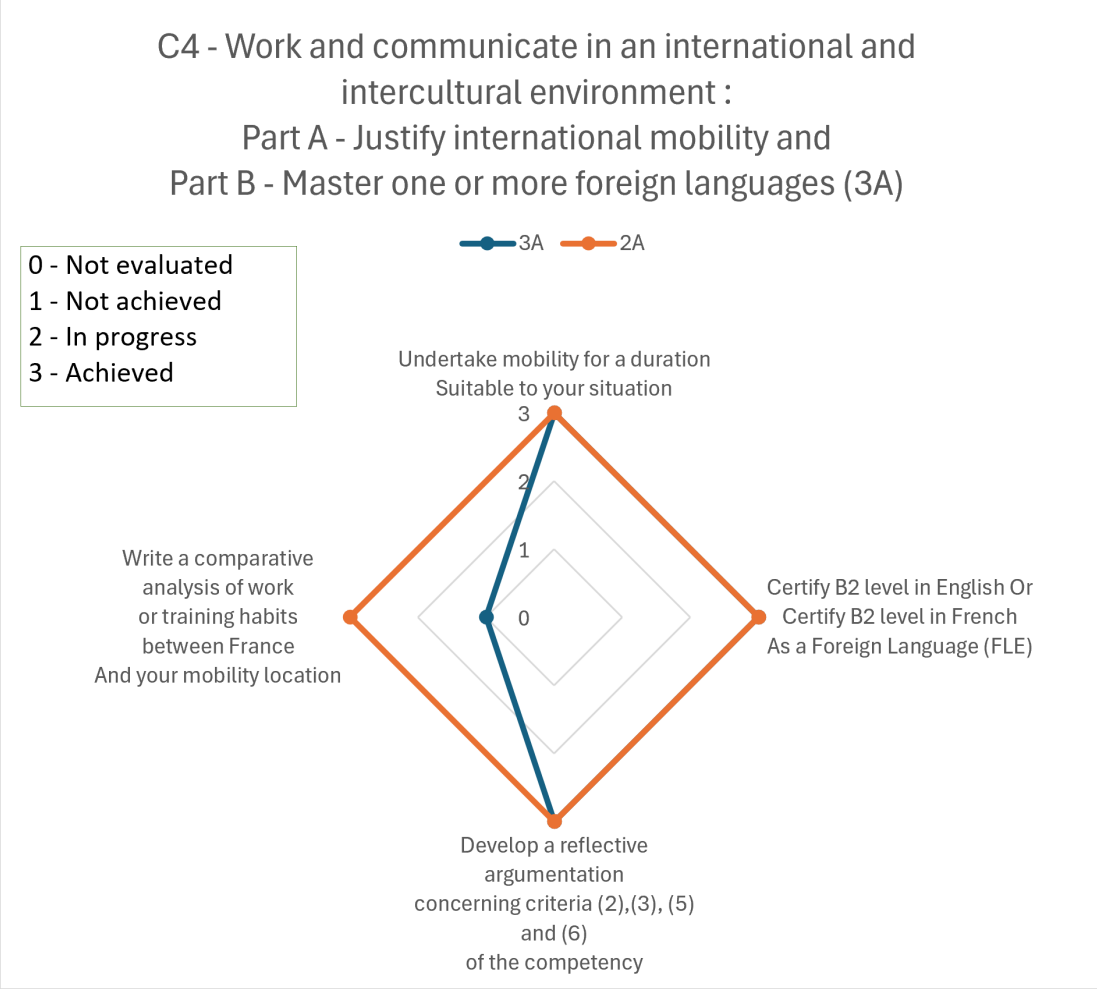
project. These meeting were really useful to have the insights of our supervisor who have more knowledge on Sentaurus. It allows us to go further into the topic as it guides us toward a goal. Furthermore, another great help during this project, was the user manual from Sentaurus, it was really tough to understand it. However, it was of great help as it has lot of explanations, such as the validity domain for the transport model.

In addition, we were a strongly international team composed of 5 Italians and French, so we need to adapt our work methodology, to work in harmony. French people were more simulation-oriented, we advance per testing some patterns on Sentaurus, and looking at the user manual to try various things. While Italian people were more theoretically-oriented, before implementing a simulation they want to understand all the physics behind. Thus,the coordination was quite good, because both approaches are complementary, as simulation is already a complex field, so some could focus on understanding how the software work, while others were focusing on explain the physics behind.

We had have regular meeting among ourselves, either the whole team or in each subgroup. In order to monitor the progress of the work, and the struggles we encountered. That way, we could define the next step of the project, which was most of the case to try to go to lower temperature. And when someone struggle with the software, everyone could help accordingly.

Along my stay in PHELMA, I participated in a lot of group project. In my opinion, it is the most useful kind of process to learn, as the students need to collaborate, from organizing themselves, to sharing their knowledge and know-how, it is some of the most formative experience. I think, one way to improve my work, is to divide and structure the work more thoroughly, with clear deadlines and deliverables for every project.

C.4 C4: Work and communicate in an international and intercultural environment



During my studies in PHELMA, I had many opportunities to work in an international and intercultural environment. In less than 2 years, I have work in 4 different countries. I am a MNIS master' student, so I have worked for 6 months in Politecnico di Torino (Italy), 6 months in Grenoble INP PHELMA (France), 6 months in EPFL (Switzerland), and for my master thesis, I worked 3 months in IJL Nancy, and 3 months in Tohoku University.

This highly international environment was, in my opinion, really beneficial and allow to exchange idea among people from various horizons. That trains our adaptability and open-mindness, as well as being a good english training as we are constantly speaking english from casual conversation to technical ones.

From an academic point of view, what was the most striking difference between France, and others countries such as Italy and Switzerland. Is the size of the university, and the number of student and different nationalities. When we are in PHELMA, there are only roughly 2000 students, and we are all separated in subgroups (IPhy, BIOMED, NANOTECH etc...), so basically there are not much exchange between these groups from a scientific point

of view, as people from the same sector stay mostly together, even though obviously there are still link between each sector. While in EPFL and PoliTo, I find that there is far more exchange between people from different fields, such as between electronic, mechanical masters for example. I think it derivate from the fact that, while the French engineering school have a more or less strict curriculum, so less mixing between group, while in EPFL and Italy, the student are more free to choose their major and class. Hence, leading to more stirring between field, and so maybe a more global vision of science. Moreover, another thing that I appreciate in EPFL and PoliTo, is that the classes were for the whole semester, with a more or less "theoretical" at the beginning, to go application and project in the middle or end of the semester.

Regarding the criteria (2), (3), (5), (6):

- 2: Showing open-mindedness and tolerance
- 3: Demonstrating adaptability
- 5: Considering ambiguity in intercultural relations
- 6: Respecting cultural diversity

In my opinion, these are fundamental rules for living in society. Everywhere, we need to be adaptable and flexible, be it in work environment or international environment. Been flexible and adaptable, is a fundamental skill to have, because there are always unexpected events at work or in life. Even though adaptability is even more important in a foreign country, such as Japan, you need to adapt to the cultural way of life, as everything is unknown, misunderstanding between people might be common, so one need to understand slightly the cultural in order to avoid misunderstanding. Regarding open-mindedness and tolerance, both are important as it allows to meet more people with different points of view, that might gave a new vision on the world. Every culture has a different relation with concepts, such as nature, work, religion, and society, by been open-mindedness it might allow us to develop critical thinking, both from a scientific and societal point of view.

Along my years in PHELMA, I had many opportunities to work and collaborate in intercultural and international environment. From my point of view, it is really beneficial for the quality of the work, as everyone has different background, so they could view certain aspect of the work that might have been overlook otherwise.

C.5 C5: Integrate technological, environmental and societal transitions into the work

During my master degree, I had have the opportunity to participate in a few conferences that spoke about the effects of electronic on the environment, to give a few names, I followed conferences and classes on:

- Digital Odyssey workshop on sustainable ICT
- The rebound effect
- Sustainable design based on advanced VLSI nanoelectronics

All these activities gave me new insights about the impact of electronic on the planet, they gave me a new point of view about electronic. For the past decades, electronic devices has reshaped our lifestyle, become more and more prominent in society and our environment. The objective of electronic is not only to improve it capacity (performance, speed, latency...), but also to take into account it impact on the environment and also on mankind.

The workshop on sustainable ICT was organized by GreenChips-edu which is a collaboration between 7 universities (Grenoble-INP, TU Graz...), 7 companies (Infineon, Silicongate...) and 1 research center. It gave me insights about the impact of electronic on the environment, such as order of magnitude for electronic devices, e-waste and electric consumption. I learnt that all the electronic devices in the world, are estimated to use roughly 3-5% of the total electric production (equivalent of France production), and it consumption is expected to increase even more in the next years. Thereby, energy efficiency becomes an important topic in electronic design.

Moreover, from the conference on the rebound effect, I learnt that the solution may not be a technological solution. Even through improving the energy consumption of devices may seems like a solution, in reality reducing the energy consumption will lead to an increase in CO2 emissions and e-waste. It is due to the fact that, the less is the energy consumption, the more we could produce and use the device. More efficient devices will be produced and used in higher quantities, thereby the economy in the technological side will induce an increase in usage. The losses from the improvement in technology, may overthrow the benefits.

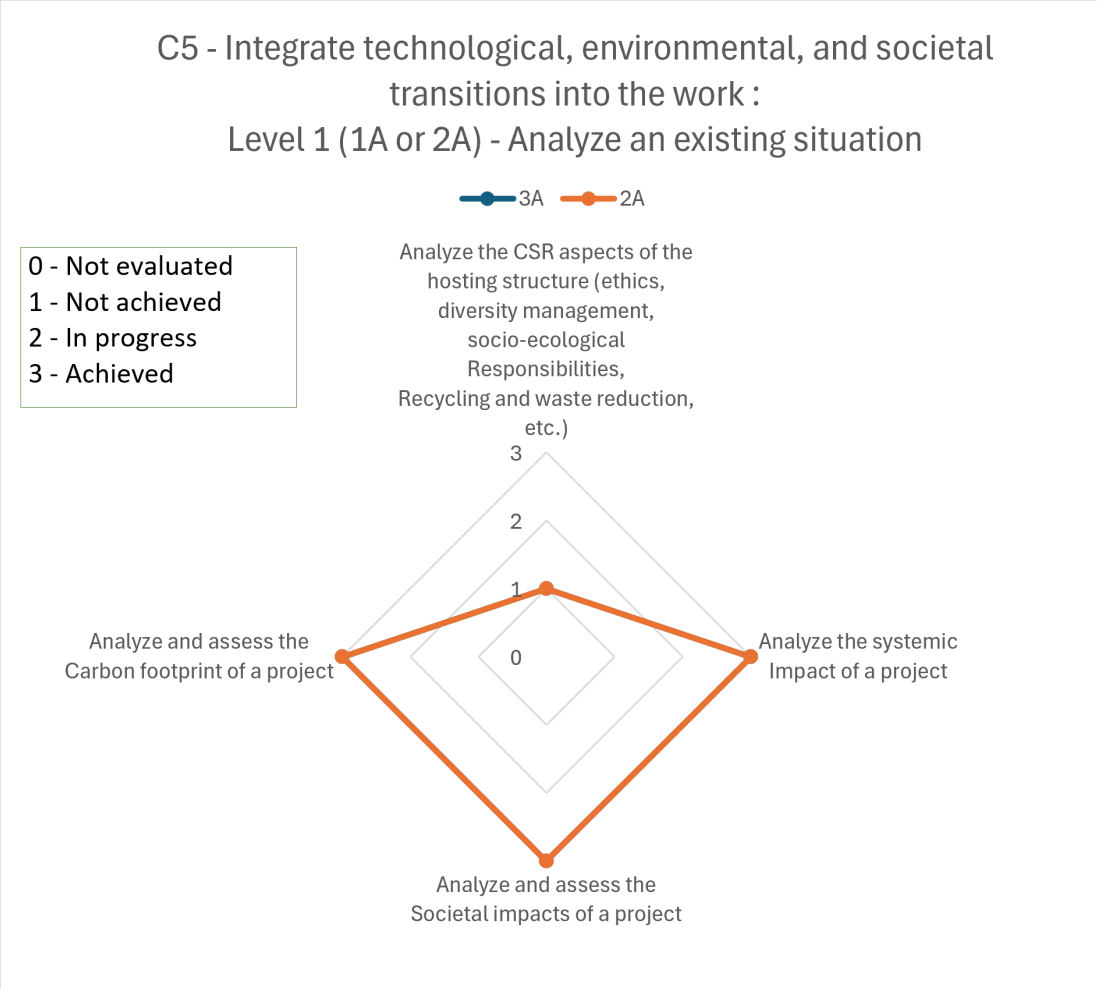
Of course, technological advancements still play an important role to have a more sustainable electronics. There should be continued efforts to develop energy-efficient systems through better design, optimization, development of new materials, and innovative fabrication processes. For example in Very Large Scale Integration (VLSI), there exist a few techniques and methods to design a chip which has improved energy performance. Other than the design part, the development of new processes and structures (FinFET, Gate-all-around...), may also lead to the reduction of power consumption.

In this context, technologies can show some paths toward a more sustainable electronics. However as seen with the rebound effects, the solution to the environmental impact of electronic, is not solely a technical solution, it should also be a societal solution. Using only the technological aspect may lead to the worsening of the situation, due to overproduction and overconsumption. There should be the simultaneous evolution of technologies, societal norms and regulations to go toward a more sustainable electronic.

Technology could be optimize to have the lowest environmental impact, but the consumer

using it has as much impact. To have a sustainable electronic and technological transition, the solution is plural, it should go through consumer awareness, regulations (e.g.: right to repair). To limit the impact of electronic on the environment, all the chain of value of the product should be supervised.

In conclusion, addressing the environmental challenges posed by electronics requires an integral approach, starting from technology and production, passing through customers awareness and regulations, and ending by a better management of e-waste. To achieve the integration of technological, environmental and societal transitions into the work, is a complex and interrelated process which go through many different areas and societal layers.



During my master thesis, my subject was about the combination of AOS and STT. The objective of this work was to combine both mechanism in order to obtain ultrafast and ultra energy efficient magnetic memories.

This objective arise, knowing that due to nearly exponential increase in data storage, the energy required for data storage will be 12% of all of US electricity production in 2028. Thus arise the need for more energy efficient devices, that may reduce this energy demand. Due to their energy efficiency this kind of device, might be more sustainable for memory application at a time where memory take an even more important role with the rise of AI, which require

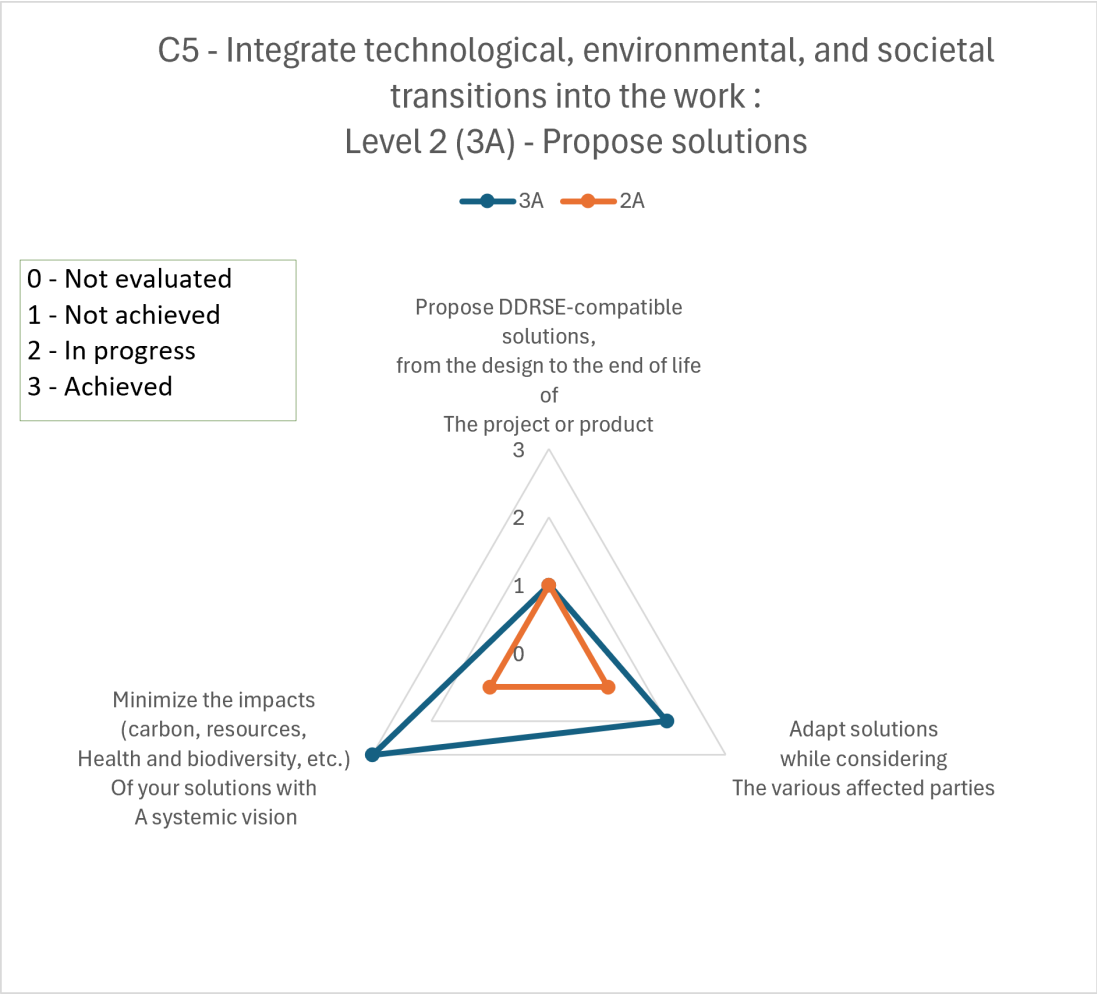
a large amount of data to be processed. So reducing the energy required for memory, would in the same time, reduced energy consumption for AI and allow to obtain a more sustainable AI. To have some order of magnitude, AOS is expected to be nearly 100 times faster than other magnetic device, and only consume a few fJ/bit so nearly 1000 times more efficient. Plus, with the development of STT-MRAM that allows in-memory computing, the energy required would be even lower.

However, while this seems like a a great solution to reduced AI energy consumption, it might not be completely exact. Due to the rebound effect, one reduction in cost or in energy efficiency, might lead to an increase in energy consumption or pollution. Because, if a device become more efficient and cheaper to produce, in the same time it could be integrated and used in more systems, leading therefore to an increase in energy consumption. While this rebound effect should be kept in mind, when speaking about energy efficient device, the combination of AOS and STT is still a promising ways to develop energy efficient device. When this technology would be more matured, there should be a thorough investigation about its energy efficiency, and environmental impact.

Another thing that should be kept in mind, when speaking about electronics, is that some of its resources are rare earths. And some AOS composition are also composed of rare earths, which arise concerns about worker condition and environmental impact of fabrication.

All these remarks should be kept in mind, to avoid over optimism about energy efficient devices. This field of work should obviously be studied thoroughly, however there might still be drawback coming from its usage.

In my opinion, as a future engineer I think that taking into account as much as possible environmental and societal aspect in technologies is of the highest importance for sustainability. However, while I learn a lot about sustainability from a "theoretical" point of view, I don't think I learn enough about how to implement it in concrete technological application.



C.6 Traces of Project:

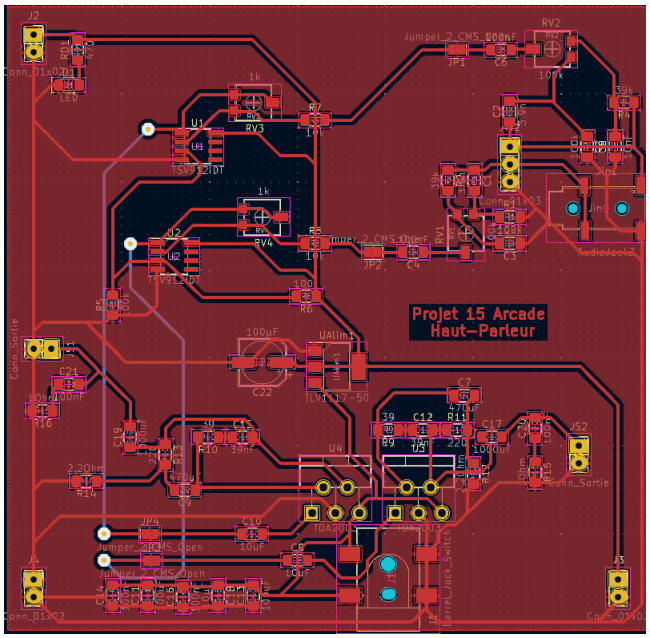


Figure 45: PCB circuit of the Audio Amplifier

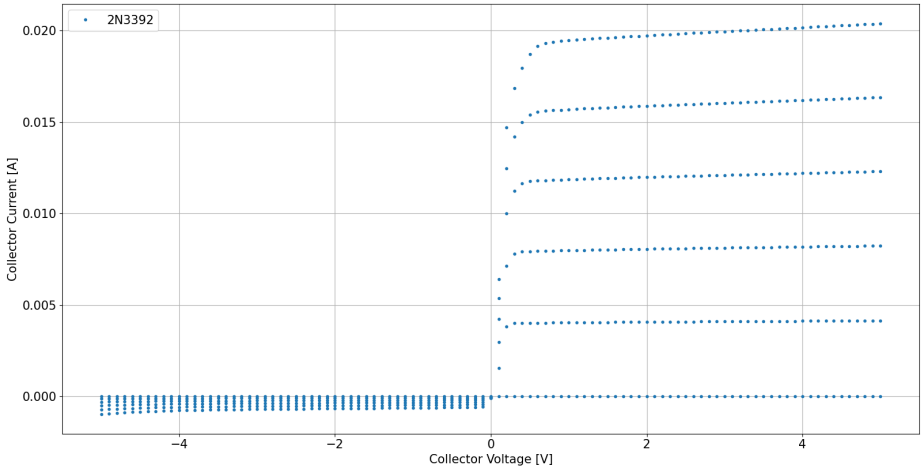


Figure 46: Evolution of collector current as a function of collector voltage

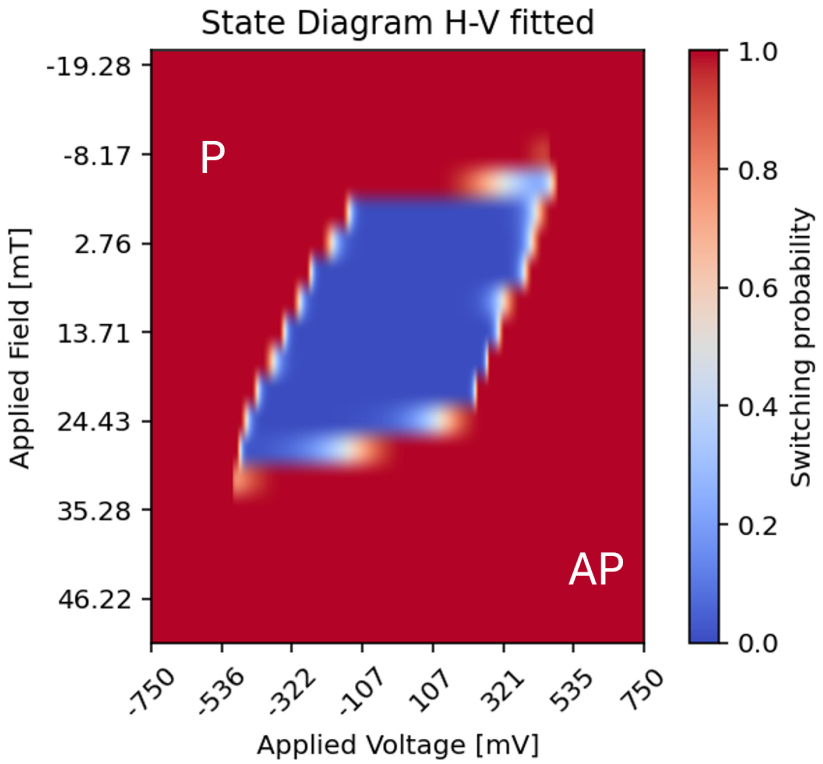


Figure 47: State diagram defined through automation using labview and python programms

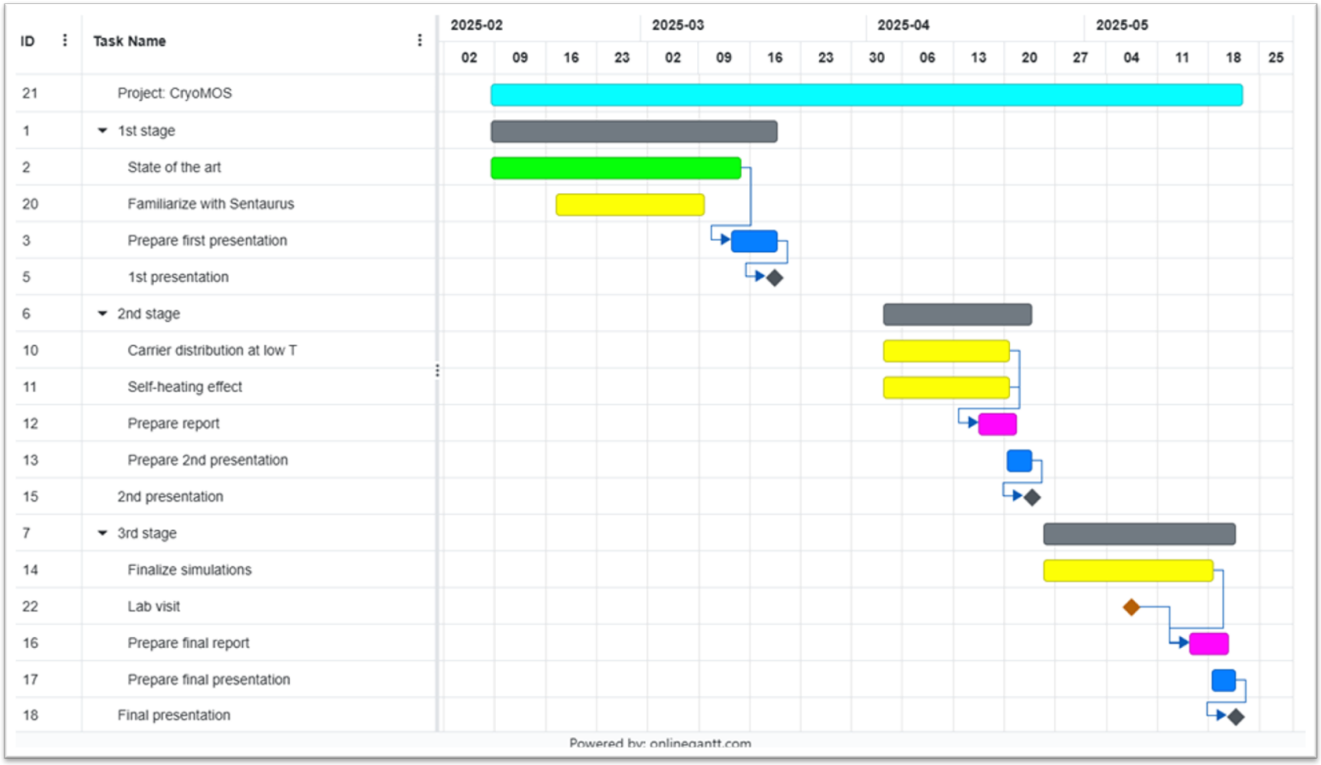


Figure 48: Gantt Diagram presenting our role repartition and deadlines